

THESIS FOR THE DEGREE OF DOCTOR OF PHILOSOPHY

Nanoplasmonics for solar cells

Viktorija Gusak



Department of Applied Physics
CHALMERS UNIVERSITY OF TECHNOLOGY
Göteborg, Sweden 2014

Nanoplasmonics for solar cells
Viktoria Gusak
ISBN 978-91-7385-962-2

© Viktoria Gusak, 2014.

Doktorsavhandlingar vid Chalmers Tekniska Högskola
Ny serie nr 3643
ISSN 0346-718X

Department of Applied Physics
Chalmers University of Technology
SE-412 96 Göteborg
Sweden
Telephone + 46 (0)31-772 1000

Cover picture:

Schematics of samples used in this thesis: (top left) plasmon-induced photoconductivity measurements on ultrathin amorphous silicon films; (bottom left) cones/amorphous silicon film on top of a reflector-spacer structure; (top right) Indirect nanoplasmonic sensing of dye adsorption on a flat TiO₂ film; (bottom right) dye diffusion front in a porous TiO₂ film.

Printed at Chalmers Reproservice
Göteborg, Sweden 2014

Abstract

The main source of our energy system, the fossil fuels, will eventually be depleted and also pose environmental and climate hazards. There is thus a need for alternative, renewable energy sources. Solar (photovoltaic) cells will play an important role as one of them. The photovoltaics research is extensive today, but the relatively high cost of solar cells and/or insufficient efficiency make them still often loose in the energy market competition.

This thesis explores novel concepts for solar cell research, enabled by advances in nanotechnology, specifically applying the phenomenon called plasmon resonance in metal nanoparticles, to study and improve thin-film solar cells. The plasmon resonance is a collective oscillation of conduction electrons in a metal nanostructure, which can be excited by light. It leads to interesting and potentially useful interactions between nanoparticles and light; in particular, the electric field in the vicinity of the nanoparticle is enhanced compared to that of the incident light. This work focuses on employing the enhanced field to (i) improve light absorption in thin amorphous silicon (a-Si:H) films and (ii) to sense adsorption and diffusion of dye molecules in TiO₂ films, used for dye-sensitized solar cells.

In the first part of the thesis, optical and photoconductivity measurements were performed on ultrathin a-Si:H films, with and without Ag plasmonic nanoparticles, in order to quantify the light absorption in a-Si:H films caused by the enhanced near-field around the nanoparticles. The effect was studied for (i) systems of Ag nanodiscs coated with a-Si:H films of various thicknesses, and (ii) Ag cone/a-Si:H nanocomposites placed on a reflector-spacer structure with varied geometric parameters. Finite-element method calculations were used to connect observed experimental features to specific plasmon resonance modes, and to explain mechanisms of absorption enhancement in the a-Si:H films.

The second part of the thesis is focused on adsorption and diffusion kinetics of dye molecules on TiO₂ films, studied by Indirect NanoPlasmonic Sensing (INPS) and Quartz crystal microbalance with dissipation monitoring (QCM-D) techniques. Measurements on flat film model systems revealed details of adsorption and desorption kinetics and allowed extracting the corresponding rate constants. Incorporating plasmonic sensing nanoparticles within mesoporous TiO₂ films provides a unique opportunity to resolve adsorption kinetics locally in the film (in this case, at the bottom of the mesoporous TiO₂ films). Diffusion times for dye molecules through the mesoporous films were measured and modelled with a diffusion-front model. This allowed deriving the effective diffusion coefficient of the dye molecules in this system.

Keywords: plasmonic nanoparticle, Localized Surface Plasmon Resonance, amorphous hydrogenated Silicon, enhanced near-field, Dye-Sensitized Solar Cell, mesoporous material, titanium dioxide, diffusion, adsorption, Langmuir kinetics, diffusion-front model.

Appended publications

Paper 1

V. Gusak, B. Kasemo, and C. Hägglund.

Thickness dependence of plasmonic charge carrier generation in ultrathin a-Si:H layers for solar cells.

ACS Nano 5 (8), 6218-6225 (2011).

Paper 2

V. Gusak, B. Kasemo, and C. Hägglund.

High aspect ratio plasmonic nanocones for enhanced light absorption in ultrathin amorphous silicon films.

In manuscript.

Paper 3

V. Gusak, L.-P. Heiniger, M. Grätzel, C. Langhammer, and B. Kasemo.

Time-resolved Indirect Nanoplasmonic Sensing Spectroscopy of dye molecule interactions with dense and mesoporous TiO₂ films.

Nano Letters 12, 2397-2403 (2012).

Paper 4

H. A. Harms, N. Tetreault, V. Gusak, B. Kasemo, and M. Grätzel.

In situ investigation of dye adsorption on TiO₂ films using a quartz crystal microbalance with a dissipation technique.

Physical Chemistry Chemical Physics 14, 9037-9040 (2012).

Paper 5

V. Gusak, L.-P. Heiniger, V. P. Zhdanov, M. Graetzel, B. Kasemo, and C. Langhammer.

Diffusion and adsorption of dye molecules in mesoporous TiO₂ photoelectrodes studied by Indirect Nanoplasmonic Sensing.

Energy and Environmental Science 6, 3627-3636 (2013).

Paper 6

V. Gusak, E. Nkurunziza, C. Langhammer, and B. Kasemo.

Real time adsorption and desorption kinetics of dye Z907 on a flat mimic of dye-sensitized solar cell TiO₂ photoelectrodes.

In manuscript.

Publications that are not a part of this thesis

M. Schwind, V. D. Miljkovic, M. Zäch, V. Gusak, M. Käll, I. Zoric, and P. Johansson.
Diffraction from arrays of plasmonic nanoparticles with short-range lateral order.
ACS Nano 6, 9455-9465 (2012).

M. Müller, U. Jung, V. Gusak, S. Ulrich, M. Holz, R. Herges, C. Langhammer, and O. Magnussen.

Localized surface plasmon resonance investigations of photoswitching in azobenzene-functionalized self-assembled monolayers on Au.

Langmuir 29, 10693-10699 (2013).

Contents

Abstract.....	iii
Appended publications	iv
Publications that are not a part of this thesis	v
1. Introduction.....	1
2. Physics of solar cells.....	7
2.1. Solar cells basics.....	7
2.2. The solar spectrum	9
2.3. Working principles of solar cells	10
2.3.1. Physics of semiconductors	10
2.3.2. Absorption of light: photogeneration of charge carriers and recombination.....	14
2.3.3. Separation of charge carriers: junctions.....	16
2.3.4. Efficiency limitations for solar cells	19
3. Solar cell research: achievements and challenges.....	23
3.1. Crystalline solar cells	23
3.1.1. Single- and polycrystalline Si solar cell.....	23
3.1.2. III-V crystalline solar cells	25
3.2. Thin-film solar cells.....	26
3.2.1. CdTe and CIGS solar cells	26
3.2.2. Amorphous silicon solar cells	27
3.2.3. Micro- and polycrystalline silicon solar cells	29
3.3. Organic solar cells	30
3.4. Dye sensitized solar cells and related concepts	31
4. Localized Surface Plasmon Resonance	35
4.1. Classical models of optical constants	35
4.1.1. Two types of optical constants.....	35
4.1.2. The Lorentz model	36
4.1.3. The Drude model.....	38
4.2. Localized Surface Plasmons	41
4.2.1. Qualitative description.....	41
4.2.2. Metal particle in a quasi-static electric field	41
4.2.3. Beyond the electrostatic approximation	46
4.3. Applications of nanoparticle plasmon resonance	48
4.3.1. Brief overview	48
4.3.2. Sensing using nanoparticle plasmons	49
4.3.3. Indirect nanoplasmonic sensing technique	50
5. Interactions of dye molecules with compact and porous TiO₂ films: adsorption, desorption and diffusion	53
5.1. Basics of adsorption of molecules on solid surfaces.....	53

5.2. Kinetics of adsorption and desorption	54
5.3. Adsorption isotherms	57
5.3.1. Basic overview	57
5.3.2. Langmuir adsorption model.....	58
5.3.3. Other adsorption models	59
5.4. Studies of adsorption and desorption of dye molecules on TiO ₂ surfaces	61
5.5. Dye loading of mesoporous TiO ₂ photoelectrodes for Dye solar cells.....	64
5.6. Diffusion of dye molecules in mesoporous TiO ₂ films.....	65
6. Nanoparticle plasmonics for enhancing light absorption in solar cells	69
6.1. Mechanisms of plasmonic absorption enhancement	69
6.2. Results for various solar cell types	72
6.2.1. Plasmonic nanoparticles for monocrystalline solar cells	72
6.2.2. Plasmonics for organic and dye-sensitized solar cells: a few examples	74
6.2.3. Plasmonics for improving a-Si:H solar cells	75
7. Experimental methodology.....	81
7.1. Fabrication techniques	81
7.1.1. Photolithography.....	81
7.1.2. Thin-film deposition by evaporation and sputtering	83
7.1.3. Hole-mask colloidal lithography	85
7.1.4. Plasma enhanced chemical vapour deposition for producing a-Si:H films	87
7.2. Characterization techniques	87
7.2.1. Photoconductivity measurements	87
7.2.2. Light transmission and absorption measurements.....	88
7.2.3. Indirect nanoplasmonic sensing measurements.....	89
7.2.4. Spectroscopic ellipsometry.....	91
7.2.5. Scanning Electron Microscopy	92
7.2.6. Quartz crystal microbalance with dissipation monitoring (QCM-D).....	93
8. Summary of results	95
9. Outlook	101
9.1. Near-field plasmonic enhancement for a-Si:H solar cells.....	101
9.2. Adsorption, desorption and diffusion of dye molecules on and in TiO ₂ films	102
9.3. Possible combinations of the two lines of research.....	104
10. Acknowledgements	105
11. References.....	107

1. Introduction

The modern life of humankind, especially in developed countries, critically depends on energy supply primarily in the form of fossil fuels (coal, oil and natural gas), hydroelectric and nuclear energy, and biomass. Fossil fuels are totally dominating, contributing about 80 % of the total world energy consumption [1]. The amounts of energy needed increase at fast rates, mostly due to the economical growth of developing countries and also because of the increase in the population of Earth. This increasing demand leads to numerous problems, the two most important being the unavoidable depletion of the fossil fuel resource sooner or later, and the adverse effects of increased amounts of carbon dioxide (CO₂) gas in the atmosphere that result from using the fuels in energy demanding processes, such as industry, transport systems and house heating.

The known remaining *fossil fuel resources*, which can be extracted with existing technologies at current prices, are about 10¹² tons of coal equivalents [2]. The world consumption in 2002 was about 1.3×10¹⁰ tons of coal equivalents [2], and with this number the fossil fuels would be enough for 70 more years if the consumption rate remained constant (which will not be the case). However, estimations suggest that there should be more fuels available in the Earth crust [2], especially as coal. Moreover, a relatively recent (around year 2000) development of fracking, a method to harvest shale gas and oil [3], provided access to large fossil fuel resources, which were not available before. Depletion of all fossil resources is therefore not likely to occur within the next 100 years. For conventional raw oil and natural gas the times scales are however significantly shorter. Prices will increase, which will have a damping effect on the consumption rate and a stimulating effect on energy savings and energy efficiency. Increased fossil fuel prices will also create opportunities for new sustainable energy supply systems such as wind and solar energy.

Another urgent problem, closely interlinked with the energy needs, is the much-discussed *greenhouse effect*, which is expected to lead to global warming and climate change. The latter in turn may cause serious harmful effects in the whole world: various climate instabilities (including hurricanes, fires, floods and increasing sea levels), diseases and extinction of some plant and animal species, and even possibly disappearance of whole islands and countries. The greenhouse effect originates primarily from increased amounts of CO₂ in the atmosphere, produced as a side product of burning fossil fuels. CO₂ molecules absorb infrared light, the atmosphere thus heats up and radiates some of the energy back to Earth (instead of transmitting it into cosmos), increasing the Earth's temperature. The exact mechanisms and consequences of the greenhouse effect are a subject of intense debate, but most

researches agree that the amount of CO₂ exhausted into the atmosphere should be minimized as soon as possible. It should be mentioned that the greenhouse effect is also promoted by other gases like methane and N₂O.

The world used about 148 000 terawatt-hour (TWh) of energy in 2010 and is expected to consume about 170 000 TWh in 2050 [1]. In 2010, 81% of the world total energy consumption was based on fossil fuels. For comparison, the total energy supply in Sweden in 2010 was 550 TWh, out of which only 31% originated from fossil fuels [1], mainly for the road transport system. In order to stabilize the CO₂ concentration in the atmosphere at 450 ppm (which is slightly higher than the current 393 ppm [4]), the energy provided by fossil fuels has to be limited to about 90 000 TWh in 2050 [5] and/or very efficient means of collecting and storing CO₂ must be developed (CCS=carbon capture and storage). The rest of the energy supply, i.e., 80 000 TWh, must come from renewable energy sources. The latter primarily include biomass (electricity and fuel from residues from wood industry, organic waste etc.) with an estimated capacity of 35 000 TWh, nuclear energy contributing 21 000 TWh, and hydropower with 9 000 TWh of energy supply in 2050 [5]. Wind power is expected to contribute 5 000 TWh in 2050, and solar energy sources will then likely supply about 9 000 TWh [5].

Sunlight is the most powerful sustainable energy source available on Earth. It is estimated that an area in Sahara of approximately the size of Belgium (about 30 000 km²) covered with solar modules of 25% efficiency would produce all needed global electricity supply in 2008 (about 20 000 TWh) [5]. Another popular estimation is that placing solar cell panels of 10% efficiency on 6 areas, 100x100 km each, of high solar radiation around the globe would provide energy enough to cover the electricity need of the world (ca. 70 000 TWh) [6]. Solar energy can be used in two basic approaches being developed today: the solar thermal technology, and photovoltaics. In a *solar thermal* concentrator, numerous mirrors focus sunlight onto a medium (air, water etc), which provides heat to drive a thermal cycle, just as in fossil power plants. Essentially, concentrated solar light heats water to produce hot steam, which runs a steam turbine connected to an electrical generator. In the second approach, a *photovoltaic (PV) cell* (solar cell) produces electricity directly from sunlight via physical processes in specially designed materials. Photovoltaics is in focus in the present thesis.

The *installed capacity* of solar cells over the world as of 2012 is approximately 100 GW, and they can annually produce the same electrical energy as 16 coal power plants [7]. Most of these solar cells are installed in Europe (ca. 70 GW), where the generated energy covers 2.6% of the total electricity demand. Next in the ranking are China (8.3 GW), the USA (7.8 GW), and Japan (6.9 GW) [7]. Among the EU countries, the leader in the PV capacity is Germany (32 GW), followed by Italy (16 GW, which covers 6.7% of the country's electricity consumption) [7]. The numbers are still relatively low, but the

growth tendencies are promising. According to some optimistic scenarios, electricity from solar cells could cover 25% of the total electricity demand in Europe in 2030 [8].

The main barrier for PV technology on the way to become competitive has been the *high price* of photovoltaic modules. In Europe, the governments had to subsidize installation of solar cells. However, soon generating electricity with photovoltaic modules will become economically beneficial, *i.e.*, the savings in electricity costs and revenues from selling PV electricity to the grid will be equal or higher than the cost of the PV system installation and maintenance. This highly desirable situation is called '*dynamic grid parity*' and is already achieved in some regions of some countries [7]. The average price for a 3 kW household PV system was 20000€ in 2000, 6000€ in 2012, and expected to decrease to 4500€ in 2020 [8]. The PV generation cost, which includes the investment (buying a PV module) and maintenance costs, and takes into account the lifetime of the module, were estimated to be *ca.* 0.2 €/kWh for Europe in 2011 [9]. The cost of fossil and nuclear energy is presently 0.1-0.2 €/kWh for industry [5], which means that photovoltaics is starting to be competitive on the market.

The other barriers for the PV electricity on the way to become a major energy source are *limited availability* of some materials used in solar cells (for example, Indium, which is used in transparent conductive coatings – but not Silicon), *high energy payback times* for the most common cells (crystalline Silicon, c-Si), *intermittency* of the solar resource, and major *infrastructure investments* needed for a large scale establishment of solar electricity [10]. The scarce material problem might be partly solved by recycling solar cell modules [11]. To resolve the intermittency issue, energy produced by PV has to be stored or transmitted over long distances. Storage in conventional batteries cannot provide all capacity needed [6], and thus storage in a form of fuels (hydrogen) is an attractive option [10], as well as storage as heat to generate steam for steam turbines running an electrical generator during night [12]. National, international and even inter-continental grids could transmit electricity between countries to balance the intermittency in the generation and consumption rates. This will require enormous infrastructure investments, though. Fortunately, the solar and the wind resources often complement each other during the time of a day and over a year (there is usually less sun and more wind during evenings and winters in Europe). Smart integration of photovoltaic and wind energy systems over Europe can realistically provide a large share of these renewable sources in the electricity production, up to 45% in 2030, according to some estimations [8].

There are several types of solar cells that are actively researched today, sometimes referred to as '*generations*'. The '*first generation*' of PV cells is based on *single-crystalline* semiconductors, like Si and GaAs. These solar cells have high efficiencies, long lifetimes and are expensive, since they use crystals of very high quality. In order to reduce the price, the single-crystalline wafers are often substituted with poly-, or multicrystalline Si wafers of a worse quality, which results in solar cells with a lower

efficiency compared to monocrystalline cells. The amounts of material needed in multicrystalline Si cells are the same high as for the monocrystalline solar cells, and therefore they belong to the ‘bulk Si’ group (and are often classified as the ‘first generation’, although this is somewhat ambiguous). The ‘second generation’ of solar cells is also called *thin-film* photovoltaics. These solar cells are also based on inorganic semiconductors, but use less material and of a worse quality than the mono-crystalline PV. The main difference between the two generations is that thin-film solar cells can be produced with relatively cheap fabrication techniques, and on cheap substrates (e. g., glass, steal, and plastic). The ‘second generation’ photovoltaics primarily includes amorphous Si, cadmium telluride (CdTe) and copper indium gallium diselenide (CIGS) solar cells. The ‘third generation’ of PV has an *organic* component in the devices; dye sensitized (or Graetzel) and organic (polymer) solar cells belong to this group. These PV cells are cheap, but their efficiencies and stability (especially of organic solar cells) have to be improved before they enter the PV market. The current PV market is dominated by mono- and multi-crystalline Si solar cells (ca. 82% in 2012 [7]).

There is some ambiguity in classification of solar cells according to ‘generations’. In addition to the one described above, there is an alternative definition for the ‘third generation’ photovoltaics in the literature. According to it, the ‘third generation’ solar cells are those based on novel concepts (for example, multiple carrier generation, hot carrier extraction etc.) that could potentially achieve high efficiencies of 30-40% at low costs [13]. These concepts are still mostly under development. Dye sensitized and organic solar cells belong to the ‘second generation’ in this classification.

Performance of any solar cell is determined by efficiency of two processes: absorption of light via excitation of electron-hole pairs and extraction of these generated charge carriers (electrons and/or holes). For a given material, the light absorption increases with thickness, while the efficiency of extraction of charges is higher in thinner films. Most solar cell types (except monocrystalline ones, where extraction of charges is very efficient) therefore have a thickness that is a compromise between these opposite trends, and would benefit greatly if their thickness could be reduced without decrease in the efficiency. Not only would this lead to smaller amounts of material needed, but also a worse material quality can be tolerated.

A novel way to allow for thinner solar cells, without compromising the light absorption, is to employ the *nanoparticle plasmon resonance* phenomenon, which is in focus in the present work. Localized surface plasmon resonance is a special light-matter interaction occurring in a metal nanostructure, which exhibits interesting optical properties. In particular, the local electromagnetic field around the particle can be orders of magnitude larger than the field from the incoming light that excites the resonance. This locally enhanced field can be used to *promote light absorption* in a semiconductor next to the particle; if plasmonic nanoparticles are placed into a solar cell, its light absorption may also be enhanced. This can produce thinner, cheaper, and

still efficient solar cells. The first part of this thesis (Papers 1 and 2) focuses on employing this effect to increase absorption of light in amorphous Si thin films.

The focus of the second part of this work is on dye-sensitized solar cells. In these solar cells, interactions between the two key components, *i.e.*, organic dye molecules and an inorganic mesoporous film, are not yet fully understood. A part of this thesis is devoted to using the plasmon resonance as a *sensing* tool to give insights into these interactions. The sensing technique utilizes the high sensitivity of nanoparticle plasmon properties to small changes in the surrounding medium. A novel modification of the plasmon sensing idea is applied to investigate diffusion and adsorption of dye molecules into a porous material (TiO₂), which provides valuable information for dye solar cell research.

This thesis is structured in the following way: Section 2 gives a background on the physics of solar cells, and Section 3 continues with an overview of the solar cell types investigated nowadays. Section 4 provides a background of the plasmon resonance physics, and describes the application of plasmon resonance for sensing. Section 5 describes adsorption, desorption and diffusion, concepts and processes that are relevant for preparation of dye-sensitized solar cells. Section 6 gives an overview on mechanisms and achievements in using plasmonics for enhancing light absorption in photovoltaics, with focus on amorphous Si solar cells that are investigated in this work. Section 7 describes the experimental techniques used. Section 8 summarizes the results, and Section 9 presents an outlook.

Throughout the thesis, I tried to gradually introduce the reader to the world of solar cells, plasmons and adsorbing molecules. I hope that in this way, the concepts and their implementations will be understandable also for people with no extensive background in physics or material science.

2. Physics of solar cells

2.1. Solar cells basics

A solar (photovoltaic) cell is a device that generates electricity from light. There are many different kinds of solar cells; the most common type available commercially is crystalline silicon (Si) solar cells (Figure 2.1). These cells usually appear dark blue, because their surface has been treated to minimize reflectance of light in the red part of the spectrum. A grid of metal contacts is fabricated on the surface to allow for collection of the generated electrical power. Under sun light, a solar cell of this type generates a DC voltage of 0.5-1 V and a photocurrent on the order of 10 mA/cm² [14]. The current is reasonable, but the voltage is too low for most applications. To improve the voltage output, the cells are connected in series and encapsulated into modules (Figure 2.1A). A Si solar cell module from Sharp Solar of an area of 1.6 m² consists of 60 solar cells and generates a DC voltage of 30 V and a power of up to 250 W [15].

Since the solar light is a power source with a variable output in time, solar cell modules are usually combined with a battery for storing energy, and with electrical components for regulating power. Solar cells generate DC current, and electrical inverters are used to convert it into AC power, which is much more commonly used. However, especially for off-grid applications, like summer houses with no electricity, sailboats etc, there is also a fast development of components running at 12 V DC to be used in connection with solar cells.

Let us consider general parameters that phenomenologically describe performance



Figure 2.1. (A) A module made of polycrystalline Si solar cells, mounted on a wall of a residential building in Göteborg, close to where the author lives. (B) One of the cells in the module.

of any photovoltaic cell and which are used when comparing solar cells. Any solar cell has a mechanism to separate the excited charge carriers (electrons and holes) that are produced when the cell is illuminated, and drive them in opposite directions. By doing this, a solar cell develops a photovoltage and generates a current. Due to the presence of this separation mechanism (the physical origin of which will be discussed in the following chapters), a solar cell can be represented as a current source connected to a diode (Figure 2.2A). The current-voltage (IV) characteristic of such a system is shown in Figure 2.2B [14]. In dark, the cell behaves as a diode, and under illumination the IV curve is shifted by the value of the current generated by the cell. The maximum voltage is called the *open circuit voltage* V_{oc} and is produced when the two terminals of the cell are isolated (open circuit), providing an infinite resistance. When the terminals are connected together, a maximum current called the *short circuit current* I_{sc} is obtained. The current is roughly proportional to the solar cell area, and therefore the short circuit *current density* J_{sc} , often expressed in mA/cm^2 , is a useful value to compare different solar cells.

When a real load is connected to a solar cell, it develops some intermediate values of the voltage and current, which are determined by the load resistance. There is a set of values of V_m and J_m that produce the maximum power that a cell can deliver (P_{max} in Figure 2.2B). The optimum resistance of the load is therefore V_m/J_m [14]. The *fill factor* is defined as

$$FF = \frac{J_m V_m}{J_{sc} V_{oc}}, \quad (2.1)$$

and describes how close to a square the shape of the IV curve is.

The *energy conversion efficiency* (or often just *efficiency*) η is defined as a ratio of the electric power, supplied by the cell at the maximum power point, to the power of the incident radiation P_{inc} :

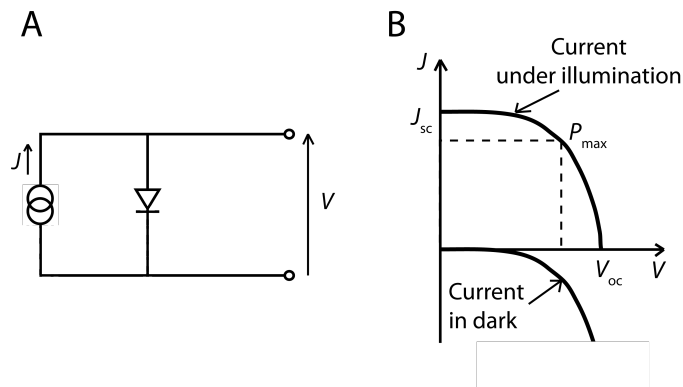


Figure 2.2. (A) Electrical circuit schematically representing a solar cell: a current source in parallel with a diode. (B) Current-voltage characteristics of a solar cell in dark and when illuminated.

$$\eta = \frac{J_m V_m}{P_{\text{inc}}} = \frac{J_{\text{sc}} V_{\text{oc}} FF}{P_{\text{inc}}}, \quad (2.2)$$

The four parameters η , J_{sc} , V_{oc} and FF are the main parameters that describe the performance of a solar cell. To be able to compare different solar cells, the tests should be conducted under standard test conditions, which are: an incident power density of 1000 W/m^2 , temperature 25° C , and the Air Mass 1.5 spectrum [14]. The meaning of this definition of the solar spectrum is described in the next section.

A more ‘microscopic’ characteristic of the solar cell efficiency is the *incident photon to current conversion efficiency (IPCE)*, also called *external quantum efficiency (EQE)*. This is the probability that an incident photon will contribute one electron to the external circuit. The external quantum efficiency is the product of the light absorptance in the active layer of a solar cell, and the efficiency of charge separation and transport to the external circuit.

2.2. The solar spectrum

The Sun is a broad spectral range light source, emitting in the ultraviolet, visible and infrared regions of the electromagnetic spectrum. The power received from the Sun, per unit area (the irradiance), is shown as a function of light wavelength in Figure 2.3. Outside the Earth atmosphere, the solar spectrum is similar to that radiated by a black body at a temperature of $5960 \text{ }^\circ\text{K}$. The value of the solar power density just outside the Earth atmosphere is 1353 W/m^2 [14]. When the sunlight passes through the atmosphere, it is partly absorbed by the atmospheric gases,

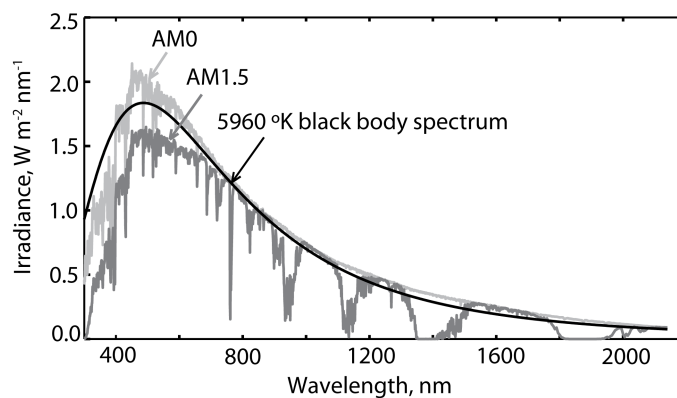


Figure 2.3. Solar spectra AM0 and AM1.5, and the spectrum of a black body of a temperature $5960 \text{ }^\circ\text{K}$. The data for the spectra are taken from [16].

which changes the shape of the spectrum. The ultraviolet radiation below 300 nm is removed primarily by oxygen, ozone and nitrogen, and some of the infrared photons at 1000-2000 nm are absorbed by water. To account for contribution of the atmosphere to the change in the solar spectrum, the Air Mass (AM) coefficient is used. The AM coefficient is defined as the ratio between the optical path length to the Sun and the optical path length when the Sun is directly overhead. Thus, AM1 corresponds to the Sun in zenith, and the extraterrestrial spectrum is called AM0. AM1.5 corresponds to the solar spectrum reaching the Earth surface when the Sun is at an angle of elevation of 42° . AM0 and AM1.5 spectra are shown in Figure 2.3 [16].

Naturally, the solar irradiance varies for different latitudes on Earth, and depends on the time of the day and season. The averaged yearly irradiances vary from less than 100 W/m^2 at high latitudes to over 300 W/m^2 in the sunniest deserts [14]. In Gothenburg, Sweden, the yearly irradiance is approximately 107 W/m^2 (estimated from data in [17]).

The molecules and particles in the Earth atmosphere do not only absorb, but also scatter the solar light. This results in a part of the solar radiation being diffuse, *i.e.*, coming from various angles rather than directly from the Sun. The fraction of the diffuse light is about 15%; it is larger on higher latitudes and in places that are often cloudy [14]. Diffuse light usually cannot be easily accounted for when optimizing a solar cell design.

2.3. Working principles of solar cells

For a solar cell to produce electricity, the following processes have to take place: (i) generation of excited charge carriers as a result of absorption of light, (ii) spatial separation of the generated charges (electrons and holes), and (iii) transport of the charges to solar cell terminals, in the way that electrons preferentially move to one terminal, and holes to the other. This chapter gives an introduction to these processes. Since most solar cells are based on semiconductor materials, we first consider the basics of semiconductor physics.

2.3.1. Physics of semiconductors

When two atoms are brought together in a molecule, their atomic orbitals combine and form pairs of new orbitals, with energies different from those in the individual atoms. Similarly, when many atoms form a crystal, each atomic orbital splits into a

large number of energy levels, which lie very close in energy and effectively form a *band* of allowed energy states. Bands originating from individual atomic orbitals may or may not overlap, and may be occupied by electrons or be empty [14]. The highest occupied band, formed by valence electrons, is called the *valence band*. The lowest unoccupied band (following next in energy after the valence band) is called the *conduction band*.

If the valence band is only partly filled with electrons, or it overlaps in energy with the conduction band, then such a solid is a *metal*. In this case there are free states easily accessible for the valence electrons, into which they can be excited by the thermal energy at ambient temperatures or by external fields. The electrons are thus relatively free to move, and they can conduct heat and electrical current. Since there is no real distinction between valence band and conduction band in metals, the two terms are used interchangeably for metallic materials.

If the valence and conduction bands are separated by a gap of forbidden energy states, called *band gap*, then the solid is a dielectric (insulator) or a semiconductor. (A semiconductor is an insulator at zero temperature, but attains significant conductivity at elevated temperatures.) Semiconductors have a band gap of about 0.5-3 eV, and solids with larger band gaps are usually called dielectrics or insulators. In these materials, the electrons do not have readily available higher energy states to move to, unless the available energy is larger than the band gap. If, however, energy equal to or larger than the band gap is provided, the electrons can be promoted to the conduction band with free states. Such promotion can occur by absorption of photons, which is the basic principle of photoconduction and photovoltaics.

The band structure of ideal solids with a perfect periodic lattice can be calculated exactly. The periodic nature of a crystal makes it possible to solve the Schrödinger equation despite the very large number of electrons. The wave functions of the electrons in a crystal that satisfy the Schrödinger equation are periodic and delocalized, and are therefore usually represented as a periodic part $u_{ik}(\mathbf{r})$, times a plane wave part $\exp(i\mathbf{k}\mathbf{r})$. This form is called a Bloch wave function. For each original orbital i , there is a set of solutions with different wave vectors \mathbf{k} . Energies corresponding to these solutions vary continuously with \mathbf{k} and form an energy band i [14]. $E(\mathbf{k})$, called the dispersion relation for the electrons in the solid, is usually plotted as a function of $|\mathbf{k}|$ for several important directions in a crystal (different directions have different periodicity of the lattice). $E(\mathbf{k})$ is periodic with a periodicity of π/a , where a is the atom spacing in the corresponding direction, and therefore only values $|\mathbf{k}| < \pi/a$ need to be plotted.

Examples of $E(\mathbf{k})$ plots are shown in Figure 2.4. If the minima of the conduction and maxima of the valence bands occur at the same value of \mathbf{k} , the band gap is called *direct* (Figure 2.4A). In this case, the valence electrons can be excited to the

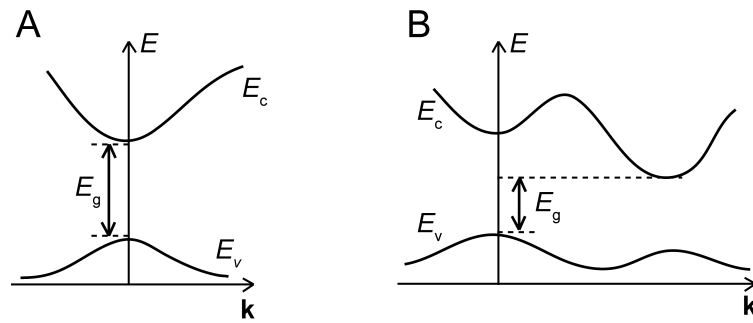


Figure 2.4. Schematic illustration of the band structure of (A) a direct band gap semiconductor and (B) an indirect band gap semiconductor. E_c and E_v are conduction and valence band edges, respectively, and E_g is the band gap.

conduction band when provided sufficient energy, for example, in a form of a photon. This can occur without any change of \mathbf{k} vector. If the minima of the conduction and valence bands occur at different \mathbf{k} , the solid has an *indirect band gap* (Figure 2.4B). To excite electrons from the highest point in the valence band to the lowest point in the conduction band in such materials, both their energy and momentum have to be changed. Photons alone cannot accomplish this, because they have virtually no momentum, and therefore absorption of light happens only if a lattice vibration (phonon) with an appropriate \mathbf{k} is involved [14]. Since the latter is present at any given moment with a non-unity probability, absorption of photons becomes less likely and thus indirect band gap materials have lower absorption coefficients close to the band gap than direct band gap solids. Indirect band gap materials may have a direct band gap of a larger energy, which makes direct transitions possible employing photons of a corresponding energy (Figure 2.4B).

At absolute zero temperature electrons in an *intrinsic* (i.e., with no impurities/dopants that create additional electron energy states) semiconductor occupy all states in the valence band, and the conduction band is empty. The energy up to which the states are occupied is called the *Fermi energy*. At non-zero temperatures, thermal fluctuations in the lattice (phonons) may provide enough energy for an electron to be excited into the conduction band, above the Fermi level. An excitation from the valence to the conduction band leaves a vacancy, ‘hole’, in the valence band, which can move and conduct electricity (in reality, it is *electrons* from the neighbouring states that move and occupy the hole, but since these electrons are much more abundant than the hole, it is more convenient to describe what happens to the hole instead).

Thermal excitations in an intrinsic semiconductor provide only a minor amount of excited electrons and holes at practical temperatures and band gap values; to increase their quantity sufficiently in a controlled manner, a semiconductor is *doped*. Doping means introducing a small (compared to the host material) number of impurity atoms

into an otherwise homogeneous crystal in order to change its electronic properties. Dopants introduce new energy levels into the band gap of a crystal as described below. Typical concentrations of dopants are 10^{-7} - $10^{-3}\%$ of the total number of atoms.

Consider a small amount of an element with 5 valence electrons, such as phosphorous (P), added to a silicon crystal, which has 4 valence electrons per atom [18]. 4 of the electrons from P take part in the covalent bonding with Si, leaving the fifth electron loosely bound to the P ion. The energy of this electron is higher than that of the valence electrons in Si. Its energy level actually lies just below the bottom of the conduction band in Si, and addition of some small amount of thermal energy is enough to excite it into the conduction band. Thus, in this case the P atoms *donate* electrons to the Si conduction band, producing immobilized positive ions (holes) with electronic states in the bandgap, but no holes in the valence band (Figure 2.5A), and mobile electrons in the conduction band. The Si with donor atoms becomes *n-type*, which means that the negative charge carriers (electrons) are the majority carriers. The Fermi level E_F of an n-doped material lies close to the conduction band edge.

Similarly, if an element with 3 valence electrons, as for example boron (B), is added to the Si, the B-Si bonds will lack an electron, creating a hole, which lies in the band gap above, but close to the top of the valence band. By thermal energy fluctuations, a valence electron can be excited to a Boron-induced hole state and occupy this state, creating a negative ion (Figure 2.5B). In this way a mobile hole is formed in the valence band, while the negatively charged B ion with its extra electron are immobile. The produced semiconductor material is of *p-type*, the name indicating that the main charge carriers are positive. The Fermi energy E_F of such a material is located close to the valence band edge.

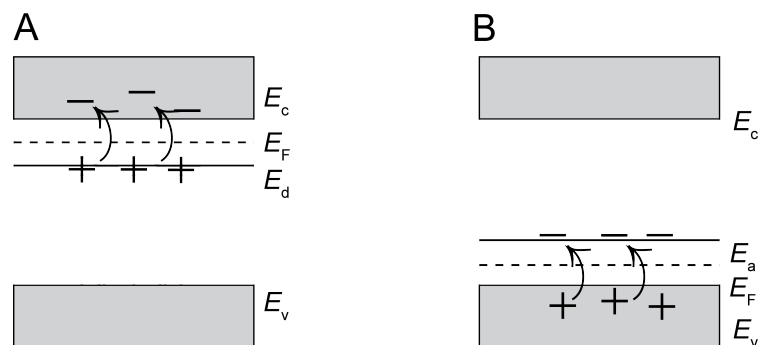


Figure 2.5. Illustration of doping effects in a semiconductor. (A) Generation of electrons in the conduction band via doping with donor atoms with energy levels E_d . (B) Generation of holes in the valence band by doping with acceptor atoms having energy levels E_a .

Real crystals almost always have defects, like impurity atoms, vacancies, dislocations etc., which can introduce energy levels into the band gap. Even in a high quality monocrystalline semiconductor, structural defects arise from broken bonds and surface states, which are naturally different from those in the bulk. In polycrystalline materials, defects are concentrated mostly at grain boundaries. The energy states in the band gap originating from defects often act as recombination centers and are therefore undesirable (but mostly unavoidable) for solar cells, since they reduce the lifetime and transport lengths of the charge carriers.

2.3.2. Absorption of light: photogeneration of charge carriers and recombination

A photovoltaic material utilizes the solar energy by absorbing the solar light through excitation of charge carriers. If the carriers produced in this way can move freely this process is called photogeneration of charge carriers. Most often, this implies transition of electrons into the conduction band, which creates an electron-hole pair, but can also include excitations to and from localized states in the band gap, which generate only one type of charge carrier. Recombination is a reverse process compared to generation.

The band gap is of ultimate importance to the solar cell function, since its presence increases the recombination time, *i.e.*, the lifetime of the charge carriers. Electrons can remain in the excited states long enough to be extracted and subsequently used to create voltage and current, *i.e.*, electrical power. If electrons are instead excited to energy levels which have many empty neighbouring states (as in metals), they will lose the excessive energy much faster, on the order of a few to a few tens of femtoseconds [14]. This also occurs whenever electrons are excited into higher energies within the conduction band of a semiconductor; the electrons dissipate the energy very fast and end up at the bottom of the conduction band. This process is very difficult to avoid, and it fundamentally limits the efficiency of solar cells, since the energy that photons have in excess of the band gap energy is usually lost as heat. The impact of this process along with other loss processes on the solar cell efficiency is discussed in Section 2.3.4.

The probability of absorption of a photon with energy E is described by the absorption coefficient $\alpha(E)$, which is a material specific property. Since absorption leads to generation of an electron-hole pair (in an ideal semiconductor), $\alpha(E)$ is proportional to the density of occupied states in the valence band, where a hole is produced, and the density of empty states in the conduction band, to which an electron is excited [2]. If $\alpha(E)$ is uniform throughout the material, then the intensity of light after passing through a material slab of thickness x is $I = I_0 \exp(-\alpha x)$, where I_0 is

the intensity at the entrance. $\alpha(E)$ is related to the imaginary part of the refractive index k as

$$\alpha = \frac{4\pi k}{\lambda}. \quad (2.3)$$

It can be shown [14] that for direct band gap semiconductors $\alpha(E)$ close to the band gap energies E_g varies as

$$\alpha \sim \sqrt{E - E_g}, \quad (2.4)$$

and for indirect band gap semiconductors as

$$\alpha \sim (E - E_g)^2. \quad (2.5)$$

These dependences reflect a more gradual increase in $\alpha(E)$ with energy for indirect band gap materials compared to direct band gap ones. This is in line with the physical picture of decreased probability of indirect transitions discussed in Section 2.3.1.

If we assume that all photons absorbed by a solar cell material generate one electron-hole pair each, then the rate of carrier generation per unit volume, at a depth x below the surface is

$$g(E, x) = b(E, x)\alpha(E, x), \quad (2.6)$$

where $b(E, x)$ is the *flux* of photons with energies E at position x [14]. It is the number of photons and not their energy that determines the photogeneration rate. $b(E, x)$ is the photon flux after the incident flux $b_0(E)$ has been partly reflected with probability $R(E)$ and partly absorbed by the material until position x . After taking this into account, the photogeneration rate becomes

$$g(E, x) = (1 - R(E))\alpha(E, x)b_0(E)\exp\left(-\int_0^x \alpha(E, x')dx'\right). \quad (2.7)$$

To get the total photogeneration rate, (2.7) has to be integrated over the part of the solar spectrum, where absorption results in generation of free carriers [14].

Recombination results in loss of mobile electrons or holes, and can happen via several mechanisms. *Radiative recombination* is a relaxation of an electron from the conduction band to the valence band by emission of a photon. The rate of this process is proportional to the densities of both electrons and holes, and it is more important in materials with a high absorption coefficient. Radiative recombination is important in the limit of perfect materials, but plays a minor role in practical solar cells at operating point [14]. *Auger recombination* involves three charge carriers; two carriers of opposite polarity recombine, and the released energy is used to excite the third carrier to a higher kinetic energy state. This energy is eventually lost as heat when the excited

carrier relaxes to the band edge. The rate of Auger process is proportional to the densities of all three carriers, and it is therefore important in materials where carrier densities are high. Contrary to radiative recombination, it occurs with high probability in indirect band gap materials, and plays a major role in very pure Si crystals. *Shockley Read Hall recombination* involves defect states in the band gap, and it is the dominant loss mechanism in real solar cells [14]. Defect states are spatially localized, and can be thought of as *traps*, which can capture mobile carriers. The carriers can then, after trapping, be released by thermal activation. If however two carriers of opposite polarity are captured, they will recombine. This is more likely for defect states lying deep in the band gap, and therefore these states are called *recombination centres*.

2.3.3. Separation of charge carriers: junctions

The key process in any solar cell is separation of the electrons and holes generated by absorption of light, which builds up an electric potential, able to perform work. The separation is achieved through a built-in electric field or a designed alignment of energy levels of two materials, which enables traveling of carriers of one sign (+ or -) in one direction and produces a barrier in the other direction. The implementation of these mechanisms is described below, and examples of solar cells using these principles are given in Section 3.

A classical and efficient way of establishing an electric field inside a semiconductor is by using a *p-n junction*. A p-n junction is a basic structure of monocrystalline solar cells, like Si and GaAs. When a p-type and an n-type material are brought into physical contact at the atomic level, at first a very large density gradient in the electron and hole concentrations is established, which causes carriers from each region to move toward the other region. Near the junction, the electrons and holes recombine, leaving the fixed donor positive ions and acceptor negative ions in the corresponding regions (Figure 2.6A). The zone near the junction is free from mobile charges, and is called the *depletion region*. The immobile ions in this region form an electric field, which prevents the movement of free electrons from the n- to the p-side of the junction, and holes in the opposite direction [18].

In the alternative energy picture, the Fermi level of an n-doped region lies higher than the Fermi level of a p-region before the materials are brought into contact. Since the Fermi levels align at a constant energy once the materials are in contact, the conduction and valence band edges need to shift (bend) in the depletion region (Figure 2.6B). The energy of electrons on the p-side is higher than on the n-side, so

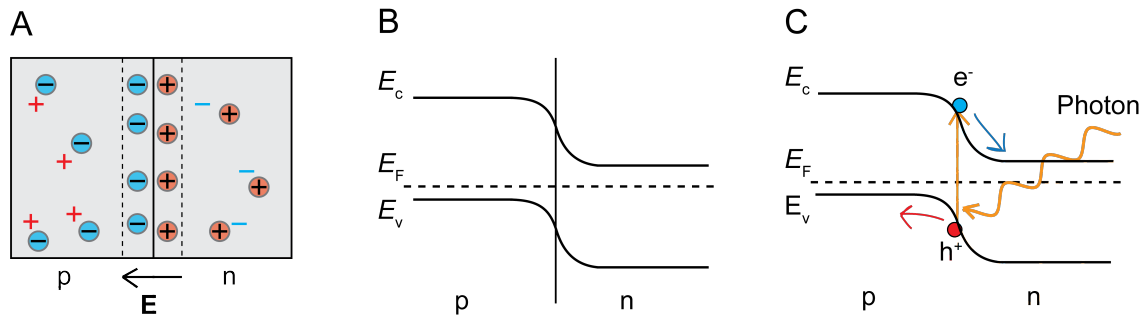


Figure 2.6. (A) Mobile and fixed (the latter shown in circles) electrons and holes in a p-n junction. **E** shows the direction of the built-in electric field. Energy diagram of a p-n junction (B) in dark and (C) under illumination.

they tend to move toward the n-type region, and holes are in the symmetric situation. However, in dark the concentration of the electrons in the p-region (and the holes in the n-region) is very small, and the conductivity through the junction is very low. The situation changes when the p-n junction is illuminated. Absorption of light by both p- and n-regions populates the corresponding conduction bands, and the generated electrons diffuse to the n-type region, and the holes to the p-type region. If the p-n junction is connected to an external circuit, a photocurrent will flow and so the junction will function as a solar cell generating electricity.

In a p-n junction structure, there are large regions without a built-in field (corresponding to the flat band regions in Figure 2.6B). In these regions, there are significant numbers of corresponding majority carriers (electrons in n-type, and holes in p-type material). The charge carriers generated by illumination cannot substantially increase these majority carrier populations [19]. However, electrons produced in the p-type, and holes generated in the n-type region, do increase the corresponding *minority* carrier populations significantly. These carriers have to diffuse to the junction, from where they are swept by the built-in electric field to the other side.

A variation of a p-n junction is a *p-i-n junction*, which is of particular importance to amorphous Si solar cells. This junction has an intrinsic (i), which means undoped, material in between the p- and n-regions. The junction is established in a similar way to a p-n junction, but the electric field extends now over a larger volume, the whole i-region (Figure 2.7). This structure is beneficial in semiconductors with large number of defects, which is further increased by doping, so that the lifetime of excited carriers in doped regions is very short. The carriers are generated mostly in the i-region and can diffuse longer distances than in doped regions.

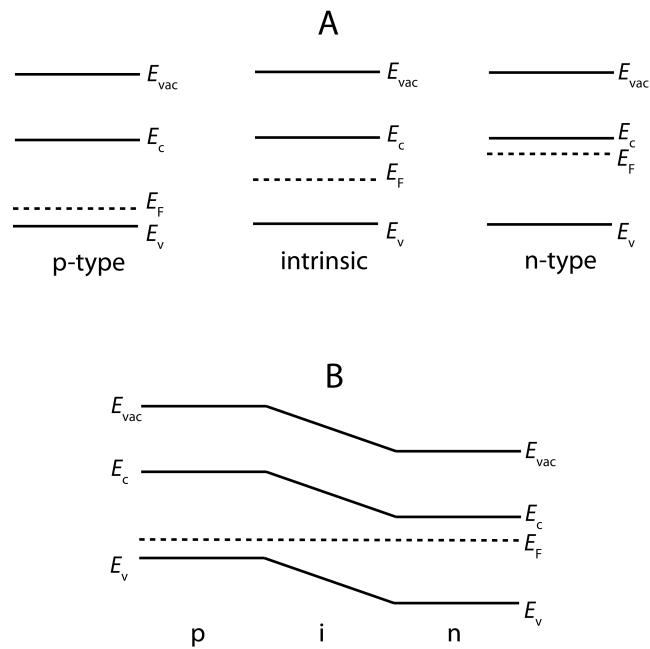


Figure 2.7. Band structures of p-, i- and n-type materials (A) in isolation and (B) when brought together in a p-i-n junction.

A p-n junction can also be made between two different materials (a *heterojunction*). In this case, the driving force for separating charges originates from both a built-in electric field and a difference in conduction band positions of the two materials. Heterojunctions form basics for *thin-film solar cells* like CdS/CdTe and CdS/CuInGaSe₂.

Similar heterojunctions between molecular materials are used in *organic solar cells* (Figure 2.8A). A substantial difference between organic and non-organic semiconductor junctions is that in the former, absorption of light generates excitons, which are electron-hole pairs bound by Coulomb's force (as opposed to free electrons and holes in non-organic semiconductors). Excitons drift in the material, and only split when they reach the junction. To overcome the problem of short diffusion length of excitons (typically on the order of 10 nm), the two organic materials are blended into a *bulk heterojunction* (Figure 2.8B). The same principle is used in *dye sensitized solar cells*, where the junction is formed between a molecular absorber (dye) and a porous semiconductor.

All types of solar cells mentioned in this section are discussed in more detail in Section 3.

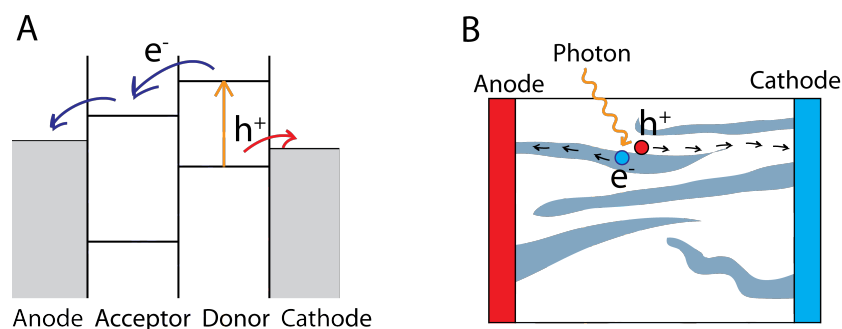


Figure 2.8. (A) Band profile of a heterojunction between two organic materials. The donor absorbs a photon (yellow arrow), and the generated electron and hole migrate to different electrodes. (B) Schematics of a bulk heterojunction. (Figures are redrawn from [14]).

2.3.4. Efficiency limitations for solar cells

The power delivered by a solar cell can be expressed as the product of the generated current and voltage at the maximum power point, as discussed in Section 2.1. The current is proportional to the number of absorbed photons, and would be maximal for a material with a band gap that approaches zero (which however cannot function as a solar cell material for the reasons discussed in Section 2.3.2). The photovoltage, however, decreases with decreasing band gap. Therefore there must be an optimal band gap for photovoltaic devices, which was first calculated by Shockley and Queisser [20] in an approximation that the Sun is a black body source with a temperature of 6000 °K. Under assumption that each photon with energy larger than the band gap E_g produces one electronic charge at voltage E_g , and photons with $E < E_g$ do not contribute, the authors arrived at 44% maximal efficiency for a band gap of 1.1 eV [20].

However, the radiative recombination is an inevitable loss mechanism, which comes from the fact that an absorber has a non-zero probability of emitting light through recombination of the excited charge carriers. Moreover, since a solar cell has a non-zero temperature, it will emit black-body radiation corresponding to this temperature as well. These processes lower the maximal attainable current and voltage and therefore also the efficiency. Taking this into account, Shockley and Queisser calculated an efficiency limit of approximately 33% for a material with a band gap of *ca.* 1.3 eV [20]. Würfel used a slightly different approach, but arrived to very similar results [2]. Figure 2.9A shows the maximal achievable efficiency for a single band gap (single-junction) solar cell as a function of the band gap, and suggests that band gaps from 1 to 1.5 eV are the most efficient. Crystalline Si and GaAs have band gaps in this region.

While maximum 33% of the solar power can be utilized by a single-junction solar cell, ca. 21% of the solar radiation is lost because photons with $E < E_g$ are not absorbed [21]. This decreases the current that a solar cell produces. Approximately 23% of the solar power is lost due to relaxation of photons with $E > E_g$ to the band gap edge (also called *thermalisation*), which reduces the maximum achievable voltage so that it cannot be larger than the band gap. Similar numbers can be estimated from Figure 2.9B, taken from Hirst and Ekins-Daukes [22], who calculated the contribution of different loss mechanisms as a function of the band gap. The *inevitable emission* (radiative recombination) loss adds only a few percent to the total loss. The *Carnot loss* comes about if a solar cell is considered as a heat engine with heat flowing from a hot reservoir (the Sun) to a cold reservoir (the atmosphere) and work is done in the process [22]. In this case some energy is lost to the cold reservoir, which in the solar cell context leads to a decrease in the maximum achievable voltage. The *Boltzmann loss* originates from the fact that the light from the Sun comes to a solar cell in a very small solid angle, while the solar cell radiates into a large angle (basically all around). This is schematically shown in Figure 2.9C.

According to Polman and Atwater [23], these loss mechanisms decrease the maximum open-circuit voltage V_{oc} from the band gap value according to:

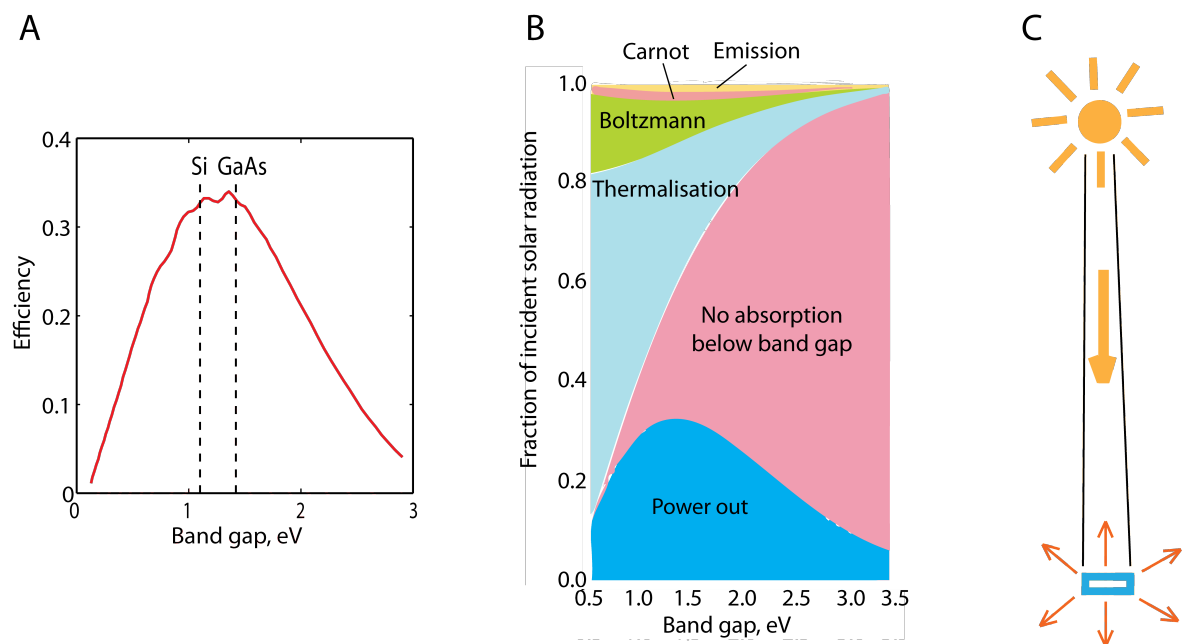


Figure 2.9. (A) Efficiency of ideal solar cells, where the only loss mechanism is radiative recombination, as a function of the band gap magnitude (redrawn from [2]). (B) Intrinsic loss processes in solar cells (redrawn from [22]). (C) Schematics of the angles of absorption and emission by a solar cell.

$$eV_{oc} = E_g \left(1 - \frac{T_A}{T_{Sun}}\right) - kT_A \left[\ln\left(\frac{\Omega_{emit}}{\Omega_{abs}}\right) + \ln\left(\frac{4n^2}{I}\right) - \ln(QE) \right], \quad (2.8)$$

where the first term is the Carnot factor with T_A being the temperature of the absorber and T_{Sun} the temperature of the Sun. The Carnot loss reduces the voltage by ca. 5% compared to the band gap at room temperature, and by additional 7% if the spontaneous emission of photons (and not only the black-body radiation) is also accounted for [23]. The terms in square brackets are related to an increase in the entropy of light. The first of them is what was called the Boltzmann loss above, and it reduces the V_{oc} by ca. 0.3 V [23]. The second term in square braces, where n is the refractive index of the absorber and I is the light concentration factor, describes the result of incomplete light trapping inside the absorber. If there is no light trapping (like in a planar solar cell), then $I = 1$ and the corresponding loss in V_{oc} is approximately 0.1 V [23]. In a classically optimized cell, $I = 4n^2$ can be achieved and then this loss vanishes. Novel light trapping methods, for example plasmonic enhancement effects as described in this thesis, may lead to even higher light trapping factors and thus increase the V_{oc} . Finally, the last term in the square brackets in equation (2.8) originates from non-radiative recombination (which may happen via pathways discussed in Section 2.3.2). The quantum efficiency for it is defined as $QE = R_{rad} / (R_{rad} + R_{non-rad})$, where R_{rad} and $R_{non-rad}$ are the rates for radiative and non-radiative recombination, respectively. This will normally not provide a loss over 0.1 V. As a result of all the loss mechanisms presented in equation (2.8), the maximum V_{oc} is usually 0.4-0.5 V lower than the band gap for almost all solar cell materials [23].

It has been realized that it is possible to overcome some of these intrinsic losses and achieve solar cell efficiencies above the Shockley-Queisser limit. The largest loss contributions are the absence of absorption below the band gap and the thermal relaxation of carriers excited with energies above the band gap. These losses can be decreased if a solar cell has a number of layers with different band gaps, each absorbing its fraction of the solar spectrum. In this way, both the current and voltage can hypothetically be increased, due to absorbing more photons and extracting them at higher energies, respectively. This idea has been around for a long while and it is referred to as the *multijunction solar cell* concept. The best confirmed efficiency of such a cell is 37.9% (the cell is InGaP/GaAs/InGaAs) [24]. However, if the parts of the solar cell with different band gaps are stacked on top of each other, as it is usually done, then the generated current is equal to the lowest current among those from the subcells. An alternative is to place the subcells in an optically parallel configuration [23], which would remove the requirement of current matching, but at the same time would introduce the need of a spectrum-splitting device and also increase the area occupied by solar cells.

Another way to decrease the loss associated with thermalisation of excited carriers to the band edge is to try to extract the electrons and holes before they go through

the thermal relaxation process. This is the idea with the *hot carrier solar cell* concept, the name coming from the hope that the excited electron population stays at a higher temperature than the temperature of the lattice, before being extracted to the external circuit. However, a recent work by Kirk and Fischetti [25] theoretically estimated the efficiency of hot carrier extraction and arrived to a pessimistic conclusion that such cells cannot successfully compete with the conventional cells even if all conditions are optimized. The problem originates mainly from the fact that it is highly improbable that the excited carriers end up having energies in a narrow range away from the band gap, which is required for successful extraction [25].

In order to decrease the Boltzmann loss, an interesting idea is to limit the angle of re-radiation of energy by a solar cell. A recent study by Kosten *et al.* [26] investigated the influence of light trapping and limited re-radiation angle on the efficiency of a thin GaAs solar cell and predicted the efficiency of 38% for such an optimized single-junction solar cell - which is above the Shockley-Queisser limit. Microparabolic light reflector structures placed on top of a solar cell were suggested in order to direct the emission of light [26].

3. Solar cell research: achievements and challenges

This section gives an overview of the main types of solar cells investigated nowadays. Crystalline solar cells, sometimes referred to as ‘first generation’ of photovoltaics, are described in Section 3.1. Thin film solar cells, constituting the ‘second generation’, are discussed in Section 3.2. Organic and dye-sensitized solar cells, which involve molecular components, belong to the ‘third generation’ and are described in Section 3.3. Amorphous silicon and dye solar cells are discussed in more detail, since they are investigated in the present work.

3.1. Crystalline solar cells

Monocrystalline solar cells belong to the first generation of photovoltaic devices. They still dominate the market and have the highest efficiencies of all solar cells. These cells are based on a silicon (rarely also GaAs, in specialized applications) p-n homojunction fabricated on a high quality monocrystalline wafer, which ensures very good performance but also leads to comparatively high costs. The most common monocrystalline cells based on Si and GaAs are described in the next sections.

3.1.1. Single- and polycrystalline Si solar cell

Silicon has many advantages: it is an abundant, non-toxic material, with the energy band gap (1.1 eV) lying in the favourable range for solar cells. In air Si forms an oxide layer, which is very stable and protects it from further oxidation (this oxide is central in the MOS/MOS-FET technology in microelectronics). Silicon has been investigated very thoroughly for microelectronics applications, and the accumulated knowledge significantly accelerated development of crystalline Si solar cells, especially in the beginning. The disadvantages of crystalline Si are low absorption coefficient, resulting from the indirect band gap, and relatively high cost. Because of the poor absorptance¹, Si has to be thick (about 500 μm) to capture sufficient amount of light, which in turn requires highly pure and defect-free crystals in order to collect the charge carriers at the distant contacts.

¹ Absorptance is the fraction of the light absorbed, *i.e.* the ratio between the intensity of the light that is absorbed, and the intensity of the incoming light.

Si reflects *ca.* 30-40% of solar light, and to prevent this, antireflection coatings and/or surface texturing are often used [27]. An antireflection coating is a thin film of a dielectric, the thickness of which is optimized to minimize reflectance of the system at a region around a particular wavelength. Improved reflectance at a wider spectral band can be achieved using several thin films, in a sandwich coating. Antireflection coatings for Si solar cells are usually based on TiO_2 or Si_3N_4 , and optimized for reducing reflectance in the red and infrared parts of the spectrum [14]. Texturing of the front and/or back surfaces of the cell reduces reflectance too, and can additionally cause multiple reflections inside the cell, increasing the path of light and therefore the probability of absorption. Pyramids arranged in regular patterns can increase the mean light path in a Si solar cell by a factor up to 50 [2, 28].

The maximal achievable efficiency of a *Si single-crystalline solar cell* under AM1.5 illumination was predicted to be 29.8% [29]. The best experimentally demonstrated efficiency of 25.0% [24], achieved by Green and co-workers in 1998 [30], is quite close to this limit. The structure of this cell is shown in Figure 3.1. It is based on a p-doped Si wafer, which forms a junction with the front n-doped layer. Heavily doped n- and p-regions (marked as n^+ and p^+) are included close to the cell contacts to improve the resistance. The metal layer on the back surface serves both as an electrode and as a mirror reflecting photons, which have not been absorbed, to increase their path in the cell. The front surface is textured with pyramidal structures, coated with an antireflection coating, and finished with metal finger electrodes for collecting current. The best demonstrated efficiency for a module based on similar solar cells is 22.9% [24].

A large part of the Si solar cells produced today is based on *polycrystalline* (or *multicrystalline*) Si, with the solar cell structures that are very similar to those of single-crystalline Si cells. The polycrystalline Si consists of large crystalline grains and is produced *via* a less demanding and energy-consuming technique compared to the

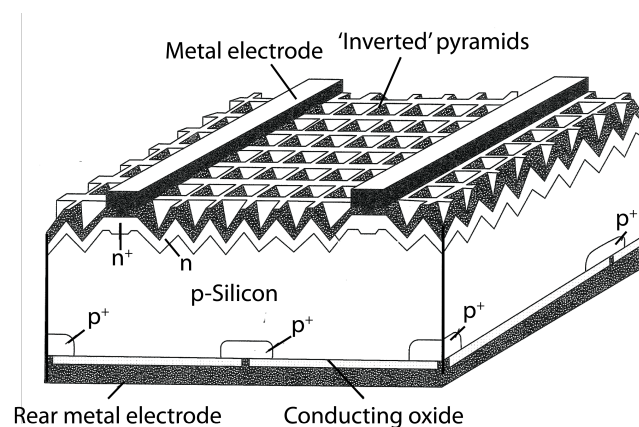


Figure 3.1. Schematics of the Si solar cell with the best efficiency of 24.4% (adapted from [2]).

monocrystalline counterpart. This makes it cheaper than the monocrystalline Si, but the corresponding solar cell efficiencies are lower too [27]. The optical properties of the polycrystalline Si are similar to those of the monocrystalline Si, which means that thick wafers (about 0.3 mm) are needed for sufficiently high light absorption. The charge carrier transport in polycrystalline Si is lower compared to crystalline Si, due to presence of charge carrier traps at the grain boundaries, and also point defects and impurities, which reduces the solar cell efficiency. The best achieved single multicrystalline Si solar cell efficiency is 20.4 %, and the highest module efficiency is 18.5% [24]. Polycrystalline Si can also be fabricated on glass substrates (as opposed to wafers cut out from large ingots crystallized from molten Si) by deposition of an amorphous Si film and subsequent annealing. Solar cells of this type belong to the ‘thin-film Si’ group (although this division is somewhat diffuse in this particular case) and are described in Section 3.2.3.

3.1.2. III-V crystalline solar cells

Another group of crystalline solar cells of high efficiencies and high production costs is *III-V semiconductor alloys*, containing elements from groups III and V of the periodic table. These include gallium arsenide (GaAs), indium phosphide (InP), and also several types of ternary alloys, like indium gallium phosphide ($\text{In}_x\text{Ga}_{1-x}\text{P}$). These materials are direct band gap semiconductors, and have therefore much higher absorption coefficients than Si.

GaAs is the most widely used material for the III-V solar cells. It has a band gap of 1.4 eV, which is very close to the optimal band gap (see Figure 2.9A), and a high absorption coefficient, which allows harvesting most of the photons with energies above the band gap in a cell of thickness of several μm . In spite of being much thinner, GaAs solar cells are about 5 to 10 times more expensive than crystalline Si cells, and are therefore used mostly in space applications, where weight and efficiency matter more than the cost [14]. The best achieved efficiency of a GaAs solar cell is 28.8% (and 24.1% for a module) [24], which is very close to the theoretical limit of 31%. This is also the general record in efficiency of single-junction solar cells.

Since the best achieved efficiencies of crystalline Si and GaAs solar cells are already very close to the theoretically predicted limits, the main efforts are focused on fabricating the materials and the cells in a cheaper way. At the same time, alternative, cheaper solar cell types are being developed. They are discussed in the following sections.

3.2. Thin-film solar cells

Similarly to the monocrystalline photovoltaics, thin-film solar cells are based on p-n junctions between inorganic semiconductors. The materials used have direct band gaps and high absorption coefficients, which allow absorbing a significant amount of light in thin (several μm) solar cells. Since generated charge carriers do not have to travel very long distances to be collected at the contacts, due to the much thinner p- and n-layers, poorer electronic quality of the materials can be tolerated. This allows fabricating solar cells using relatively cheap deposition methods, and on cheap substrates (like glass and plastic). The term ‘thin’ actually refers more to fabrication methods with mass-production possibilities rather than to the thickness; monocrystalline GaAs solar cells are similarly thin, but are not included in this class. Interestingly, it is often the inactive solar cell components (e.g., substrates and sealants), and not the functional layers (like semiconductor films and electrodes), that contribute most to the cost of thin film solar cells [31].

The most researched thin-film solar cells are based on *cadmium telluride* (CdTe), *copper indium gallium diselenide* (CuInGaSe_2 , or CIGS), and *amorphous and microcrystalline hydrogenated silicon* (a-Si:H and $\mu\text{c-Si:H}$, respectively). The first two types are described briefly below, and the silicon-based solar cells are discussed in more detail, since they are important for the present work.

3.2.1. CdTe and CIGS solar cells

CdTe is a semiconductor with a direct band gap of approximately 1.4 eV and a very high absorption coefficient [14]. It is usually used in a junction with cadmium sulfide (CdS). Both materials are slightly non-stoichiometric, which conveniently produces p-type doping of CdTe, and n-type doping of CdS without a need for external dopant atoms [32]. The CdTe film has a thickness of 2-5 μm , and performs the function of light absorption, while the CdS layer of *ca.* 100 nm is used to form the junction. The best demonstrated efficiency of a single CdTe/CdS solar cell is 19.6% (16.1% for a module) [24]. The rather high efficiency for relatively cheap thin film solar cells led to their commercialization. However, usage of highly toxic Cd in a ‘green’ energy source, and also scarcity of Te may substantially limit the production of these solar cells in the future.

CuInSe_2 (CIS) has a direct band gap of approximately 1 eV and an absorption coefficient that is almost the highest known among inorganic semiconductors [14]. Usually some Ga is added to CIS, and the resulting p-type material CuInGaSe_2 (CIGS) is used in a junction with an n-type CdS film. The principle structure and characteristic thicknesses of CIGS cells are similar to those of CdTe/CdS solar cells. The best confirmed efficiency for CIGS solar cells is 19.6%, and the highest module efficiency is

15.7% [24]. CIGS cells with high efficiency of 17% can also be fabricated on flexible substrates [33]. The main problems of CIGS solar cells is the complicated deposition process of the multi-element alloy CIGS, which imposes challenges for realization of uniform coatings in large-scale production, and also the use of toxic Cd and the scarce element In [32].

3.2.2. Amorphous silicon solar cells

In amorphous materials, the bond lengths and number vary slightly for different atoms in the lattice. The coordination of bonds of an atom with its closest neighbours is almost the same as in the corresponding crystalline material, but is gradually lost with more distant neighbours. In other words, in the amorphous material, the short range order (nearest and next nearest neighbours) is quite similar, but not identical to the crystalline material, while there is no long range order that can be described by simple lattice (translation) vectors etc. This loss of order makes the momentum of the energy states largely undetermined, and therefore no phonons are required for transitions between the states [2]. Thus amorphous Si (a-Si) is a direct band semiconductor - unlike crystalline Si, and has a high absorption coefficient.

The most numerous defect type, crucial for use of a-Si in solar cells, is a *dangling bond*, which is a vacant valence electron not used in bonding with neighbouring atoms (Figure 3.2A). Presence of dangling bonds produces numerous defects in the band gap, which function as traps and recombination centres and drastically decrease the charge carriers lifetime and mobility. Moreover, such material cannot be doped, since the extra carriers introduced by dopants will likely be captured by the defects [14]. To improve this situation, hydrogen (H) is incorporated into a-Si during fabrication. H

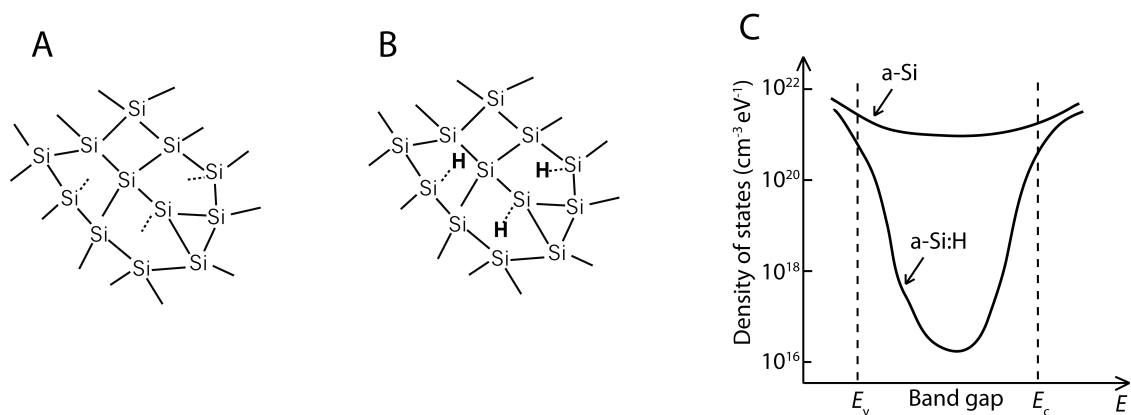


Figure 3.2. (A) Schematics of amorphous Si containing dangling bonds. (B) The dangling bonds are saturated by hydrogen atoms in a-Si:H. (C) Schematics of density of states in a-Si and a-Si:H (redrawn from [34]).

atoms form bonds with the unpaired electrons and remove their capacity to trap charge carriers (Figure 3.2B). The density of dangling bonds in a-Si is approximately 10^{20} cm^{-3} , which is about 1% of the Si atom density, and in the *hydrogenated amorphous Si* (a-Si:H) containing 5-15% of H this density can be decreased to 10^{16} cm^{-3} [34]. This is illustrated in Figure 3.2C.

Passivation of a-Si with H leads to a substantial increase in the band gap, which changes from *ca.* 1.1 eV for a-Si to *ca.* 1.7 eV for a-Si:H [27]. The defect states that remain after passivation hinder transport of charge carriers in a-Si:H. The carriers move either by ‘hopping’ between localized defect states with energies in the band gap, or in the conduction band, being periodically trapped by defects and thermally activated back to the conduction band. In undoped a-Si:H the carrier lifetimes are 10^{-8} – 10^{-6} s and the diffusion lengths are *ca.* 100 nm [14, 35]. The corresponding numbers for monocrystalline Si are *ca.* 10^{-4} s and more than 200 μm , respectively [36, 37].

Addition of H to a-Si makes doping possible, although the carrier diffusion lengths and lifetimes are much reduced in doped a-Si:H. Collection of current from a p-n junction would thus be very poor, and therefore a-Si:H solar cells are based on *p-i-n junctions*, discussed in Section 2.3.3. The doped regions are usually made thin (10-20 nm), and the thickness of the intrinsic layer is chosen to maximize current generation. Here, the thickness is a trade-off between light absorption, which benefits from thick films, and charge carrier collection, which is favoured by thin films.

Schematics of a state-of-art a-Si:H solar cell is shown in Figure 3.3A [32]. The front layer is a transparent conductive oxide (TCO), which is a dielectric doped in a way that improves conductivity while maintaining transparency. This layer is made rough to enhance light scattering into the cell and thereby increase the light path length, which leads to an improved absorption. A p-i-n structure is deposited afterwards, most often by a plasma enhanced chemical vapour deposition (PECVD) from a silane (SiH_4) gas. The details of this process are described in Section 7.1.4. The doped layers can be a-Si:H alloys or microcrystalline Si. The rear contact is composed of another TCO film and a metal electrode, which also serves as a reflector.

The major problem of the amorphous Si solar technology is light-induced degradation of a-Si:H films, known as the *Staebler-Wronski effect* [38]. Under light exposure, the density of defects in a-Si:H increases, which drastically deteriorates performance of solar cells during the first months of operation. The performance stabilizes afterwards, but the stabilized efficiencies are much lower than the ‘fresh’ cell efficiency. There is no full understanding of the mechanism of Staebler-Wronski effect yet, but it is believed that H atoms play an important role in it [38]. The light-induced degradation decreases with decreasing the intrinsic layer thickness [35], which additionally motivates developing *thin* a-Si:H solar cells (as addressed in this work; Papers 1 and 2).

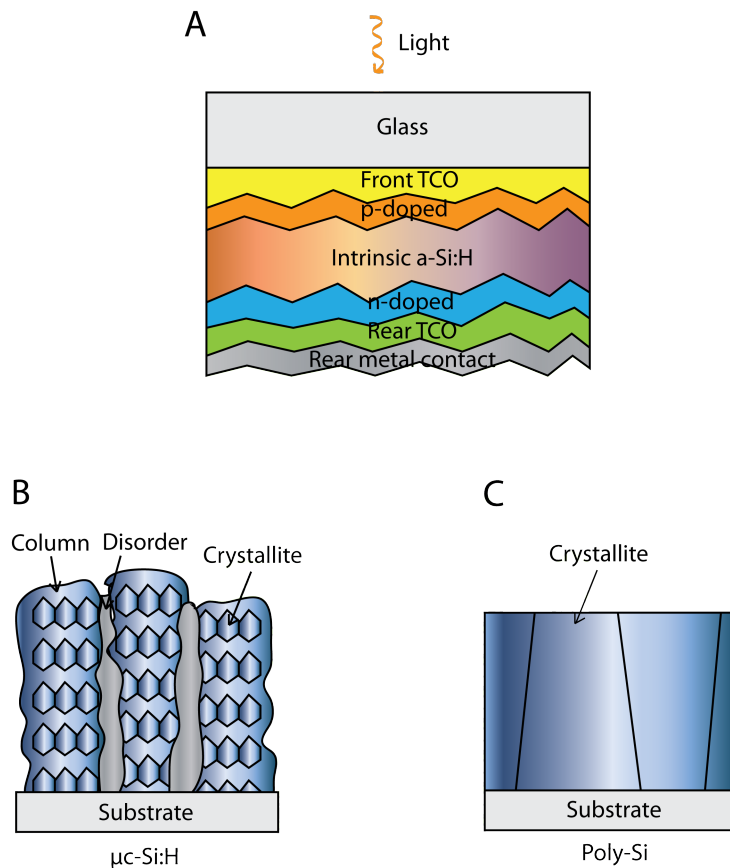


Figure 3.3. Schematics of (A) a state-of-art a-Si:H solar cell (redrawn from [32]), (B) a microcrystalline Si film and (C) silicon layers used in ‘crystalline silicon on glass’ solar cells (redrawn from [27]).

The highest confirmed efficiency of a stabilized single a-Si:H solar cell is 10.1% [24].

3.2.3. Micro- and polycrystalline silicon solar cells

Parameters of the PECVD deposition process can be adjusted to produce microcrystalline Si films ($\mu\text{c-Si:H}$; sometimes also called nanocrystalline Si). These films are made of long columns containing crystalline grains, the spaces in between which are filled with amorphous silicon and/or voids (Figure 3.3B). The band gap is approximately 1.0 eV, which is close to that of the crystalline Si. Single-junction $\mu\text{c-Si:H}$ cells have recently reached the efficiency of 10.7% using only 1.8 μm of Si [39]. However, it is considered to be more viable to combine a $\mu\text{c-Si:H}$ cell with an a-Si:H cell, forming a tandem photovoltaic device. The $\mu\text{c-Si:H}$ cell is ca. 2 μm , and the a-Si:H cell is approximately 400 nm thick [32]. The different band gaps of these cells improve solar light harvesting and lead to increased efficiencies, the best stabilized efficiency being currently 12.3% [24].

In an attempt to decrease production costs related to crystalline Si while maintaining benefits of the latter, 'crystalline silicon on glass' (CSG) solar cells were developed. CSG is deposited by PECVD and subsequently annealed at ~ 600 °C to produce polycrystalline material with large grains, as illustrated in Figure 3.3C [27]. The best efficiency obtained with a CSG solar cell of thickness of 2 μm is 10.4% [32].

3.3. Organic solar cells

An organic solar cell is formed as a junction between donor and acceptor organic materials, the electronic levels of which are aligned in such a way that it provides charge separation. The principle of work of organic solar cells is discussed in Section 2.3.3 and illustrated in Figure 2.8. Various polymers are used as donors that absorb light and transfer excited electrons to the acceptor, which is often a fullerene molecule C_{60} [40]. The generated electrons and holes are supposed to be collected at separate contacts, the process driven by appropriate work functions of the electrodes.

The advantages of organic solar cells is their large absorption coefficient, low cost of production and possibility to fabricate cells on flexible substrates [2]. The drawbacks are low efficiencies and poor control/reproducibility of the fabrication process, especially when a complex bulk heterojunction is involved. Advanced chemistry and nanotechnology methods are being developed to improve control over the structures [41]. Another major issue is stability of organic solar cells, which are susceptible to fast oxidation and need tight encapsulations. Most organic solar cells investigated nowadays degrade within several hours to several months time [42]. The timescale of degradation depends sensitively on the presence and type of encapsulation. For cells that are not encapsulated, slightly different testing conditions often result in significantly different degradation kinetics, according to a recent very thorough study by Tanenbaum *et al.* [43]. Optimized and well encapsulated organic solar cells with the active layer of only 90 nm thick and efficiency of 2% demonstrated remarkable stability during >40 days of full sun illumination at 85° C [43].

The best achieved efficiencies reported are 10.7% for a single organic solar cell, and 8.2% for a submodule [24]. However, the stability of these champion solar cells was not investigated.

3.4. Dye sensitized solar cells and related concepts

The *dye-sensitized solar cell* (DSC, DSSC, or Grätzel cell) is a hybrid organic-inorganic device, employing organic dye molecules for light absorption, and an inorganic semiconductor to form a junction and to transport the charge carriers. Its structure is illustrated in Figure 3.4A. The semiconductor is usually a mesoporous titanium dioxide (TiO_2) thin film, with an average pore size of about 15 nm, and a film thickness of 5-20 μm [44]. The porosity is typically 50-60 % of the sample volume. An SEM image of such a film is shown in Figure 3.4B. While a TiO_2 nanoparticle film is the most common structure employed in DSCs, a variety of other materials and structures have been investigated as well [45]. A monolayer of dye molecules is attached to the internal surface of the TiO_2 film, the area of which is largely increased due to the high porosity of the TiO_2 film. The electronic structure of the dye is tailored so that it absorbs a broad part of the solar spectrum and its LUMO (lowest unoccupied molecular orbital) level lies slightly above the TiO_2 conduction band edge, so that injection of electrons from the excited dye to the TiO_2 can take place rapidly. When a dye molecule absorbs a photon, the excited electron can then be transferred to the TiO_2 conduction band. To complete the circuit, the dye must receive an electron to replace the lost one at the dye empty HOMO orbital. Since it is difficult to provide a direct contact between the dye molecules and the counter electrode, a liquid electrolyte is employed. The electrolyte is composed of ions of so-called redox (reduction-oxidation) couples, which can both accept and donate electrons, *i.e.*, be reduced and oxidized. This redox species donates an electron to the dye, and is subsequently reduced (picks up an electron) at the counter electrode.

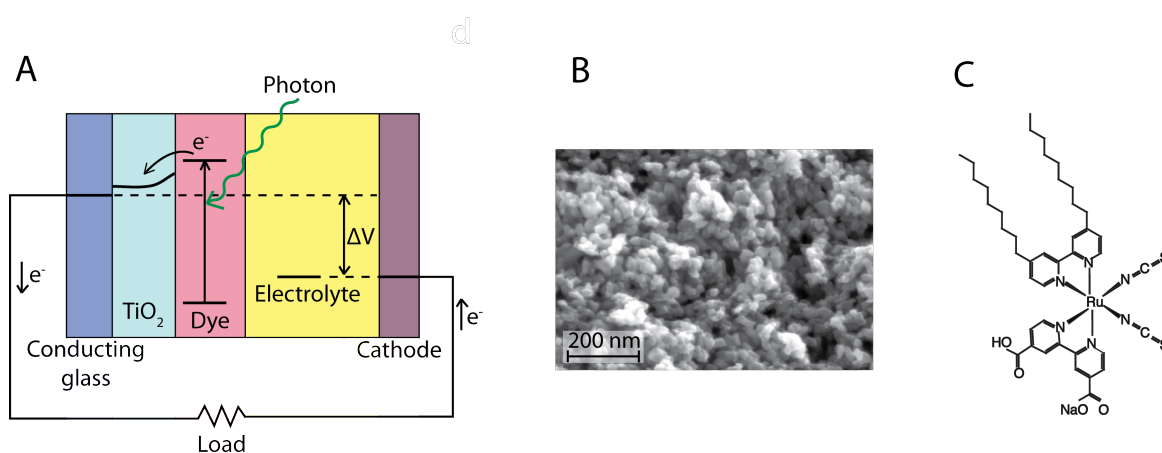


Figure 3.4. (A) Principle of work of dye-sensitized solar cells (redrawn from [44]). (B) SEM image of a porous TiO_2 film (courtesy of L.-P. Heiniger). (C) Chemical structure of dye Z907.

Different dyes can be used in a DSC, but the most efficient solar cells are based on ruthenium complexes [46]. A dye from this group is dye Z907, which is used in this work (Figure 3.4C). These dyes sustain up to 10^8 redox cycles, which corresponds to 20 years of operation in sunlight [44]. The reason for such outstanding photostability of an organic molecule is that the excited state of the dye is deactivated very rapidly through an electron transfer to TiO_2 . Thus other, much slower channels of excitation deactivation, e.g. generation of singlet oxygen, cannot compete with this process. The oxidized state of the dye is however not very stable, and regeneration of the dye by an electron transfer from the electrolyte should therefore also occur rapidly [44]. Stability tests performed on a dye solar cell show that a lifetime of at least 25 years is to be expected for the currently developed cells [47].

The best confirmed efficiency of a DSC is 11.9% [24]. Dye solar cells have also been fabricated on flexible plastic substrates with efficiencies of 7-9% [48], and even on paper with efficiency of 1.2% [49]. The energy payback time for a complete dye solar cell system with 8% efficiency installed in Southern Europe was recently estimated to be about 0.8 years [50]. For comparison, the corresponding payback time for multicrystalline silicon modules is 1.5 years [50].

There are several ways to further increase the efficiency of DSC. One is improving light absorption by dyes at 650-900 nm, where the light harvesting is usually poor [51]. Another way is to reduce the over-potentials, i.e., the difference in the position of the dye LUMO and the TiO_2 conduction band edge, and of the dye HOMO and the electron donating energy level of the electrolyte, which are needed for the corresponding electron transfer processes. Due to the presence of these over-potentials, the generated voltage is substantially lower than the band gap of the dye molecule (band gap value divided by the electron charge), usually by ca. 0.7 V [52] (this can be seen in Figure 3.4A). The largest contribution to this loss originates from the over-potential employed for regeneration of dye by the electrolyte [52]. If this loss is reduced to ca. 0.2 V and the sensitizing dye can absorb light up to 920 nm, the efficiencies can rise to 19%, according to estimations by Hardin *et al.* [52].

A concept closely related to DSC is that of *quantum-dot sensitized solar cells*, which have basically the same structure as DSCs, but with dye molecules replaced by quantum dots. A quantum dot is a nanoparticle of a semiconductor material (typically <10 nm in size) that has a higher band gap than the corresponding bulk material due to quantum confinement effects. Quantum dots are commonly made from Cadmium (CdS, CdSe, CdTe), Lead (PbS, PbSe), and Indium (InP). The properties of quantum dots that are beneficial for solar cells are tunability of the band gap achieved by varying the dot size, good photostability, and high light absorption coefficient. Among the Cd-based quantum dot sensitized solar cells, the highest achieved efficiency is 5.4% [53]. This is however significantly below the best efficiencies of DSCs.

A very recent and promising solar cell, which originated from the DSC concept, is a *perovskite-based cell* [54-58]. Perovskite is a crystal structure with a chemical formula ABX_3 , where X is a halogen or oxygen atom, and A and B are two different cations [58]. Some examples are CaTiO_3 , LaMnO_3 , and LaNiO_3 . Perovskite materials have been extensively studied as superconductors. The compounds used in the recent solar cells have methylammonium CH_3NH_3^+ and lead Pb^{2+} as the two cations, and I^- , Cl^- or Br^- as the anion [58]. Lee *et al.* [56] developed solar cells with a perovskite as the absorber, infiltrated into TiO_2 and Al_2O_3 mesoporous films, respectively. The Al_2O_3 based cells showed a better performance than the TiO_2 based devices (10.9% versus 8%). This is a very interesting and unexpected result, since Al_2O_3 is an insulator with a very large bandgap and only acted as a scaffold for the adsorbed perovskite. The perovskite thus functioned as both the absorber and the charge-transporting layer [56]. The highest demonstrated efficiency of a mesoporous perovskite-based solar cell is 15.0% [54]. Another very impressive result is a 15.4% efficient planar cell based on a flat layer of perovskite $\text{CH}_3\text{NH}_3\text{PbI}_{3-x}\text{Cl}_x$ forming a junction with a planar layer of a hole conducting polymer. The perovskite film for this champion cell was deposited by physical vapour deposition; the more conventional solution processing method yielded a solar cell with an efficiency of 8.6% [57]. All these results demonstrate a very impressive progress in a very short time.

4. Localized Surface Plasmon Resonance

This section describes the fundamentals of Localized Surface Plasmon Resonance (LSPR), which constitutes the central part of this work. It starts with a background on physics of optical constants, focusing on two basic models to describe optical properties of most crystalline solids: the Lorentz and the Drude oscillators. This theory is necessary for understanding the nanoparticle plasmon resonance, and it also provides background knowledge for methods of data modelling for the ellipsometry technique, described in Chapter 7.2.4. The physics of LSPR is covered in Section 4.2, and a brief overview of LSPR applications is given in Section 4.3.

4.1. Classical models of optical constants

4.1.1. Two types of optical constants

There are two types of optical constants, which are used interchangeably for description of optical properties: the *complex dielectric function* $\varepsilon = \varepsilon_1 + i\varepsilon_2$ and the *complex refractive index* $N = n + ik$ [59]. Generally, the complex dielectric function is more natural in microscopic descriptions of optical properties, since it is present in Maxwell's equations. However, the complex refractive index seems more intuitive for many people, because it can be directly related to *absorption* (through the absorption coefficient k) and *refraction* (via the real refractive index n) of light in matter. Therefore there is no general preference to one or the other optical constant type, and both will be used in this work. These two optical constant types are not independent, and their real and imaginary parts can be easily converted into one another through the following relations [59]:

$$\begin{aligned}\varepsilon_1 &= n^2 - k^2, \\ \varepsilon_2 &= 2nk, \\ n &= \sqrt{\frac{\sqrt{\varepsilon_1^2 + \varepsilon_2^2} + \varepsilon_1}{2}}, \\ k &= \sqrt{\frac{\sqrt{\varepsilon_1^2 + \varepsilon_2^2} - \varepsilon_1}{2}},\end{aligned}\tag{4.1}$$

assuming that the material is nonmagnetic ($\mu = \mu_0$).

4.1.2. The Lorentz model

The Lorentz model describes electrons in matter as oscillators ('springs'), which can respond to the driving electromagnetic field. The oscillators are assumed to be harmonic, isotropic, identical and independent. The displacement from equilibrium \mathbf{x} of an oscillator with mass m depends on (i) the driving force produced by the local electric field $\mathbf{E} = \mathbf{E}_0 e^{-i\omega t}$, (ii) a restoring force $K\mathbf{x}$, where K is the spring constant characterizing interactions between the electron and the positive ion core, and (iii) a dissipation force $b\dot{\mathbf{x}}$, where b is the damping constant. The corresponding equation of motion is therefore [59]

$$m\ddot{\mathbf{x}} + b\dot{\mathbf{x}} + K\mathbf{x} = e\mathbf{E}, \quad (4.2)$$

where we neglect magnetic forces, which are usually small compared to the electric ones. A steady-state solution to (4.2) suggests oscillation of the electron:

$$\mathbf{x} = \frac{e}{m(\omega_0^2 - \omega^2 - i\gamma\omega)} \mathbf{E}, \quad (4.3)$$

where $\omega_0^2 = K/m$ and $\gamma = b/m$. If $\gamma \neq 0$, the proportionality factor between \mathbf{x} and \mathbf{E} is complex and the oscillations of the electrons are not generally in phase with the driving field. The proportionality factor can be written in a general form $\mathbf{x} = (e\mathbf{E}/m)Ae^{i\theta}$, where [59]

$$A \sim \frac{1}{\sqrt{(\omega_0^2 - \omega^2)^2 + \gamma^2\omega^2}}, \quad (4.4)$$

$$\theta \sim \arctan \frac{\gamma\omega}{\omega_0^2 - \omega^2}.$$

The amplitude and phase are plotted as functions of frequency ω in Figure 4.1A. The amplitude has a maximum at about the resonant frequency ω_0 , and its lineshape is determined by γ . The height of the maximum is proportional to $1/\gamma$, and the width is proportional to γ . At low frequencies $\omega \ll \omega_0$ the displacement is in phase with the driving field ($\theta \cong 0$), while at high frequencies $\omega \gg \omega_0$ it is π out of phase [59]. The phase shift changes rapidly in the region around ω_0 .

The displaced electrons contribute to macroscopic polarization of the matter $\mathbf{P} = -n e \mathbf{x}$, where n is the number of oscillators per unit volume. Using (4.3) one gets

$$\mathbf{P} = \frac{\omega_p^2}{\omega_0^2 - \omega^2 - i\gamma\omega} \varepsilon_0 \mathbf{E}, \quad (4.5)$$

where ω_p is the plasma frequency defined as $\omega_p^2 = ne^2/m\varepsilon_0$. The plasma frequency has an explicit physical meaning for electrons in metals, and will therefore be

discussed in the next chapter. Here it can be considered just as a material-specific constant.

The complex dielectric function ε is used to relate the polarizability and the driving electric field according to $\mathbf{P} = (\varepsilon - 1)\varepsilon_0\mathbf{E}$, and after comparing this to (4.5) one readily gets the complex dielectric function of the system of identical harmonic oscillators:

$$\varepsilon = 1 + \frac{\omega_p^2}{\omega_0^2 - \omega^2 - i\gamma\omega}. \quad (4.6)$$

Its real and imaginary parts are:

$$\varepsilon_1 = 1 + \frac{\omega_p^2(\omega_0^2 - \omega^2)}{(\omega_0^2 - \omega^2)^2 + \gamma^2\omega^2},$$

$$\varepsilon_2 = \frac{\omega_p^2\gamma\omega}{(\omega_0^2 - \omega^2)^2 + \gamma^2\omega^2}. \quad (4.7)$$

ε_1 and ε_2 are plotted in Figure 4.1C. It can be shown that the maximum value of ε_2 is approximately $\omega_p^2/\gamma\omega_0$, and the width of the curve at the half maximum of ε_2 is γ [59].

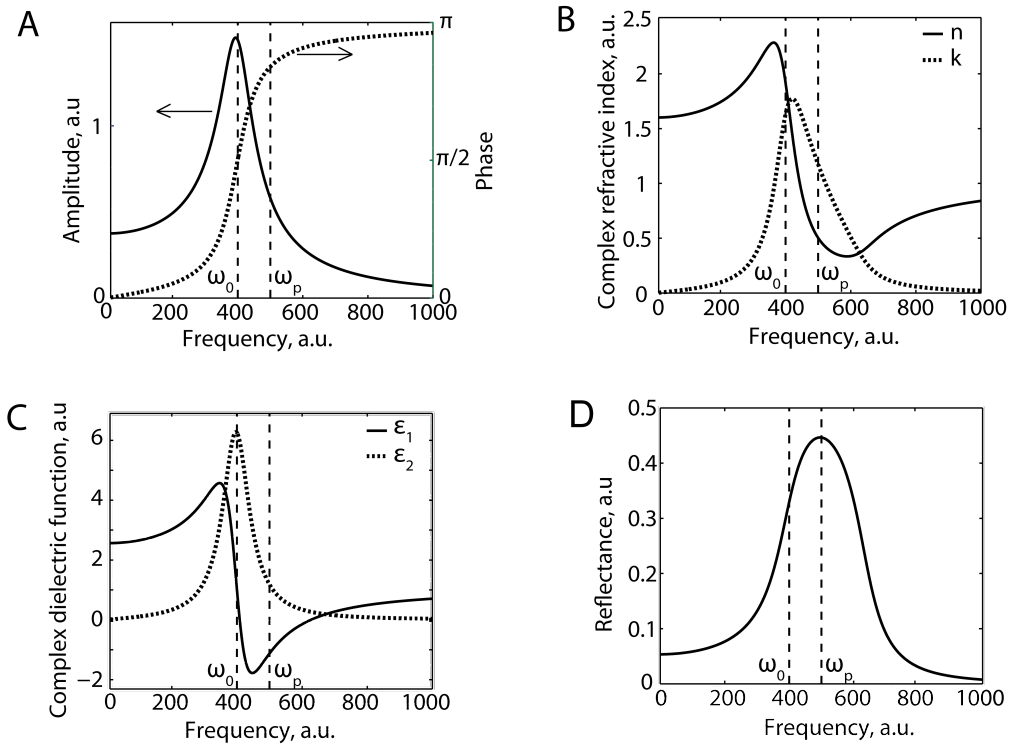


Figure 4.1. Results of the Lorentz oscillator model plotted as functions of frequency (arbitrary units): (A) amplitude and phase of a Lorentz oscillator, (B) complex refractive index, (C) complex dielectric function, (D) reflectance of a system of identical Lorentz oscillators. The dashed lines mark the resonance frequency ω_0 and the plasma frequency ω_p .

The real and imaginary parts of the complex refractive index are shown in Figure 4.1B, and the corresponding reflectance of the system is presented in Figure 4.1D. The absorption coefficient k has a maximum at about ω_0 , and the high values of k give rise to a maximum in the reflectance. At high frequencies, k goes to zero and n approaches its free-space value - the frequency is too high for the oscillator to be able to respond.

Despite its simplicity, the Lorentz oscillator model describes optical properties of many materials well, and in different spectral regions. Electronic, vibrational and permanent dipole response to electromagnetic radiation can often be accounted for using one or several Lorentz oscillators for each of the excitation types [59]. Oscillator types that are modifications of the Lorentz model were used in this work to model the optical properties of amorphous Si films in Papers 1 and 2, and of TiO₂ films in Paper 2. For metals, it is often more appropriate to use a special case of the Lorentz model - the Drude oscillator, which is described in the next section.

4.1.3. The Drude model

Metals have different optical properties compared to those of semiconductors and dielectrics (nonconductors) due to their electronic band structure, described in Section 2.3.1. In nonconductors, only photons with energy exceeding the band gap can be absorbed, and therefore they are transparent in the visible region. In metals, there is no band gap, and electrons can move to available higher energy states by absorbing low-energy photons, which makes metals highly absorbing and reflecting in the visible, infrared and microwave regions.

Since electrons in metals can be excited to higher energy states by low-energy photons and also by the thermal energy at room temperature, *i.e.*, they can pick up infinitely small amounts of energy, they can be approximated as ‘free’ electrons not bound to their ion cores. Their response to an electromagnetic field force can thus be modelled with a Lorentz oscillator without the restoring force (‘spring’). Substituting $\omega_0 = 0$ into (4.6), one gets the dielectric function of a system of free electrons [59]:

$$\varepsilon = 1 - \frac{\omega_p^2}{\omega^2 + i\gamma\omega} \quad (4.8)$$

with real and imaginary parts:

$$\begin{aligned} \varepsilon_1 &= 1 - \frac{\omega_p^2}{\omega^2 + \gamma^2}, \\ \varepsilon_2 &= \frac{\omega_p^2\gamma}{\omega(\omega^2 + \gamma^2)}. \end{aligned} \quad (4.9)$$

The plasma frequency is as before $\omega_p^2 = ne^2/m\varepsilon_0$, where n is the density of free electrons and m is the effective mass of an electron in the metal. If we neglect damping ($\gamma \ll \omega$), then it follows from (4.8) that $\varepsilon = 0$ at the plasma frequency. It can be shown that such an excitation corresponds to a longitudinal oscillation, which is the oscillation of the conduction electrons relative to the fixed ion cores in a metal. Such an oscillation is caused by an initial displacement of electrons from their equilibrium positions, and is sustained due to electrostatic forces between the electrons. The natural frequency of the free oscillation of the free electrons is the plasma frequency ω_p [60]. A quantum of this charge oscillation is called a (*volume or bulk*) *plasmon*. Since a volume plasmon is a longitudinal oscillation, it does not couple to transverse electromagnetic waves and can only be excited by charged particles impact (for example, by firing electrons into a metal). Most metals have ω_p in the ultraviolet region, typically at 4-15 eV [60].

The damping constant γ is related to the average time τ between collisions of electrons with impurities and lattice phonons as $\gamma = 1/\tau$. τ is on the order of 10^{-14} s at room temperature, corresponding to $\gamma = 100$ THz, which for most metals is much less than ω_p [59, 60]. With condition $\gamma \ll \omega_p$, (4.9) becomes:

$$\begin{aligned}\varepsilon_1 &\approx 1 - \frac{\omega_p^2}{\omega^2}, \\ \varepsilon_2 &\approx \frac{\gamma\omega_p^2}{\omega^3}.\end{aligned}\tag{4.10}$$

Values of the dielectric function in the low- and high-frequency limits can be estimated using (4.10). At high frequencies $\omega \gg \omega_p$, ε_1 is close to unity, and ε_2 approaches zero. The metal behaves as a dielectric in this region, and transmits most of the light. At frequencies $\omega \ll \gamma$ (which also means $\omega \ll \omega_p$), ε_1 is large and negative, and ε_2 is large and positive. Here, the absorptance is very high, which leads to a high reflectance. In the intermediate region $\gamma < \omega < \omega_p$, the reflectance is high as well.

The Drude model describes well the metal aluminium, the dielectric function of which is shown in Figure 4.2. The weak feature at approximately 1.5 eV is caused by interband transitions, which will be discussed below. Ignoring this feature, one can see that the low- and high-frequency behaviours follow well the ones of the Drude model described in the previous paragraph.

However, for many other metals the Drude model alone is not good enough to account for the optical properties. Metals like silver (Ag) and gold (Au) (which are both important in this work) show some free-electron behaviour, but also have a significant contribution from the more bound/localized electrons. The dielectric functions from experiments and calculations using the Drude model for Au and Ag are shown in Figure

4.2. It can be seen that the Drude model works well only up to a certain energy (ca. 2.5 eV for Au and 4 eV for Ag), and then large deviations occur. These deviations are caused by a response from the bound (lying deeper in energy than the free ones) electrons, when the energy of photons is enough to excite the electrons to empty higher bands. This mechanism is called *interband absorption*, and it naturally leads to an increase in ϵ_2 . The contribution from the bound electrons can be described with one or several Lorentz oscillators [59].

The interband transition threshold lies in the near ultraviolet (at ca. 4 eV) for Ag, so in the visible range Ag has a high reflectivity with little dependence on the wavelength of light, which explains its ‘white’ colour. On the other hand, for Au the interband transitions occur already at approximately 2.4 eV (≈ 520 nm), which means that only red and yellow light is reflected efficiently. This explains the ‘yellow’ colour of gold.

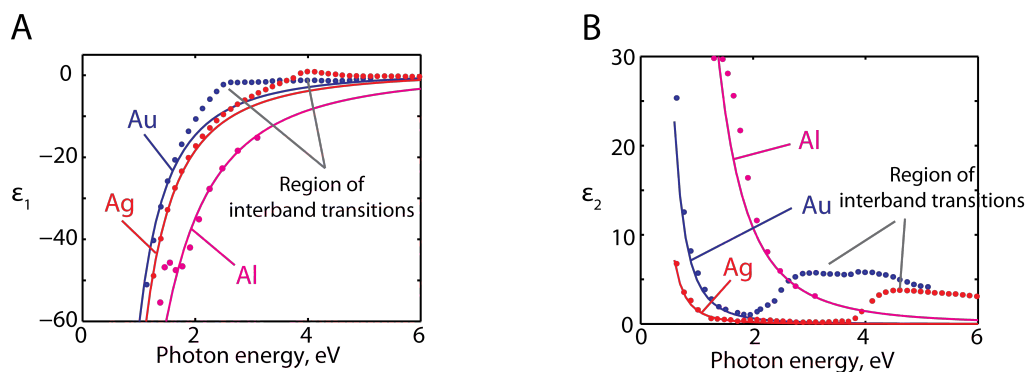


Figure 4.2. Optical properties of three metals important in plasmonic studies: aluminium, gold, and silver. (A) Real and (B) imaginary parts of the dielectric functions, measured (dots) and calculated with the Drude model (lines). For Au and Ag, presence of interband transitions in this spectral region causes substantial deviations from the free-electron behaviour. The measured data for Al was taken from Ordal *et al.* [61], and for Ag and Au from Johnson and Christy [62]. In the Drude model fit, the following parameters were used: Au: $\omega_p = 7.9$ eV, $\gamma = 0.08$ eV; Ag: $\omega_p = 8.8$ eV, $\gamma = 0.02$ eV; Al: $\omega_p = 12.5$ eV, $\gamma = 0.6$ eV.

4.2. Localized Surface Plasmons

4.2.1. Qualitative description

A *localized surface plasmon* is a collective oscillation of conduction electrons in a metal nanoparticle, which can be excited by light, often in or around the visible part of the spectrum. In contrast to the volume (or bulk) plasmons, discussed in Section 4.1.3, and surface plasmons, which are propagating charge oscillations at a metal-dielectric surface, the nanoparticle plasmons are *localized* excitations. They are confined within the volume of the particle, the dimensions of which are smaller than the wavelength of light. Since the localized plasmons do not carry momentum, they can be excited by photons, which possess zero momentum as well. At the resonance conditions, discussed in the next section, the electron cloud in the nanoparticle is believed to oscillate in phase with the incoming light, as schematically illustrated in Figure 4.3A. However, the electron cloud oscillating as a whole might be a wrong picture of the phenomenon. In particular, a time-dependent density functional theory treatment performed on a very small metal particle (containing 100 atoms) exposed to an electric field changing periodically in time, suggests a complex pattern of charge distribution [63]. At every moment, this pattern has a structure of multiple shells inside one another having alternating, more positive or more negative, charges [63]. For larger particles, the pattern approaches the more conventional picture of negative and positive charges induced on the surfaces of the particle.

This chapter covers the basic physics of the localized surface plasmon resonance, which is the core feature of this work. It starts with the quasi-static approximation, explaining the nature of the resonance, and continues with a discussion beyond the quasi-static treatment, which clarifies some of the plasmon resonance properties.

4.2.2. Metal particle in a quasi-static electric field

The quasi-static approximation assumes that the electric field of the incoming electromagnetic wave is constant over the particle volume, which allows simplifying the problem to a problem of a particle in an electrostatic field. This assumption is valid if the particle has a size $b \ll \lambda$, where λ is the wavelength of light in the surrounding medium. When the stationary special solutions are found, the harmonic time dependence of the incoming field can be added to them.

Let us consider a homogeneous metal sphere of radius b in a uniform, static electric field $\mathbf{E} = E_0 \hat{\mathbf{z}}$ (Figure 4.3B) [60]. The surrounding medium is non-absorbing and has a real dielectric constant ϵ_m , and the dielectric function of the sphere is $\epsilon(\omega)$. Calculations of the optical properties of metal nanoparticles using the bulk metal

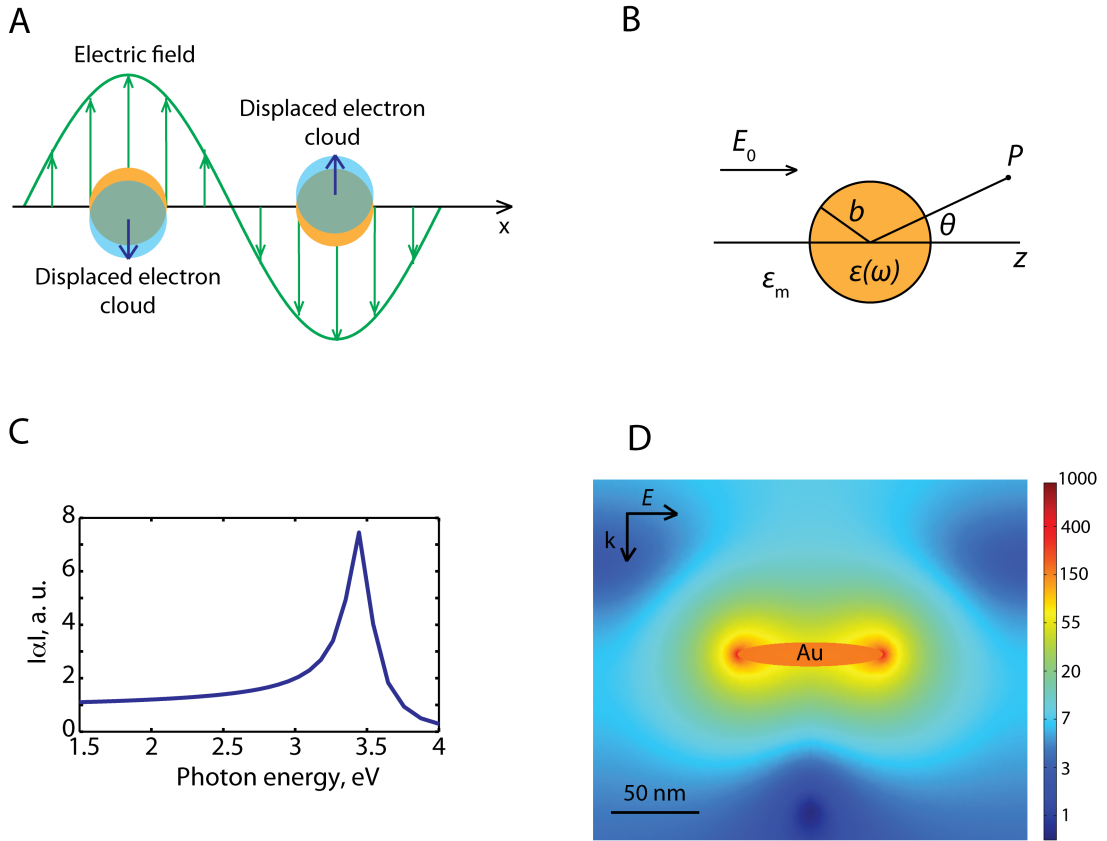


Figure 4.3. (A) Schematics of the displacement of the electron cloud driven by the electric field of a photon in a plasmonic nanoparticle (shown in yellow) at a resonance. (B) Schematics of a sphere in an electrostatic field. (C) The absolute value of the polarizability α of a small Ag sphere obtained in the electrostatic approximation, as a function of the energy of the incoming electromagnetic field. (D) Simulated electric field distribution around a prolate nanoparticle at a resonance. The Au nanoparticle (the axes are 84 nm and 14 nm) is surrounded by a medium with refractive index of 1.26, and the resonance is at 700 nm. The colour scale for the electric field represents the ratio of the intensity of the near-field to that of the incident field, $|E^2|/|E_0^2|$. Image courtesy of Carl Hägglund.

dielectric functions can reproduce the experimental results well, which justifies use of the bulk metal functions to describe plasmon resonance in nanostructures [64]. There is an estimation that it is the case for nanoparticles larger than about 3 nm [65]. To calculate the electric potentials inside and outside of the sphere, one has to solve the Laplace equation. The obtained electric potentials are [60]:

$$\Phi_{\text{in}} = -\frac{3\epsilon_m}{\epsilon(\omega) + 2\epsilon_m} E_0 r \cos \theta, \quad (4.11)$$

$$\Phi_{\text{out}} = -E_0 r \cos \theta + \frac{\mathbf{p} \cdot \mathbf{r}}{4\pi\epsilon_0\epsilon_m r^3},$$

$$\mathbf{p} = 4\pi\epsilon_0\epsilon_m b^3 \frac{\epsilon(\omega) - \epsilon_m}{\epsilon(\omega) + 2\epsilon_m} \mathbf{E}_0.$$

One can see that the applied field induces a dipole moment in the sphere, which can be also defined via $\mathbf{p} = \epsilon_0\epsilon_m\alpha\mathbf{E}_0$, where α is the *polarizability* of the sphere. Comparing this expression and \mathbf{p} from (4.11), one gets the polarizability of the small sphere in the electrostatic approximation:

$$\alpha = 4\pi b^3 \frac{\epsilon(\omega) - \epsilon_m}{\epsilon(\omega) + 2\epsilon_m}. \quad (4.12)$$

The absolute value of α as a function of frequency ω , calculated using $\epsilon(\omega)$ from a Drude model fit to experimentally obtained dielectric functions of silver, is shown in Figure 4.3C. The polarizability exhibits a resonance when

$$\text{Re}(\epsilon(\omega)) = -2\epsilon_m. \quad (4.13)$$

We have thus demonstrated that the polarizability of a small metal sphere in an electrostatic field is enhanced at particular energies (or frequencies ω) of the field, which is the essence of the *plasmon resonance*. For a sphere made from a Drude metal and located in vacuum, condition (4.13) is realized at $\omega_0 = \omega_p/\sqrt{3}$ (from (4.10)). The position of the resonance depends on the dielectric function of the surrounding medium, a fact that has given rise to numerous applications of metal nanostructures in biological and chemical sensing [66-68]. The plasmon position red-shifts with increasing ϵ_m , and qualitatively this can be understood as polarization of the dielectric by the field of the sphere. The polarization charges accumulated at the dielectric-sphere interface reduce the restoring force for the oscillating electrons in the sphere, which shifts the resonance position to lower energies [65]. The magnitude of α at the resonance is limited by the non-zero denominator, due to $\text{Im}(\epsilon(\omega)) \neq 0$ [60].

The electric field inside and outside of the sphere can be calculated from the potentials (4.11) to obtain [60]:

$$\mathbf{E}_{\text{in}} = \frac{3\epsilon_m}{\epsilon(\omega) + 2\epsilon_m} \mathbf{E}_0,$$

$$\mathbf{E}_{\text{out}} = \mathbf{E}_0 + \frac{3\mathbf{n}(\mathbf{n} \cdot \mathbf{p}) - \mathbf{p}}{4\pi\epsilon_0\epsilon_m} \frac{1}{r^3}, \quad (4.14)$$

where \mathbf{n} is the unit vector in the direction of point of interest P . The electric fields exhibit a resonant enhancement at the condition (4.13) as well. The field inside the sphere is uniform and enhanced compared to the incident field. The field at the sphere surface is even more enhanced (by *ca.* 10 times for a small Ag sphere [69]) and decays

rapidly away from the surface (as $1/r^3$, see (4.14)). An example of calculated electric field around a Au nanoparticle is shown in Figure 4.3D; the enhancement in the field intensity (the field amplitude squared) in this case is up to *ca.* 500 times. The enhanced near-field around a metal nanoparticle is used in many application, in particular, to promote light absorption in solar cell materials and for sensing purposes, which both are in focus in this thesis.

Since the incoming electromagnetic field is actually not static, but changing in time according to $\mathbf{E} = \mathbf{E}_0 e^{-i\omega t}$, one should add the time dependence to the obtained quasi-static solutions. The dipole then oscillates as $\mathbf{p}(t) = \varepsilon_0 \varepsilon_m \alpha \mathbf{E}_0 e^{-i\omega t}$, and therefore radiates electromagnetic waves, which corresponds to scattering of light by the sphere. It can be shown that within the near field region, the magnetic fields are much weaker than electric fields, and can therefore be neglected [60].

The *absorption* and *scattering cross sections* can be calculated according to [60]:

$$C_{\text{sca}} = \frac{k^4}{6\pi} |\alpha|^2 = \frac{8\pi}{3} k^4 b^6 \left| \frac{\varepsilon - \varepsilon_m}{\varepsilon + 2\varepsilon_m} \right|^2, \quad (4.15)$$

$$C_{\text{abs}} = k \text{Im}(\alpha) = 4\pi k b^3 \text{Im} \left(\frac{\varepsilon - \varepsilon_m}{\varepsilon + 2\varepsilon_m} \right),$$

where $k = 2\pi/\lambda$ is a wave number. Absorption scales as b^3 , and scattering as b^6 , and for particles with $b \ll \lambda$ absorption dominates over scattering. Both quantities exhibit a resonant enhancement at the plasmon dipole resonance energy.

Nanoparticles used in this work have shapes of discs and cylinders, which can be geometrically approximated as oblate spheroids. This is a subtype of a general *ellipsoid* shape, which can be solved analytically in the electrostatic approximation. For an ellipsoid with semiaxes $b_1 \leq b_2 \leq b_3$, specified by $\frac{x^2}{b_1^2} + \frac{y^2}{b_2^2} + \frac{z^2}{b_3^2}$, the polarizabilities α_i along the axes can be shown to equal [59]:

$$\alpha_i = 4\pi b_1 b_2 b_3 \frac{\varepsilon(\omega) - \varepsilon_m}{3\varepsilon_m + 3L_i(\varepsilon(\omega) - \varepsilon_m)}, \quad (4.16)$$

where L_i is a geometrical factor given by

$$L_i = \frac{b_1 b_2 b_3}{2} \int_0^\infty \frac{dq}{(b_i^2 + q) \sqrt{(b_1^2 + q)(b_2^2 + q)(b_3^2 + q)}}. \quad (4.17)$$

The sum of all geometrical factors is 1.

Spheroids is a special class of ellipsoids. For prolate spheroids, the two minor axes are equal ($b_1 = b_2$), and for oblate spheroids, the two major axes are the same ($b_2 = b_3$). An everyday example of a prolate spheroid is a rugby ball, and an example of an oblate spheroid is candy M&M's. It follows from (4.16) that a spheroidal metal nanoparticle has two plasmon resonances of different energies, which correspond to oscillations of electrons along the different axes. The resonance along the major axis can be significantly red-shifted compared to that of a sphere of the same volume, and its peak wavelength increases in a close to linear fashion as a function of the spheroid aspect ratio (b_1/b_2 for oblate spheroids) [65]. This effect is illustrated in Figure 4.4, which shows the spectral positions of plasmon resonances in Au nanodiscs of different diameters and with a constant height, both measured and calculated using the quasi-static approximation. The calculations reproduce the measured peak positions reasonably well (Figure 4.4A).

The electrostatic approximation is strictly valid only for very small particles with sizes $b \ll \lambda$; however, in practice it provides reasonably good results for particles of sizes up to 100 nm, interacting with visible or near-infrared light [60]. For larger particles, a full electrodynamics calculation (based for example on Mie scattering) is generally needed [60].

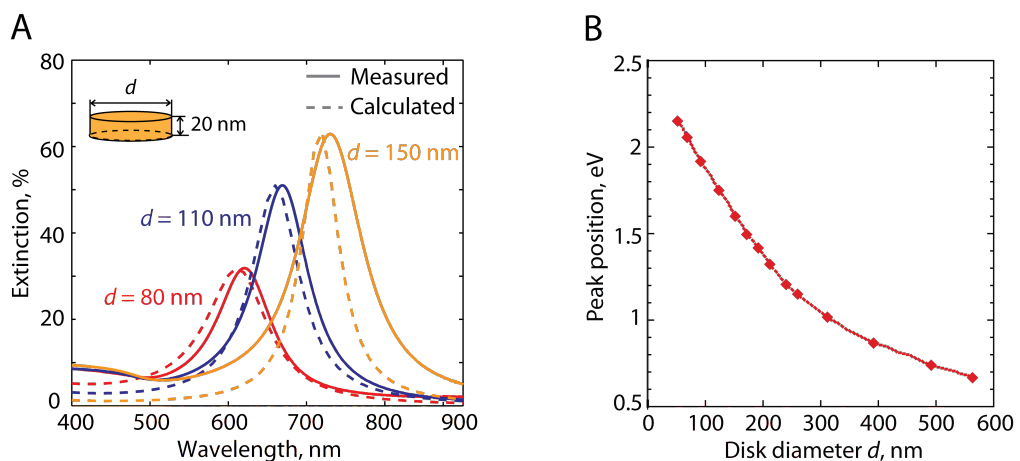


Figure 4.4. (A) Plasmon resonance of Au nanodiscs of different diameters and a constant height of 20 nm. The samples were measured in extinction (for details of measurements, see Section 7.2.2), and calculated using the electrostatic approximation. The calculated peaks are normalized so that the values of the maximal extinction are the same as those in the experiments. (B) Dependence of the resonance peak energy on the disc diameter for the same type of nanodiscs (adapted from [64]).

4.2.3. Beyond the electrostatic approximation

The Mie scattering is a rigorous electromagnetic treatment of scattering and absorption of a plane wave by a spherical particle. The resulting expressions are mathematically complex and difficult to understand intuitively, and thus we omit them here. The Mie scattering predicts appearance of peaks in absorption and scattering spectra, which are the result of resonances between the incident light and the electromagnetic modes of a sphere. These modes are oscillations that satisfy Maxwell's equations and the boundary conditions at the sphere surface [69]. The resonances exist not only in metal spheres, but also in other materials. Interestingly, the near-field enhancement is not specific to metal surfaces either. A Si sphere with the radius of 100 nm can have the same as or even larger near-field enhancement than a Ag sphere of the same radius [69]. The modes of a Si sphere are not related to the surface plasmon resonance; they are rather morphology-dependent resonances.

The Mie scattering predicts changing of the plasmon resonance energy with the particle size; the plasmon peak shifts to longer wavelengths as the size increases. Also, the relative contributions of scattering and absorption change with the size: scattering becomes dominant as the size increases [69]. It is also possible to calculate the near-field enhancement using the Mie treatment. The resonances in the near-field correlate well with the far-field effects (like measured absorption and scattering), although the peak positions are slightly different. Importantly, the near-field intensity increases with decreasing size of the sphere [69].

In the following, we go back to the intuitive electrostatic approximation and consider two particle size regimes where the electrostatic approximation no longer is an accurate and valid description of plasmonic excitations. These include large particles of sizes $b \sim \lambda$, and small particles of $b < 10$ nm. The analysis provided below reveals dependence of the plasmon resonance position and linewidth on the particle size [60].

For large ($b \sim \lambda$) nanoparticles, the electric field cannot anymore be considered constant over the particle volume. Thus different parts of the particle experience a different phase of the incoming light, and the interference of the induced polarization fields is not anymore entirely constructive [65]. The restoring force of the oscillation therefore weakens, and the plasmon resonance position red-shifts with increasing particle size; this is also known as *dynamic depolarization*. Moreover, as the particle size increases, spontaneous emission of radiation by the induced dipole becomes more probable [70]. It is possible to modify the electrostatic approximation by including corrections derived from an electrodynamic treatment, which account for the radiative damping and the dynamic depolarization effects. This treatment is known as the *modified long-wavelength approximation* (MLWA) [70], and it allows extending the

validity of the electrostatic approximation for nanoparticles that have sizes up to 10% of the wavelength of light.

The width of the plasmon resonance peak (for example, the *full width at half maximum value*, FWHM), which is inversely proportional to the lifetime of the plasmon oscillation, is generally larger in the experiments compared to the value predicted by the theory, in particular, by the electrostatic approximation. The broadening is a result of various damping processes (and in measurements on many particles, it is enhanced by variations in particle size, shape, arrangement etc; these latter contributions are usually referred to as heterogeneous broadening). The plasmon oscillation can be damped via the radiative and non-radiative decay routes, and due to scattering of oscillating electrons on the lattice vibrations and impurities, and at the particle surface [60]. The *radiation damping* is a decay of the plasmon oscillations into photons. This route becomes more important as the particle size increases, which is expected for the dipole radiation since its intensity is proportional to the dipole moment squared. The *non-radiative damping* is a transfer of the resonance energy to an electron-hole pair, which means absorption of energy, since the excess of energy created by excitation of an electron is in most cases released as a thermal energy (via a cascade of lower and lower energy electron-hole pair excitations) and is ‘lost’.

It can be shown that the linewidth of the plasmon resonance, which can be deduced from light extinction measurements (as those in Figure 4.4), is related to the time constant of the decay processes t as [60]:

$$\Gamma = \frac{2\hbar}{t}, \quad (4.18)$$

where t incorporates contributions from characteristic times of the radiative decay t_{rad} , non-radiative damping t_{abs} , and elastic collisions t_{coll} :

$$\frac{1}{t} = \frac{1}{t_{\text{rad}}} + \frac{1}{t_{\text{abs}}} + \frac{1}{t_{\text{coll}}}. \quad (4.19)$$

It can be shown that in general $1/t_{\text{coll}} \ll (1/t_{\text{rad}} + 1/t_{\text{abs}})$ [60]. For small Au and Ag nanoparticles, t is about 1-5 fs.

In case of very small nanoparticles ($b < 10$ nm), the width of plasmon resonances is substantially increased due to the fact that the particle size is smaller than the electron mean free path (usually 30-50 nm). This enhances scattering of oscillating electrons at the surface of the particle, and additionally, the electrons can tunnel into states of surface adsorbates, if such are present [60, 65].

4.3. Applications of nanoparticle plasmon resonance

4.3.1. Brief overview

The specific optical properties of plasmonic nanoparticles have led to development of various applications. This section gives a very brief overview of applications of plasmon nanostructures to obtain enhanced signals in a number of spectroscopic techniques and potential benefits of plasmonics in nanomedicine. Nanoplasmonic applications for sensing and solar cells, which are particularly relevant for this work, are discussed in more detail in Chapters 4.3.2, 4.3.3 and 6.

As was shown in section 4.2.1, the electric field around a plasmonic nanoparticle at the resonance is greatly enhanced compared to the driving field (the external field from the incoming light). This phenomenon is employed in several spectroscopic techniques, where the generated signal is proportional to the electric field, often in powers of 2 to 4. One example is *fluorescence*, which is commonly used for detection and studying of organic, in particular biological, molecules. Placing a fluorescent or fluorescently labelled molecule next to a plasmonic nanostructure substantially improves the efficiency of the optical excitation/de-excitation process leading to fluorescence, and thus also enhances the fluorescence intensity. Gaps in between two nanoparticles ('hot spots') provide especially strong local electric fields; fluorescent emission from a dye molecule in a hot spot has been shown to be enhanced by a factor of 1340 [71].

Similarly, plasmonic resonance can greatly enhance the signal in *Raman spectroscopy* and *Infrared spectroscopy*, which are techniques for studying molecular vibrational modes. Raman scattering intensity has a very strong dependence on the local electric field E in a form of E^4 . Therefore enhancements of up to 10^{12} should be possible to obtain using plasmonic nanostructures [71], and enhancement factors of 10^6 are routinely demonstrated [72]. The high sensitivity of plasmon enhanced Raman scattering makes detection of single molecules possible [73], and it has even enabled studying processes inside a living cell [72].

Plasmonic nanoparticles have also been studied for medical applications. *Imaging of living tissue* and *detection of diseases* often require optical markers such as fluorescent dyes or quantum dots. The dyes are however prone to photobleaching, and quantum dots are potentially or demonstrated toxic. Sometimes the optical marker can also affect the function of the molecules to be detected. Recently, plasmonic nanoparticles were proposed for so called *label free sensing*; they do not exhibit photobleaching and are relatively non-toxic [71] or can be provided with non-toxic shells. The relevant signal for detection can be either optical, caused by scattering of light by the particles, or thermal, caused by absorption of light in the

particles that leads to an increase in local temperature, which can be detected. Heating of small metallic particles upon the resonant absorption of light is also investigated for *treatment of diseases*. The idea is to selectively introduce plasmonic nanoparticles into tumour cells, and by illuminating them (at wavelengths where living tissue is rather transparent) increase the temperature, which can be lethal for the cells [71]. The latter approach can also be used to thermally release chemotherapeutic drugs attached to the plasmonic nanoparticle, and thereby obtain a local release function.

4.3.2. Sensing using nanoparticle plasmons

The characteristics of localized surface plasmon resonances (LSPR) are sensitive to the dielectric function of the environment surrounding the plasmonic nanostructure, which has given rise to various sensing applications. The plasmon resonance energy (or, alternatively, the plasmon peak wavelength) depends, to a first approximation, linearly on the dielectric function (or, alternatively, refractive index) of the surrounding medium. This is suggested by equation (4.13) and supported by numerous experiments [66]. The refractive index sensitivity of a particular nanoplasmonic structure can therefore be estimated as a peak shift in nm per refractive index unit. The precision that can be achieved in LSPR sensing depends also on the peak width, since narrower peaks allow determination of the peak shift more accurately. The refractive index sensitivity used to compare various plasmonic sensing structures is therefore usually normalized by the width of the plasmon resonance peak and quantified in a figure of merit (FOM) [66].

The enhanced electric field around a plasmonic nanostructure decays in most cases exponentially with distance, unless affected by interference effects, and this makes it possible to sense processes happening in very small local volumes close to the sensing nanoparticle. It is especially convenient for some biological sensing applications, where interactions between specific molecules with sizes of the order of 1 nm are of interest. In this case (detector or recognition) molecules of one type, e.g., antigens, can be attached to the plasmonic sensor, and when molecules of another type, e.g., antibodies, specifically bind to the first ones, this process will be sensed via a change in the LSPR resonance, e.g., a peak shift. Plasmon resonance properties are very sensitive to processes within several tens of nm around the particle; for example, layer-by-layer formation of self-assembled monolayers [66] and slight changes in molecular configuration upon absorption of light [74] were monitored using this technique.

As was discussed in Section 4.2.2, the properties of a nanoparticle plasmonic resonance depend strongly on the particle size and aspect ratio. Thus, the refractive

index sensitivity of LSPR correlates strongly with these parameters; generally the sensitivity is higher for larger particles and for larger aspect ratios. This can be at least partially explained by the red-shift (lowering in energy) of the plasmonic resonance for such particles. In the visible range, the real part of the dielectric function of most metals has a steeper dependence on energy for lower energies (see Figure 4.2 for Al, Ag and Au), which leads to a higher sensitivity of the LSPR in that range. Sometimes ‘intrinsic’ shape effects, arising from a specific distribution of the electric field around a particle, play an important role along with the plasmon energy position influence. This is the case for particles with sharp edges (‘nanopyramids’, ‘nanostars’, ‘nanocrescents’, etc.), which usually exhibit much larger refractive index sensitivities compared to particles of more rounded shapes [66].

Most of the LSPR sensing experiments so far have employed Au or Ag nanostructures. The advantage of Au is its chemical stability and resistance to oxidation. Ag has however more advantageous optical properties: a steeper dependence of the real part of the dielectric function on energy and smaller imaginary part, which means less absorption losses [66]. Several other metals have been also used, for example, Pd, Al, Cu, and Sn [68].

LSPR sensing is actively researched for biological applications, and is also applied for chemical sensing [66, 67]. A number of physical and chemical processes were investigated using LSPR, for example, formation of metal hydrides, phase transitions in metal nanoparticles, corrosion processes, and magnetic transitions [68]. A part of this work (Papers 3, 5 and 6) is devoted to application of an LSPR sensing technique to study surface adsorption and desorption processes, and also diffusion in a porous material, relevant for dye solar cells. This is done using the indirect nanoplasmonic sensing (INPS) technique, which is described in the next section.

4.3.3. Indirect nanoplasmonic sensing technique

The indirect nanoplasmonic sensing (INPS) platform is an extension of the general idea of nanoparticle plasmon sensing, described in Section 4.3. In the INPS, the sensing nanoparticles are coated by a dielectric spacer and are thus not in a direct contact with the sample to be studied. The technique was recently developed in our group and has been successfully applied to study kinetics of various chemical and material science processes [75, 76]. It is based on monitoring the position of the plasmon resonance of nanoparticles in a structure schematically depicted in Figure 5.1A [75]. The structure consists of plasmonic nanoparticles covered with a thin dielectric film, onto which the sample to be studied is placed. A change in the properties of the sample (size, shape, phase, chemical composition etc.) influences the dielectric environment around the plasmonic nanoparticles, which leads to a change in the plasmonic resonance properties (Figure 5.1B). The dielectric spacer layer can perform functions of

protecting the sensing particle and providing the desired surface chemistry for the specimen [75]. This makes the INPS technique more versatile than the traditional ‘direct’ plasmon sensing schemes employing bare nanoparticles [66, 67]. Any material (metals, polymers, dielectrics) and in any form (particles, films etc.) can be investigated as long as the material related phenomena to be studied lie within the sensing range of the LSPR excitation electromagnetic field. However, the presence of a spacer layer also somewhat decreases the sensitivity of the plasmon resonance to the changes occurring at the specimen site compared to the case of bare nanoparticles, but optimizing the spacer thickness and nanoparticle size allows achieving good signal-to-noise ratios even with INPS.

The Indirect Nanoplasmonic Sensing technique provided valuable insights into various processes at the nanoscale, for example, formation of metal hydrides in small particles that cannot be studied by the conventional LSPR sensing, sintering of catalyst materials, glass transitions in polymers [68] and lipid bilayer formation on silica [77]. In this thesis, the INPS platform was used to better understand adsorption, desorption and diffusion of dye molecules on flat and in mesoporous TiO_2 films (Papers 3, 5 and 6).

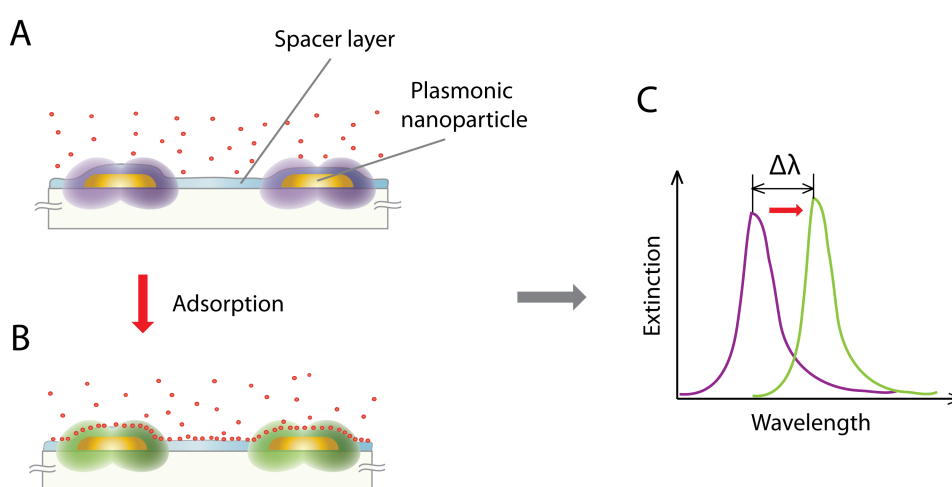


Figure 4.5. Schematics of the indirect nanoplasmonic sensing principle. An INPS sample (A) before and (B) after the monitored event (here adsorption of species onto the spacer layer) has taken place. (C) Shift of the plasmon resonance peak accompanying the adsorption.

5. Interactions of dye molecules with compact and porous TiO₂ films: adsorption, desorption and diffusion

Dye molecules adsorbed on a porous TiO₂ film is the main functional part of a dye-sensitized solar cell (DSC), as described in Section 3.4. In order to be able to fabricate well-performing and reproducible solar cells, the interactions between the dye molecules and the TiO₂ surfaces have to be understood and controlled in detail. Therefore, it is very important to understand the process of fabrication of the dye-TiO₂ system, which is commonly performed by adsorbing dye molecules from a solution onto a TiO₂ film. This section provides a background about the involved processes, namely adsorption, desorption and diffusion. Sections 5.1-5.3 describe the basics of adsorption processes on surfaces, mostly as viewed by the classical surface science that has studied adsorption of gases on surfaces for decades. The approaches used there are applicable to many adsorption-desorption processes, including those in the liquid phase, which are relevant for the dye-TiO₂ system. Section 5.4 addresses adsorption of dyes on TiO₂ as studied in relation to DSCs, and section 5.5 summarizes studies that relate the dye loading to the solar cell performance. Section 5.6 gives a brief insight into diffusion processes in porous materials and reviews studies related to impregnation of porous TiO₂ electrodes with dyes.

5.1. Basics of adsorption of molecules on solid surfaces

Adsorption is a process where molecules from a gas or liquid phase bind to a surface, forming a two-dimensional layer. The opposite process, where molecules leave a surface, is called *desorption*. In its purest form adsorption is strictly two-dimensional, and the formed adsorbate layer is a *monolayer*. There are, however, also deviations from the monolayer adsorption, where two or several layers of adsorbates can be formed on the surface. The latter process can be thought of as a condensation process; attractive interactions between the adsorbed species lead to formation of a dense film on top of the first monolayer. Generally, this happens when the attractive interactions between the adsorbate species are much larger than kT [78].

The interaction between the adsorbate and the surface (*adsorbent*) is usually classified as chemisorption or physisorption, depending on the strength of the interaction. The boundary between these two regimes is, however, not sharp. In the

case of *chemisorption*, a chemical bond is formed between the adsorbate and the surface, which leads to a significant change in the electronic structure of the adsorbed species and the surface close to the adsorbate. If an adsorbate is *physisorbed*, it is held by van der Waals forces instead and its electronic structure does not change substantially. Often, an adsorbate that can chemisorb on a particular surface goes through a physisorption state before forming a chemical bond. In terms of the bond strength, adsorbate bonds (for molecules consisting of a few atoms) below 0.1 eV are classified as physisorption, while bonds above 0.5 eV and up to the strongest bonds of 5-7 eV belong to the chemisorption regime. Adsorption may not only alter the electronic structure of the adsorbate, but also the properties of the surface, sometimes even to the extent that the surface reconstructs into a new arrangement of the atoms [78].

5.2. Kinetics of adsorption and desorption

When a molecule impinges on a surface, it is not certain that it will adsorb on it, even if adsorption is energetically favourable. There are several possible scenarios for a molecule colliding with a surface (Figure 5.1A-C). First, it can scatter back to the gas phase, either elastically or inelastically. *Elastic scattering* can be visualized as occurring to a ball bouncing off a hard surface without losing its kinetic energy, and in *inelastic scattering*, the surface is ‘softer’ and can deform, and upon collision, the molecule transfers a part of its energy to the surface. If the surface is deformable enough, the molecule may lose sufficient amount of its energy to stay on the surface. (Since the surface actually consists of atoms with bonds between them, ‘hard’, ‘soft’ and ‘deformable’ are actually determined by the mass ratio of the incident atom and the substrate atoms and by the stiffness (force constant) of bonds between the substrate

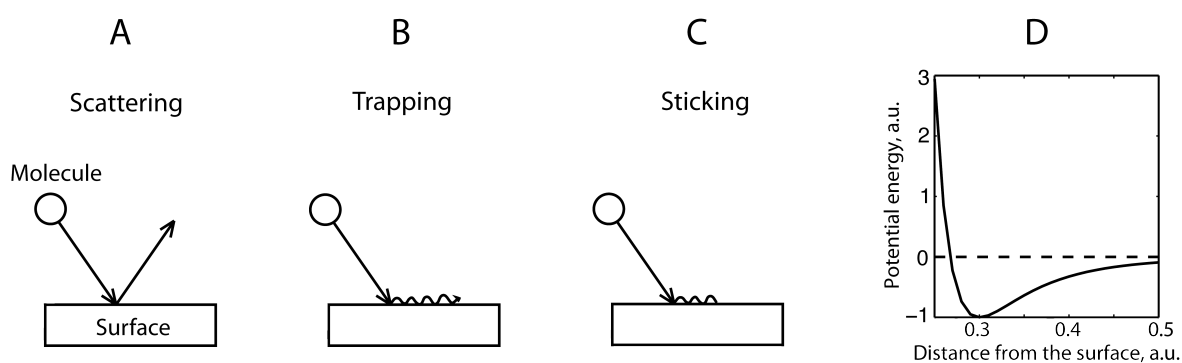


Figure 5.1. (A-C) Possible scenarios for a molecule colliding with a surface. (D) Schematics of a Lennard-Jones potential.

atoms.) When sufficiently large energy is lost in the collisions, the event is called *trapping* (Figure 5.1B) [78]. Although the molecule stays on the surface, it may be in a weakly bound state and thermal fluctuations (of the molecule and/or the surface atoms energy) can cause the molecule to desorb. A very special case of trapping is when only momentum transfer occurs so that the trapped adsorbate atom moves along the surface with maintained kinetic energy. Eventually, either energy dissipation occurs so that the atom is then more permanently bound to the surface, or momentum back-transfer occurs and the atom moves back to the gas phase. Temporary trapping has been demonstrated in experiments with molecular beams directed onto surface: one can detect a small number of molecules that spend a few hundred microseconds on the surface, but still do not adsorb [78]. If, however, the molecule converts into a more strongly bound state so that it stays on the surface for a reasonable time, the molecule is said to *stick*.

Trapping rates are determined by the efficiency of the energy (momentum) transfer between the molecule and the surface, while sticking rates depend on how fast the molecule finds a site where it can adsorb. Depending on the properties of the adsorbate and the surface, it can be either trapping or sticking that introduce the rate-limiting step for the adsorption process. Trapping and sticking rates respond differently to changes in the gas temperature (*i.e.*, the kinetic energy of the molecules). Trapping decreases with increasing temperature, since more energy has to be removed from the impinging molecules. In contrast, sticking is either unaffected by the gas temperature or may even intensify upon a temperature increase, in case there is an *activation barrier* for sticking [78].

To account for *trapping* rates, one should consider rates of kinetic energy transfer between the impinging molecules and the substrate. In a simple treatment, the gas molecules and the surface atoms may be regarded as hard spheres, and then the energy transfer will only depend on the masses of the adsorbate and adsorbent (surface) molecules. In a next step, one can add a slowly varying attraction potential (as a result of interaction of the surface and the approaching molecules). The details of such treatments can be found in the book by R. Masel [78]. The surface-molecule interaction potential is commonly, at a simple level, represented by the Lennard-Jones potential (Figure 5.1D). A molecule is trapped if it enters a shallow region of the attractive potential (at about, say, 0.45 on the x-axis in Figure 5.1D). Such a state is sometimes called an *intrinsic precursor state*. From there, the molecule can leave the surface (desorb) or move into the deeper well of the potential (about 0.3 on the x-axis in Figure 5.1D). Trapping rates often increase in presence of already adsorbed molecules, since the energy transfer to an adsorbate is usually much more efficient than the energy transfer to the surface, and in addition such collisions can mediate momentum transfer. Moreover, for some systems, an incoming molecule can be trapped on top of the already adsorbed layer and move along it until it finds a free site on the substrate. Such a trapped state is called an *extrinsic precursor state*.

Sticking is usually discussed in terms of *sticking probability* $S(\theta)$, which is a function of the coverage θ (the coverage is the ratio of the number of filled sites to the number of all sites). $S(\theta)$ is defined as the ratio of the number of molecules that stick, to the number of molecules that impinge on the surface. The rate of adsorption r_{ad} is then

$$r_{\text{ad}} = S(\theta)I, \quad (5.1)$$

where I is the flux of incoming molecules, expressed in molecules per unit area.

A useful quantity is the *initial sticking probability* $S(0)$, which is the sticking probability in the limit of zero coverage. The reported values vary from 10^{-7} to 1; however, if $S(0)$ are less than about 0.001 the gas is sometimes said not to stick [78]. Initial sticking probabilities depend on the type of gas and the surface, and on the temperature.

The dependence of the sticking probability $S(\theta)$ on coverage may reveal the important parameters in the adsorption process. In the simplest case, $S(\theta)$ decreases as the coverage increases, since there are fewer sites to bind to. Langmuir showed that if the adsorbate only needs one site to adsorb, and there are no adsorbate-adsorbate interactions and weakly bound states, then the decrease of $S(\theta)$ with coverage is linear (1st order adsorption). This behaviour has been observed, but there are many deviations from strictly linear dependence; a common case is a decrease in a non-linear fashion. The latter arises for dissociative adsorption, when every adsorbing molecule needs two or more adjacent nearest neighbor sites, and also in case of strong adsorbate-adsorbate interactions. Adsorbate-adsorbate interactions may also cause *increase* in the sticking probability with increase in the coverage, in case the adsorption process is dominated by trapping. This is because, as mentioned above, the energy transfer is more efficient for the adsorbate-adsorbate system compared to the adsorbate-surface system. Another situation where the sticking probability can increase with the coverage is when the system shows a surface reconstruction that is favorable for further adsorption.

In his works during 1913-1918, Irving Langmuir studied adsorption and desorption processes and formulated a number of simple models, which have proven to be very useful. In particular, he considered variation of the sticking probability with the coverage. When a molecule impinges on a surface and encounters an empty state, it will stick with probability $S(0)$. Langmuir assumed that if the molecule hits a site that is already occupied, it will scatter back to the gas phase. The sticking probability is then proportional to the fraction of empty sites $(1 - \theta)$:

$$S(\theta) = S(0)(1 - \theta)^n, \quad (5.2)$$

where n is the number of sites needed to hold the molecule. The rate of adsorption (5.1) is then:

$$r_{\text{ad}} = S(0)(1 - \theta)^n I. \quad (5.3)$$

If $n = 1$, then $S(\theta)$ linearly decreases with the coverage (this is sometimes called the 1st order Langmuir adsorption). However, in many cases the situation is more complex: for example, if a molecule that hits an occupied site does not desorb, but diffuses across the surface instead and finds a free site to adsorb. The latter weakly bound state is called a mobile precursor, and the process is called *precursor mediated adsorption*.

An adsorbed molecule will not stay at the surface forever. At non-zero temperatures, thermal excitations of vibrational modes may provide enough energy to break the adsorbate-surface bond, so that the molecule leaves the surface (*desorbs*). Normally the vibrational modes have energies much lower than chemical bonds, but since the process is probabilistic, some desorption *will* happen provided that one waits long enough. However, when the time needed for this exceeds reasonable values, adsorption may be considered as irreversible.

5.3. Adsorption isotherms

5.3.1. Basic overview

Adsorption isotherms serve to quantify the amount of adsorbent on a surface, at different temperatures, as a function of the concentration in the bulk phase outside the surface (*i.e.*, in gas or liquid). They are constructed for conditions with a constant temperature, hence the name. Adsorption isotherms describe the situation at *equilibrium*, where the adsorption is reversible and the molecules in the bulk phase are in equilibrium with the ones adsorbed on the surface. Since adsorption has been intensively studied for molecules in the gas phase, the amount in the bulk phase is classically quantified via the gas pressure. For adsorption from the liquid phase, the corresponding variable is the concentration of molecules in the liquid.

In 1945, Brunauer proposed a general classification of adsorption isotherms observed for gas-solid surface systems. The five schematic isotherm types are shown in Figure 5.2 [78]. Type I corresponds to a monolayer adsorption, and that is why it saturates at higher pressures. Type II shows no saturation at high pressures, which indicates formation of multilayers. Type III behaviour occurs more rarely than Type I and II, and it reflects strong interaction between the adsorbed species. For this type, at low pressures there is little adsorption, but when the pressure increases, the adsorption accelerates because of adsorbate-adsorbate interactions. An example of this type is adsorption of ammonia on graphite. Type IV and V are specific for multilayer adsorption in porous materials; initially the adsorption behaviour is as the

ones for Type II and III, but at some higher pressures the pores get filled and the coverage saturates [78]. Since in the present work we only encounter Type I, *i.e.*, monolayer formation, we will not address or use the other types further.

5.3.2. Langmuir adsorption model

One of the simplest and most useful models for adsorption isotherms has been proposed by Langmuir. He considered adsorption of gas molecules onto an idealized surface, which has a number of sites available for adsorption. In the Langmuir model, (1) all the sites are equivalent, (2) each site can hold one molecule at most, and (3) there are no interactions between adsorbed molecules [78]. Then the rate of adsorption is proportional to the fraction of empty sites ($1 - \theta$), where θ is the fraction of filled sites, and the gas pressure p :

$$r_{ad} = k_{ad}p(1 - \theta). \quad (5.4)$$

This is equivalent to equation (5.3) with $n = 1$, since the flux is proportional to the gas pressure. The rate constant for adsorption k_{ad} is then proportional to the initial sticking probability $S(0)$. The rate of desorption is proportional to the number of filled sites θ (from where desorption may occur):

$$r_d = k_d\theta. \quad (5.5)$$

At equilibrium, the rates of adsorption and desorption are equal, which leads to:

$$\theta = \frac{k_{ad}p}{k_d + k_{ad}p}. \quad (5.6)$$

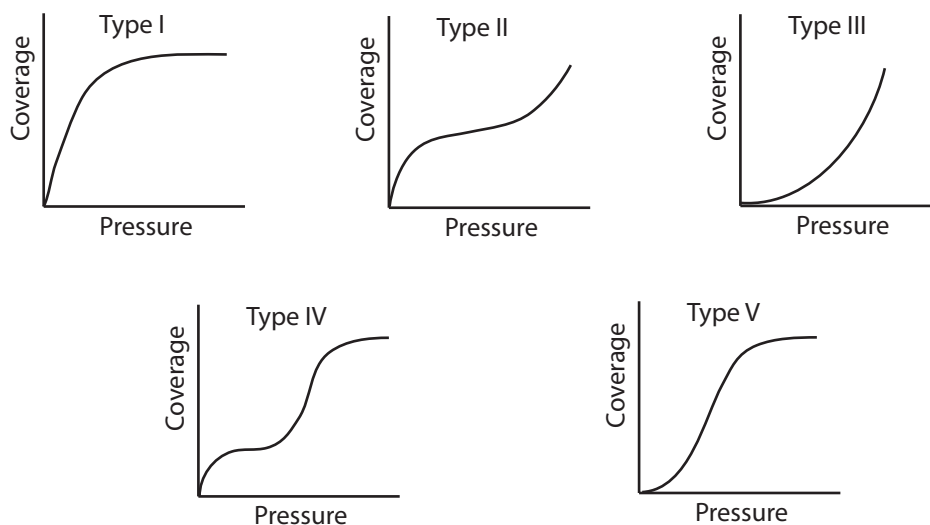


Figure 5.2. Generic types of adsorption isotherms (redrawn from [78]).

After defining an *equilibrium adsorption constant* K_{eq} as $K_{\text{eq}} = k_{\text{ad}}/k_{\text{d}}$, (5.6) is commonly rewritten as:

$$\theta = \frac{K_{\text{eq}}p}{1 + K_{\text{eq}}p}. \quad (5.7)$$

(5.7) is the equation of the *Langmuir adsorption isotherm* for non-competitive, non-dissociative adsorption. The typical behaviour is shown in Figure 5.2 as Type I, and in Figure 5.3. At low pressures so that $K_{\text{eq}}p \ll 1$, the coverage is proportional to the gas pressure. At high pressures, the coverage saturates.

The coverage θ is the ratio of the number of occupied sites N to the maximum number of states N_{max} , and so the Langmuir equation (5.7) can be written as:

$$\frac{N}{N_{\text{max}}} = \frac{K_{\text{eq}}p}{1 + K_{\text{eq}}p}. \quad (5.8)$$

Equation (5.8) can be re-written in the following way:

$$\frac{1}{N} = \frac{1}{N_{\text{max}}} + \frac{1}{N_{\text{max}}K_{\text{eq}}p}. \quad (5.9)$$

Plotting $1/N$ versus $1/p$ yields a straight line, which intercepts the y-axis at $1/N_{\text{max}}$, and has a slope of $1/N_{\text{max}}K_{\text{eq}}$.

In case there are several species *competing for adsorption*, then the equilibrium coverage of species i is [78]:

$$\theta_i = \frac{K_{\text{eq}}^i p_i}{1 + \sum_j K_{\text{eq}}^j p_j}. \quad (5.10)$$

While the Langmuir isotherm describes adsorption in many systems well, numerous cases deviate from this simplest behaviour. The deviations occur in case there are different binding sites and/or binding modes possible for the molecules, and also if adsorbed species interact with each other. Attempts to account for these deviations are described in the next chapter.

5.3.3. Other adsorption models

Freundlich proposed an empirical model to account for *multiple adsorption sites*:

$$\theta = \alpha_{\text{F}} P^{C_{\text{F}}}, \quad (5.11)$$

where α_F and C_F are fitting parameters. This equation usually only fits data over limited pressure ranges and it has little predictive value. It is therefore used quite rarely, mostly for rough inhomogeneous surfaces [78].

For single crystals, it has been more useful to assume a number of sites, where adsorption for each type of sites follows the Langmuir isotherm. According to this *multisite model*, the coverage is then a sum over coverages of the individual types of sites:

$$\theta = \sum_i \frac{\chi_i K_{eq}^i p}{1 + K_{eq}^i p}. \quad (5.12)$$

It turns out that χ_i and K_{eq}^i can be measured from adsorption-desorption data.

Another complication of the adsorption process is presence of *interactions* between the adsorbed molecules, in surface science usually referred to as adsorbate-adsorbate interactions. Adsorbed atoms or molecules can interact directly (usually relevant for neighbouring molecules) or via the surface. In the latter case, an adsorbed molecule changes the electronic properties of the surface, which in turn affects adsorption of other molecules on neighbouring sites. In direct adsorbate-adsorbate interaction, the electronic orbitals or the dipole fields of the adsorbate molecules interact. The Temkin isotherm addresses the *indirect adsorbate interactions*. Temkin assumed that indirect interactions lead to a change (usually lowering) of the heat of adsorption ΔH_{ad} that varies linearly with the coverage [78]:

$$\Delta H_{ad} = \Delta H_{ad}^0 (1 - \alpha_T \theta), \quad (5.13)$$

where ΔH_{ad}^0 is the heat of adsorption at $\theta = 0$ and α_T is a constant. Temkin then assumed that the Langmuir isotherm was still valid in case of indirect interactions, but with the equilibrium constant that varies with coverage [78]:

$$K_{eq} = K_{eq}^0 \exp\left(-\frac{\Delta H_{ad}^0 \alpha_T \theta}{kT}\right). \quad (5.14)$$

The Langmuir adsorption isotherm (5.7) can be written in the following way:

$$K_{eq} p = \frac{\theta}{1 - \theta}. \quad (5.15)$$

Substituting K_{eq} from (5.14) into (5.15), one gets:

$$\ln(K_{eq}^0 p) = \frac{\Delta H_{ad}^0 \alpha_T \theta}{kT} + \ln\left(\frac{\theta}{1 - \theta}\right). \quad (5.16)$$

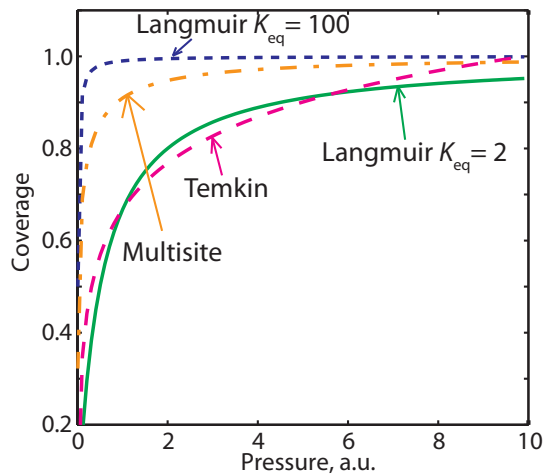


Figure 5.3. A plot of some typical isotherms calculated from equations (5.7), (5.12) and (5.17). The value of K_{eq} in the Langmuir and Temkin models was taken as 100; the multisite model assumed 3 types of sites with values of K_{eq} of 100, 10 and 2.

Temkin did most of his work at coverages θ of about 0.5, where the second term on the right hand side of (5.16) is negligible. Thus, the coverage becomes proportional to the logarithm of the pressure:

$$\theta = \frac{kT}{\Delta H_{ad}^0 \alpha_T} \ln(K_{eq}^0 p). \quad (5.17)$$

(5.17) is the expression of the *Temkin adsorption isotherm* [78]. An example of it is plotted in Figure 5.3.

Equation (5.17) is sometimes also called the *Fowler adsorption isotherm* [78], since Fowler derived it considering *direct interactions* between the adsorbed molecules and using a mean-field approximation to account for them (which is mathematically the same as the Temkin's approach).

5.4. Studies of adsorption and desorption of dye molecules on TiO_2 surfaces

As described in Section 3.4, at the heart of a dye (-sensitized) solar cell (DSC) is the system of dye molecules chemisorbed on the surfaces of a mesoporous TiO_2 film (typically *ca.* 10 μm thick). The film is composed of a network of interconnected TiO_2 nanoparticles, typically 20-30 nm large and with a porosity (relative pore volume) of

the film in the range of 50-60%. In an optimized cell, the dye molecules form a dense monolayer on the TiO₂ surface. The good 'quality' of this monolayer is crucial for the dye solar cell function; 'quality' is related to the overall efficiency, but also to stability etc. On the one hand, it is desirable to absorb as much of the solar light as possible, and thus the number of dye molecules should be maximized. On the other hand, the dyes should not adsorb in multilayers, since electron transfer from the dye to the TiO₂ can normally occur only from the dye molecules that form a chemical bond to the TiO₂, while the rest of the molecules would absorb light without any useful effect (recombination resulting in generation of heat). Moreover, a dense dye monolayer is believed to hinder the undesired recombination of charges, injected into TiO₂, with molecules in the electrolyte, although this is debated in some works (for a discussion on this topic, see [79]).

Adsorption of various dyes onto TiO₂ has been extensively studied [80-91]. A TiO₂ surface is usually immersed in a solution of dye molecules, and the molecules diffuse to and adsorb on the surface. The dyes used in DSCs have functional groups that can form a chemical bond with a TiO₂ surface (commonly carboxylate COOH or phosphonate PO(OH)₂ anchoring groups), and the molecules are known to chemisorb. The studied TiO₂ surfaces have included mesoporous films of the kind used in actual solar cells [81-83, 85, 87, 92], and also model systems: single crystals of TiO₂ [80, 86, 92] and thin compact TiO₂ films [84]. The amount of adsorbed dye as a function of the dye concentration in the solution is commonly fitted with the Langmuir adsorption isotherm [82, 83, 85, 86, 92]. (Although in this case, the adsorption occurs from a liquid phase, the Langmuir approach should be valid in principle.) The estimated values of the Langmuir equilibrium adsorption constant K_{eq} vary with the type of the dye and the TiO₂ surface; Lu *et al.* [86] report values in the range 10^5 - 10^6 M⁻¹ for single crystal surfaces, and Fattori *et al.* [82] and Fillinger *et al.* [83] found 4×10^4 M⁻¹ and 3×10^4 M⁻¹, respectively, for mesoporous anatase films.

However, some authors [83, 86] point out that some of the assumptions of the Langmuir model do not hold for the dye-TiO₂ system; the most obvious possible reasons for deviations are the assumptions of equivalent binding sites and no adsorbate-adsorbate interaction. A third possibility, when one deals with rather large adsorbate molecules, is slow re-arrangements among molecules in the adsorbate layer. Fillinger and Parkinson [83] compared impregnation of TiO₂ films using N3 dye solutions of various concentrations and during various times, but kept the final dye loading similar for all samples. They observed larger desorption of dye from samples prepared from a solution of a higher concentration (and during a shorter time). The authors therefore proposed that adsorption happens via a two-step process: a less strongly bound state converts to a strongly bound state. In their interpretation, at higher coverage the dye molecules bind with one carboxylate group (a less strong binding), while at lower coverages they attach with two carboxylate groups, which provides the strong binding [83]. Lu *et al.* [86] arrived to similar conclusions in their

study of the same dye (N3) on single crystals of rutile and anatase. Bazzan *et al.* [81] performed a series of adsorption-desorption processes for fabrication of a DSC, and discovered that such treatment leads to a higher dye loading and higher solar cell efficiencies, which also supports the hypothesis of the weakly and strongly bound states for dyes on TiO₂. Neale *et al.* [87] also found indications of the latter. The results in Papers 3, 4, and 6 of this thesis, where we observed variations in the amount of desorbed dye depending on the adsorption conditions, are consistent with such a picture.

Dye adsorption and desorption are commonly studied by optical absorption spectroscopy, where the amount of light absorbed by a sample is converted into the concentration of dye molecules, according to the Beer-Lambert law (see section 7.2.2 for the basics of the technique). A common routine is to impregnate a mesoporous TiO₂ film with dye, then desorb the dye (usually with a strong base) and measure the concentration of dye in the solution into which the dye molecules have been desorbed. Alternatively, the concentration of the impregnation solution is followed as it becomes depleted because of dye molecules adsorbing in the TiO₂ film. Sometimes, the absorption of dye directly on TiO₂ samples is followed, but this approach may lead to errors in concentration estimation, since TiO₂ films often scatter light efficiently and therefore the absorption of dye does not necessarily scale linearly with its concentration in the mesoporous structure. The mechanism of this is that due to scattering, the light path in the film increases and the dye molecules have more ‘chance’ to absorb the light, compared to the case when the rays traverse the film just once.

Alternative techniques used to study adsorption of dye molecules onto TiO₂ are electrochemical measurements [82], attenuated total reflectance and waveguide measurements [93, 94], and quartz crystal microbalance (Paper 4 in this thesis). Similarly to the optical absorption spectroscopy, these techniques only provide information about the total amount of dye in a mesoporous film, although the optical waveguide measurements could be used to map concentration profiles inside the film. In Paper 3 and 5 of this thesis, we demonstrate and develop a technique (Hidden Interface – Indirect Nanoplasmonic Sensing, HI-INPS) for following dye adsorption and desorption locally inside a mesoporous film, specifically in the present case at ‘the bottom’ (or the inner interface) of mesoporous TiO₂ samples.

Details of the dye-surface bond and orientation of dye molecules on a TiO₂ surface are another important aspects, which have been addressed by computer simulations [80, 89], X-ray reflectometry [84] and Scanning Tunnelling Microscopy (STM) [91]. A recent X-ray reflectometry study on two different dyes suggested that they bind to the TiO₂ in a monolayer fashion. The study also estimated the angle of the tilt of the molecule axes. Since most dye molecules employed in DSC have more than one binding group (for example, a classical dye N3 has four COOH groups, and dye Z907

studied in this thesis has two such groups), a number of binding ‘modes’ are hypothetically possible for each dye and TiO₂ surface. DFT calculations performed by Martsinovich *et al.* [80] suggest that the N3 dye on a rutile (110) surface may be adsorbed in 11 possible configurations with similar adsorption energies. The authors point out that the most likely binding modes are those implemented via 2 or 3 COOH anchoring groups. This consideration together with calculated electron injection times (which is the time to transfer electron from an excited dye molecule to the TiO₂) suggest 8 almost equally efficient configurations. This is an interesting result and it suggests that the adsorption geometry is not so crucial for this dye. However, if one takes into account also the effects of the electrolyte that normally surrounds the dye-TiO₂ system in actual solar cells, the conclusions may be modified, since the calculations were performed for the dye-TiO₂ system in vacuum, and did not consider any recombination with the electrolyte.

A few experimental studies have concluded that the performance of dyes adsorbed on TiO₂ is more sensitive to details of adsorption than the results from paper [80] suggest. Lu *et al.* [86] fabricated solar cells using dye N3 adsorbed on TiO₂ rutile and anatase single crystals with different faces exposed, and discovered that the cell efficiency varied significantly for the different crystal types and faces. This indicates that under actual solar cell conditions, there are a number of factors that determine the details of dye adsorption, which affect the cell performance. A recent STM study [91] suggested that absorption of light by a dye molecule might also lead to geometrical rearrangements of the molecules.

5.5. Dye loading of mesoporous TiO₂ photoelectrodes for Dye solar cells

In the process of a dye solar cell fabrication, the most common method to impregnate a TiO₂ film with dye is by soaking the film in a dye solution for about 12 h, with little (real time) control over the adsorption process. The impregnation process generally needs optimization in order to be able to reproducibly form an optimal dye monolayer, and also to make the DSC fabrication process compatible with industrial demands (where short impregnation times are desirable).

The time to fully impregnate a mesoporous TiO₂ film with dye depends on the impregnation conditions, such as the temperature [85, 95], the dye solution concentration [79, 85, 95, 96], type of the dye and the solvent [95, 96], and properties of the TiO₂ surface [97-99]. Longer impregnation times generally lead to an increase in the amount of adsorbed dye [85, 96, 100-102], although if the concentration of the dye

solution is low, the dye might not diffuse all the way to the bottom of the TiO₂ film even for long (> 12 h) impregnation times [79]. While a common procedure is to soak the film in a dye solution during 10-12 hours, a number of studies showed that it is possible to decrease this time to only several minutes by using higher temperatures [95], concentrated dye solutions [95, 103], and/or injecting the solution at high flow rates [103]. However, using high flow rates seems to be unlikely to speed up the diffusion of dye molecules into the mesoporous structure, although it will avoid depletion of the bulk dye solution outside of the TiO₂ film.

A number of studies investigated the effect of dye loading on the DSC performance [85, 87, 95, 97-99]. In a few works [85, 96, 100], a higher dye loading led to an increase in the short-circuit current I_{sc} , while Neale *et al.* [87] observed a disproportionately small effect on the I_{sc} when the dye loading was reduced twofold. The dye uptake was also related to the open-circuit voltage (V_{oc}) [99], the mechanism supposedly being shielding of the TiO₂ from the electrolyte, which reduces recombination of generated electrons from the former to the latter and increases the V_{oc} . However, O'Regan *et al.* [79] recently pointed out that care must be taken in relating the dye loading to the V_{oc} , since the presence of the dye also shifts the TiO₂ conduction band edge, which in itself has an effect on the V_{oc} .

5.6. Diffusion of dye molecules in mesoporous TiO₂ films

Diffusion is a transport phenomenon caused by random motion of species (atoms, molecules or small particles), due to the kinetic (thermal) energy of molecular movement. It is a manifestation of the thermal energy at macroscopic scales, and is classically exemplified by the *Brownian motion* of a particle suspended in a liquid. The root mean square displacement R^2 of a particle subjected to the Brownian motion is, at long times, proportional to the time t :

$$R^2(t) \sim Dt, \quad (5.18)$$

where D is the proportionality constant called the diffusion coefficient. The diffusion trajectories show (statistical) self-similarity: if one zooms in on them, they exhibit statistically the same appearance [104]. This reflects the microscopic origin of diffusion, which is the result of variation of the net momentum from a very large number of molecular collisions.

The evolution of the local concentration of the diffusing species can be described by the *diffusion equation*, which in one dimension can be written as:

$$\frac{\partial c(x, t)}{\partial t} = D \frac{\partial^2 c(x, t)}{\partial x^2}. \quad (5.19)$$

It originates from the *conservation equation*, which describes the conservation of the number of particles in the absence of any particle source or drain:

$$\frac{\partial c(x, t)}{\partial t} + \frac{\partial j(x, t)}{\partial x} = 0, \quad (5.20)$$

where j is the current density of the species. The dependence of the particle current density on the concentration was phenomenologically proposed by Fick in 1855 as a linear variation of j with the concentration gradient:

$$j = -D \frac{\partial c}{\partial x}, \quad (5.21)$$

By substituting (5.21), known as *Fick's law*, into the conservation equation (5.20), one obtains the diffusion equation (5.19) [104].

For diffusion in bulk liquids, the bulk diffusion coefficient D_b can be estimated from the *Stokes-Einstein equation*, assuming that the diffusing species can be represented as spheres with radius a , and a is at least several times larger than the dimensions of the solvent molecules:

$$D_b = \frac{kT}{6\pi a \cdot \eta}, \quad (5.22)$$

where k is the Boltzmann constant, T is the temperature, and η is the viscosity of the liquid [105]. Interestingly, the diffusion coefficient does not depend on the mass of the species. Using this equation for the case of dye Z907 in a solvent mixture of acetonitrile and *tert*-butanol, which was used in Papers 3 and 6, suggests $D_b = 280 \mu\text{m}^2/\text{s}$. Despite the fact that the viscosity of a liquid, at least water, does not significantly differ from its bulk value in pores with sizes down to a few nm [105], the diffusion coefficient of large molecules (that have dimensions comparable with the dimensions of the pores) in porous films is usually a few orders of magnitude lower than that predicted by equation (5.22). Early computer simulations suggested that $D \sim D_b \exp(-a/r_m)$, where a is the effective radius of the molecule, and r_m is the mean radius of the pores [106].

The geometry of a porous structure can be empirically characterized with three parameters: porosity ϵ , tortuosity T and constrictivity δ . *Porosity* is the volume fraction of the medium that is occupied by pores, *i.e.*, it can in principle be filled with gases or liquids. *Tortuosity* reflects the effective diffusion path through the medium, which is often much longer than the thickness of the medium. *Constrictivity* characterizes the variation in the cross-section of the pores along a diffusion path [107]. Using these parameters, the effective diffusion coefficient in a porous medium can be expressed as [107]

$$D_{\text{eff}} = \frac{\epsilon \delta}{T^2} D_b. \quad (5.23)$$

For mesoporous TiO₂ films of the kind used in DSCs, all three parameters play their role. For small molecules like tri-iodide, δ/T^2 can be as high as ≈ 1 (see discussion in [107]). However, for much larger dye molecules, this value can be on the order of 0.001, which is attributed to presence of multiple pore interconnections that are too small for the dye molecule. This would substantially increase the diffusion path, *i.e.*, the tortuosity [107]. In paper 5 of this thesis the value of δ/T^2 is found to be approximately 0.08, which is much larger than the value of *ca.* 0.001 found by Dürr *et al.* [107]. The difference may come from different pore structure, and from the type of the dye and the solvent used in the two works. In some cases, the diffusion process can be additionally complicated and slowed down by aggregation of the molecules in the supplying solution [108].

The considerations above assumed that the diffusing molecules do not adsorb in the porous material, which is obviously not the case for the dye-TiO₂ system considered in this thesis. Adsorption (or any other surface reaction that consumes diffusing molecules) effectively removes the molecules from the diffusion process. Bartlett and Gardner [109] analytically considered a number of diffusion behavior types based on several parameters of the system: the concentration of sites for adsorption compared to the concentration of the molecules in the bulk phase, the degree of saturation of the medium with adsorbed molecules at equilibrium, and the timescale of the adsorption (or reaction) compared to that for diffusion. When the concentration of sites available for adsorption is low, the diffusion is not substantially perturbed by adsorption. When diffusion is fast compared to adsorption, then the molecules diffuse into the medium and reach a constant concentration before significant adsorption occurs. This corresponds to a low sticking coefficient, which means that a molecule must make many attempts to adsorb before the adsorption takes place. In this limit diffusion goes on as if adsorption were essentially not occurring. However, when adsorption happens at a much shorter timescale than diffusion, *i.e.*, the sticking coefficient is high, the situation is quite different. The diffusing molecules are then removed from the solution by adsorption and the local concentration in the solution is lowered compared to the non-sticking case. This in turn leads to a lower diffusion coefficient in the presence of high sticking compared to no sticking. In the case when the sites are fully occupied at equilibrium, the adsorption slows down the diffusion significantly. It then proceeds according to a moving boundary mode, when the sites behind the boundary are fully occupied and the sites ahead of the boundary are empty [109]. This is the situation that we observe and characterize for our dye-mesoporous TiO₂ film system in Paper 5 (there we call the mechanism ‘diffusion-front mode’).

As O’Regan *et al.* pointed out in a recent paper [79], there had been a lack of understanding of the dye impregnation process in the literature. In particular, it was often not realized that since the dyes, which are commonly used in DSC, have high equilibrium adsorption constants for TiO₂ (*i.e.*, stick readily to the surface and stay

there) and since the number of available sites on the surface of a mesoporous TiO₂ film is very large, the dye impregnation process happens in the diffusion-front mode, as discussed above. However, this was realized by Dürr *et al.* [107], who followed the dye loading by UV-vis spectroscopy and observed that at initial stages the kinetics of the impregnation process was the same for TiO₂ films of different thicknesses. This means that at initial times, adsorption happens in a thin layer of a film and the rest of the TiO₂ thickness does not play a role, which implies that adsorption is fast compared to diffusion [107]. In Paper 5 of this thesis, we confirmed quantitatively that the impregnation process is diffusion-limited by studying the diffusion time as a function of different parameters, and successfully explained the experimental results based on the diffusion-front model.

6. Nanoparticle plasmonics for enhancing light absorption in solar cells

The thickness of a solar cell is a very important parameter to optimize. In all solar cell types, there is a trade-off between light absorption, which benefits from thicker cells, and carrier collection, which, due to shorter transport lengths, is favoured by thinner cells. A physically thin, but optically thick solar cell is highly desirable, and one way to achieve this is by trapping light in the photovoltaic material. Higher intensity of light, produced by trapping, leads to more absorption and thus more generated electron-hole pairs. This enables reduction in the solar cell absorber thickness, which is beneficial for two reasons: (i) the amount of material is reduced, which is especially valuable for expensive and/or rare materials, and (ii) the efficiency of charge carrier collection may improve due to shorter transport lengths. The latter effect can increase the efficiency of those solar cells, where carriers have short diffusion lengths (for example, amorphous Si), or, alternatively, a worse material quality could be tolerated in those cells, where charge carrier collection is not an issue (like crystalline Si). Light trapping will, however, not improve the efficiency of a solar cell, which absorbs all light (with the energy above the value of its band gap) anyway.

A new and promising way of managing and trapping light at the nanoscale is by employing plasmonic materials, which has recently been successfully applied to the solar cell research area, and is also investigated in the present work (in Papers 1 and 2). Employing plasmonic nanostructures could allow reducing the solar cell absorber thickness, leading to the benefits discussed in the previous paragraph. This section gives an overview of the research on plasmonic solar cells. It starts with the mechanisms by which plasmon resonance can improve performance of solar cells, and continues with some of the recent results for various cell types. Plasmonics for amorphous Si solar cells is reviewed in more detail, since it is of more direct importance for this work.

6.1. Mechanisms of plasmonic absorption enhancement

Plasmon resonance can enhance light absorption by a solar cell in at least four ways. They are schematically illustrated in Figure 6.1 and include (A) scattering of light into the solar cell, (B) concentrating light to very high intensities in the vicinity of a metal nanoparticle, (C) generation of electron-hole pairs as a result of the plasmon decay, and (D) coupling light into propagating surface plasmon modes [110].

According to (A) above, plasmonic nanoparticles at the resonance frequency (wavelength) efficiently *scatter light*, which leads to a prolonged path of light in the material as compared to the path of non-scattered light. Light scattering from a metal nanoparticle surrounded by a homogeneous medium is nearly symmetric in the forward and backward directions. However, if the media around the particle are not the same, the light will scatter preferentially into the medium with a higher dielectric constant [110]. This is the case if metal nanoparticles are placed on top of a solar cell (Figure 6.1A) with air or another low dielectric constant material above them. Furthermore, if the light is scattered at an angle larger than the critical angle for reflection (16° for a Si/air interface), it will get trapped inside the material [110]. This can generate wave guided (propagating) modes in a semiconductor [111]. These effects prolong the path of light inside the solar cell, which effectively increases the probability of absorption. The nanoparticle size is one of the important parameters that influence the intensity of the light scattered into the solar cell material.

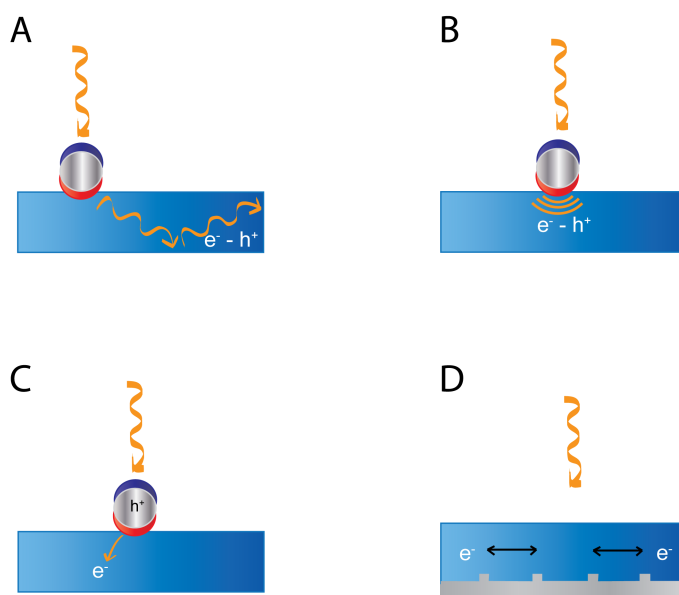


Figure 6.1. Mechanisms of plasmonic enhancement for solar cells. The blue and red regions around the nanoparticle schematically represent the fields from the displaced electron cloud and remaining ion cores, respectively, during a plasmon oscillation. (A) Enhanced *scattering* prolongs the path of light in a solar cell material. (B) Intensified *near-field* around the nanoparticle promotes absorption in the adjacent semiconductor. (C) Plasmon resonance excitation *decays* into an electron-hole pair within the plasmonic nanoparticle, and the electron is transferred into the semiconductor. (D) *Propagating surface plasmon* is excited at the rear metal film, which prolongs the light path in the solar cell material.

Scattering efficiency increases with particle size; on the other hand, it was shown that smaller particles are more efficient in preferentially scattering in the forward direction [110]. This trade-off can be avoided if the nanoparticles are placed at the rear of the cell, in between the glass substrate and the transparent conductive oxide layer.

According to (B) above, the *enhanced electric field* around the plasmonic nanoparticle increases the probability of electron excitations in the surrounding semiconductor, since this probability is proportional to the square of the electric field [14]. In this case the particles can be thought of as subwavelength antennas that store the incident light energy as a plasmon oscillation on the femtosecond timescale [110]. For an efficient coupling of this energy into the surrounding semiconductor, the absorption in the latter has to be faster than the inelastic plasmon decay time, since otherwise the energy will be absorbed in the metal nanoparticle itself. Numerical simulations and analytical treatment performed by Hägglund *et al.* [112-114] have shown that employing the enhanced near-fields, it is possible to absorb a substantial amount of light in a semiconductor as thin as 10-20 nm. Moreover, if the metal-semiconductor nanocomposite is combined with an optimized reflector, the absorption can reach 100% (at a particular wavelength) for *ca.* 10 nm of semiconductor [114]. Provided that the absorption coefficient (or the imaginary part of the dielectric constant) is much higher for the semiconductor compared to the metal, most of this high absorption will take place in the semiconductor [114]. This may provide the background for a new generation of photovoltaics, which represents truly two-dimensional solar cells [112]. However, the details of the interface between the metal and the semiconductor are expected to strongly influence the absorption fractions in the two components. These may include the surface roughness of the metal and the presence of a nanometre thin dielectric spacer (for example, the metal oxide) and have to be optimized carefully, which often is very challenging experimentally.

(C) Third, the plasmon resonance excitation can decay via *exciting an electron-hole pair* in the metal nanoparticle itself. With a proper alignment of the nanoparticle work function and semiconductor conduction band, the generated electron can be transferred into the latter. This would leave the plasmon nanoparticle charged, however, and thus can probably contribute to an increase in the solar cell current only if the particles are not electrically isolated. This process led to plasmonic enhancement of a solar cell performance in some studies [115, 116]. However, it was recently demonstrated by calculations that a solar cell based on injection of charges generated as a result of the plasmon decay may only achieve *ca.* 7% efficiency in an optimized case [117]. This limit comes about when one considers charge injection through a Schottky barrier, formed between the metal particle and the semiconductor. Since metals have high density of unoccupied levels above the Fermi energy, into which electrons can transfer upon absorption of light, many of the excited electrons will not have sufficient energy to overcome the Schottky barrier (because of their broad distribution in energy). On the other hand, the authors claim that if the barrier is small, the reverse

current from the semiconductor to the metal particle will be large, which also leads to a low efficiency for such a solar cell [117].

(D) Fourth, *propagating surface plasmon polariton (SPP)* modes can be excited at the interface of an extended metal layer and a dielectric, at the rear of a solar cell. These excitations can guide the light along the lateral direction of the solar cell, substantially increasing the light path length [110, 118] and thus the absorption probability. However, these propagating modes suffer from relatively high losses. They are beyond the scope of this thesis, which focuses on *localized* (as opposed to propagating) surface plasmon excitations.

Finally, interaction of plasmonic nanostructures with light always results in some dissipation of energy, *i.e.*, light absorption, in the nanostructure itself (as opposed to the desirable absorption in the semiconductor that leads to generation of electron-hole pairs). The plasmon excitations thus decay into electron-hole pairs, which in turn eventually decay into phonons, with heating of the material as the result. Since the conductivity of a semiconductor increases with rising temperature, the heating in a solar cell may lead to an improved photocurrent. However, theoretical estimations by Zhdanov *et al.* [119] that considered heat transfer in nanostructures, suggest that for the commonly used materials irradiated with *ca.* 1 Sun the heating effect will not lead to a temperature increase of more than 1×10^{-3} °K and is thus negligible [119], and not very significant even for concentrated solar power (concentration with focusing mirrors).

6.2. Results for various solar cell types

6.2.1. Plasmonic nanoparticles for monocrystalline solar cells

Making solar cells thinner naturally leads to a decreased amount of photovoltaic material needed, which is especially beneficial for expensive solar cells, like monocrystalline Si cells. Several research groups have worked on incorporating plasmonic structures into c-Si solar cells aiming to make them thinner without compromising light absorption. Schaadt *et al.* [120] demonstrated up to 1.8-fold increase in the photocurrent at a single wavelength (around 500 nm) when Au colloidal nanoparticles were placed on top of a wafer-based c-Si solar cell (Figure 6.2A). Pillai *et al.* [121] observed up to 7-fold enhancements in photocurrent of a 300 μm c-Si cell achieved by depositing Ag particles on top. This enhancement took place in the near-infrared spectral range (here at 1050-1200 nm). Even larger enhancements (up to 16 times) were demonstrated by the same group for a thin 1.25 μm c-Si solar cell [121]. The Ag nanoparticles were in both cases separated from the cell by a 30 nm thick

oxide film. Losurdo *et al.* [122] demonstrated that a heterojunction solar cell of a-Si:H/c-Si benefitted from Au nanoparticles on top; the integrated photocurrent produced under illumination with a close to AM1.5 spectrum increased by 20%.

Several other investigations demonstrated a slight overall improvement in performance of thick c-Si solar cells, with however a *decrease* in photocurrent in the region of plasmon resonance [123, 124]. This decrease was attributed to backscattering of the incoming light and also to dissipation (absorption) in the metal nanoparticles themselves. To avoid the dissipation, *dielectric* nanoparticles were suggested for light scattering [124, 125]. Although an improved performance was demonstrated in this case, the photocurrent was lower than that achieved by applying a standard antireflection coating [124]. In [123], where a decrease in photocurrent was observed experimentally, it was demonstrated by calculations that thinner Si samples would show an enhancement instead.

The effect of plasmonic nanoparticles positioned on top of solar cells with the aim of enhancing light scattering into the cell depends therefore on the properties of the nanoparticles: size, shape, material, surface coverage, etc., and also on the presence

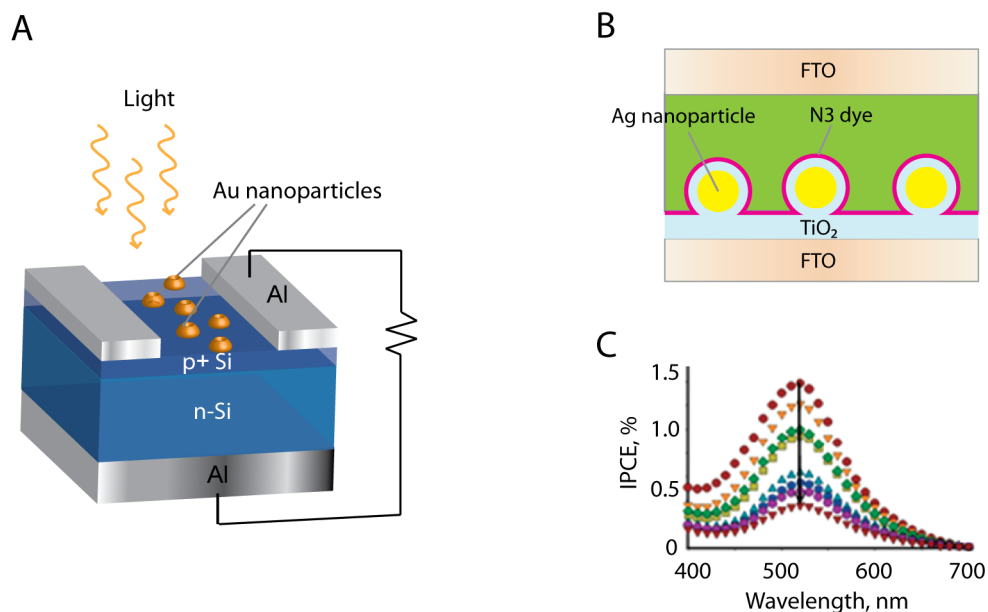


Figure 6.2. (A) Schematics of a crystalline Si solar cell with plasmonic nanoparticles on top used in [120] (redrawn from [120]). Experiments on plasmon enhanced ultrathin dye sensitized solar cell from [126]: (B) schematics of the sample, and (C) IPCE of the obtained solar cells. The top four spectra correspond to amorphous TiO₂, and the bottom four spectra to anatase TiO₂ films. The downward arrow indicates increasing thickness of the TiO₂ films, which was in the range 2.0-4.9 nm for the amorphous films, and 6.5-8.0 nm for the anatase films. (Images redrawn or adapted from [126])

and thickness of the oxide spacer layer in between the cell and the particles.

Optimization of these parameters for crystalline Si solar cells is the subject of the on-going work worldwide [127-129]. Positioning plasmonic nanoparticles at the rear of a solar cell allows avoiding the backscattering problem; a 22 μm c-Si solar cell exhibited a 10% enhancement in the photocurrent with Ag nanoparticles at the rear side, which was further slightly improved by adding an antireflection coating on top of the cell [130]. Munday *et al.* [131] performed calculations to optimize geometry of both the antireflection coating and plasmonic back reflector in order to maximize light absorption in Si films; the predicted enhancements were largest for the thinnest films studied (*ca.* 50 nm).

A thin (200 nm) crystalline GaAs solar cell with Ag nanostructured on top exhibited an 8% increase in short-circuit current, corresponding to an increase in the power conversion efficiency from 4.7% to 5.9% [132].

6.2.2. Plasmonics for organic and dye-sensitized solar cells: a few examples

The first experiments on plasmon enhanced photovoltaics were in fact performed on organic and dye solar cells. As early as 1991 Hayashi *et al.* [133] observed an improved efficiency of an organic solar cell when propagating surface plasmons were excited in a metal contact of the cell. The influence of a *localized* plasmon excitation in metal clusters on performance of an organic solar cell was reported by Stenzel *et al.* [134] in 1995. In their experiments, Cu metal clusters outperformed Ag and Au particles. The enhancement was attributed to the intensified near-field around the particles [134]. Westphalen *et al.* [116] studied a similar system and concluded that the primary mechanism of enhancement in their experiments was generation of an electron-hole pair in the metal clusters and subsequent injection of the electron into the circuit. Nowadays, the research on organic plasmonic solar cells is quite extensive and the results are promising [41, 135-137]. Plasmonic enhancement can allow reducing the thickness of organic solar cells substantially; calculations by Hägglund *et al.* [112] predicted a maximum efficiency of 12% achieved by incorporating Ag nanoparticles into an organic solar cell with the absorbing layer of only 6 nm thick.

The influence of metal clusters on the performance of a dye-sensitized solar cell was reported for the first time in 2000 [138]. Nowadays, considerable research efforts are focused on plasmonics for organic and dye photovoltaics; some of the achievements are reviewed in [41].

An interesting study of plasmonic near-field enhancement in dye solar cells was performed by Standridge *et al.* [126]. The authors investigated the dependence of the photocurrent in a dye solar cell on the distance between the dye molecules and Ag plasmonic nanoparticles. In their samples, this distance was equal to the TiO₂ thickness, as depicted in Figure 6.2B. The cells studied were in principle equivalent to the standard DSCs, but used much thinner (2-8 nm vs several μm) TiO₂ films. The incident photon to current conversion efficiency (IPCE) of these solar cells is shown in Figure 6.2C. The IPCE of a cell without the Ag nanoparticles (not shown) was 0.2% at maximum, and presence of the plasmonic particles increases this value substantially (Figure 6.2C). Furthermore, the IPCE increases with decreasing TiO₂ thickness, reaching 1.4% at maximum for a 2 nm thick TiO₂ film [126]. This is much larger than the maximum achievable IPCE of 0.27% predicted for a flat anatase TiO₂ film. The observed dependence of the IPCE on the distance between Ag nanoparticles and dye molecules further supports the near-field mechanism of the enhancement.

Recently, Sheehan *et al.* [139] incorporated Au plasmonic nanoparticles, coated with a few nanometre thick SiO₂ and TiO₂ shells in various combinations, into the mesoporous TiO₂ films of dye solar cells. All cells with plasmonic particles performed better than those without. Aggregates of 9 nm Au particles coated with 1.6 nm of SiO₂ and *ca.* 2.5 nm of TiO₂ showed the best performance, resulting in the efficiency of 5.5% compared to 2.8% without the nanoparticles [139]. The experiments suggest that the observed effect is mainly the enhancement of dye molecule absorption by the plasmonic near-field, although some contribution from far-field effects (enhanced scattering) cannot not be excluded.

6.2.3. Plasmonics for improving a-Si:H solar cells

There has been a lot of work on trying to improve the performance of amorphous and nanocrystalline Si solar cells using plasmonic nanostructures, especially during the last few years [113, 115, 140-160]. In one of the first works on this subject (2006), Derkacs *et al.* [140] reported an 8% enhancement in the photocurrent of a 240 nm thick a-Si:H solar cell, achieved by depositing colloidal Au nanoparticles on top of the cell. In most of the recent studies, Ag was the plasmonic material of choice due to its low absorption coefficient (and thus low heat dissipation losses) in the visible and near-infrared regions [114]. A drawback of Ag is its susceptibility to oxidation; however, the oxide may be reduced and the surface stabilized by a hydrogen atom treatment, as suggested in a recent work [161].

The most researched plasmonics-related approach for a-Si:H solar cells has been employing resonances supported by a rough *back reflector* of the cell ('back' in this context means that light reaches it last; see Figure 6.3). In this configuration, the metal

back reflector (often Ag) is nanostructured so that it supports plasmon resonance. Enhanced scattering associated with the resonance increases the light path inside the a-Si:H absorber; this can be thus classified as a far-field effect (Section 6.1). In this configuration the reflector is often separated from the a-Si:H absorber by *ca.* 100 nm of a transparent conducting oxide (TCO), which acts as a diffusion barrier between the semiconductor and the metal, and also prevents coupling to surface plasmon polariton modes at the metal surface (the latter tends to increase the optical losses in the metal at visible light frequencies) [149]. However, depending on the parameters of the whole system (layer thicknesses, optical constants, geometry of the structures on the metal surface *etc.*), coupling to propagating surface plasmon modes may still occur and may be beneficial [110]. Due to the presence of the TCO spacer, the near-field effect is not expected to play a significant role. State-of-art a-Si:H cells [32] actually traditionally employ this configuration, since the back reflector is rough due to the layers of the cell being deposited onto a specially roughened glass/TCO substrate (often this is commercially available Asahi glass [162]). Figure 6.3A illustrates a similar structure. The plasmonic-related research in this context has therefore focused on understanding the mechanisms and testing back reflectors structured in various ways, both random and periodic.

Substantial enhancements have often been demonstrated using this approach [141, 142, 144, 146-149, 151, 154, 159]. Zhu *et al.* [144] fabricated a 280 nm thick a-Si:H solar cell

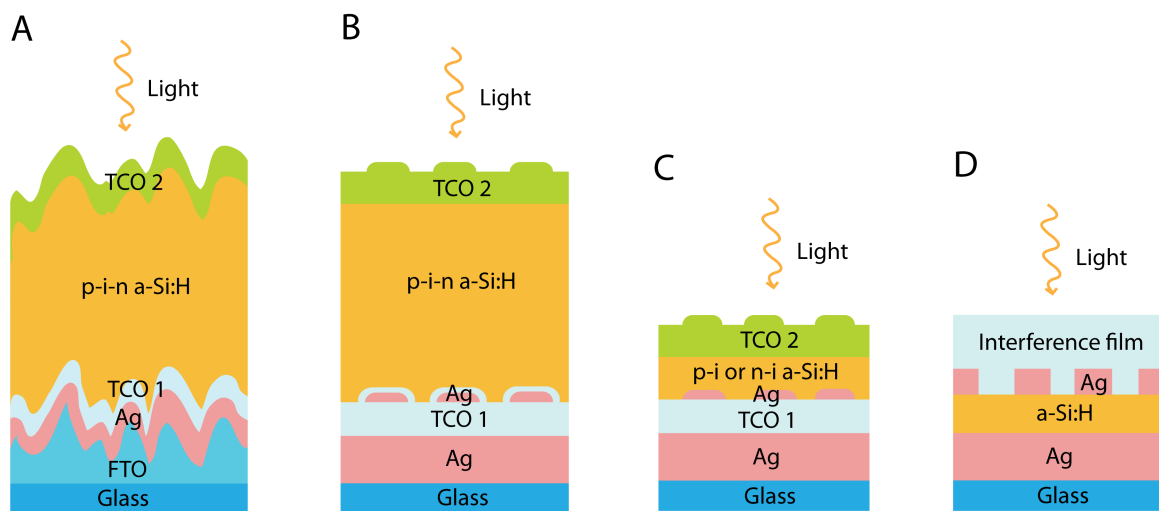


Figure 6.3. Schematics of a-Si:H solar cells with different plasmonic nanostructures for enhancing light absorption: (A) rough back reflector (redrawn from the work by Tan *et al.* [159]); (B) plasmonic nanoparticles incorporated into the back TCO for enhanced light scattering (redrawn from [159]); (C) nanoparticles embedded into a very thin (*ca.* 20 nm) a-Si:H layer for the near-field enhancement mechanism. A similar structure was used by Moulin *et al.* [115]. (D) Plasmonic metamaterial structure with a very thin a-Si:H layer (15 nm) as suggested by Wang *et al.* [160].

on an Ag metal substrate with conical features ('nanodomes'), and demonstrated an efficiency of 5.9% compared to 4.7% for an equivalent cell with a flat reflector [144]. The simulations accompanying the work suggest that the plasmon enhancement originates from coupling the incident light into trapped modes in the a-Si:H film, which substantially increases the light path in the solar cell. Ferry *et al.* [141] used a similar approach for a 500 nm thick a-Si:H solar cell and demonstrated an increase in efficiency from 4.5% for flat cells to 6.2% for cells with a periodically nanostructured plasmonic back reflector. The same group in their following publication [142] fabricated cells with thinner a-Si:H layers (160 and 340 nm) on periodic plasmonic reflectors, and surprisingly achieved even higher energy conversion efficiency of 6.6% - for both thicknesses. Hsu *et al.* [151] demonstrated a cell with 250 nm of the a-Si:H absorber film fabricated on a nanostructured back reflector with the efficiency of 9.7% (the reference flat cell efficiency was 8.1%). A similar high efficiency of 9.6% was achieved by Ferry *et al.* [149] with a yet thinner - 90 nm - intrinsic a-Si:H layer, using a periodically structured back reflector. This efficiency was higher than that of the corresponding flat cell and a cell fabricated on the Asahi glass. All these results strongly support the fact that charge carrier collection is a bottleneck in such a defective material as a-Si:H, and it is therefore highly desirable – and possible by using plasmonics – to reduce the solar cell thickness without compromising light absorption.

Enhanced scattering from plasmonic back reflectors can improve photocurrent in thick (on the order of several μm) nanocrystalline Si solar cells as well [147, 148, 157].

A similar approach, which aims at utilizing the enhanced scattering from plasmonic nanostructures, is to incorporate nanoparticles into the rear TCO of the cell (Figure 6.3B). Tan *et al.* [159] showed that performance of a 300 nm thick a-Si:H cell with a back reflector with a structure of flat Ag – TCO 60 nm – Ag nanoparticles – TCO 30 nm was similarly good as that of a reflector on Asahi glass. Ho *et al.* [150] experimented with single and double layers of Au nanoparticles embedded into the rear TCO, and achieved the best result (efficiency 6.5%) with the double layer structure. Tsai *et al.* [143] performed simulations of a-Si:H solar cells with Au, Ag or Al nanoparticles on top or/and at the rear of the cell, separated from the absorbing layer by 20-60 nm of a TCO. They concluded that the best integrated absorption enhancement of about 50% can be achieved with Al nanocylinders fabricated on both top and rear of the cell.

Near-field effects, which utilize the enhanced electrical field close to the surface of a nanostructure, have been investigated only in a few works for a-Si:H solar cells. Santbergen *et al.* [158] studied the performance of a-Si:H cells (with a *ca.* 300 nm thick absorber) with a flat back reflector and Ag nanoparticles incorporated into the front, the rear and the middle of the a-Si:H layer, respectively. The particles were in direct contact with the a-Si:H and thus three mechanisms may have played a role: the near-field, the far-field effects, and photoemission of electrons from metal nanoparticles. Particles positioned in front and in the middle of the a-Si:H film degraded the

photocurrent of the cell, while having particles at the back resulted in similar or slightly larger photocurrents. The worsened performance probably originated from absorption of light by the particles themselves, instead of the a-Si:H film.

Another example of having plasmonic particles in direct contact with an a-Si:H layer is shown in a work by Moulin *et al.* [115]. Their impressively thin solar cell, consisting of a p(n)-i junction of only 40 nm, had Ag nanoparticles in between the a-Si:H film and the rear TCO (Figure 6.3C). The authors observed an increased quantum efficiency at wavelengths larger than 750 nm, and since this corresponds to energies below the a-Si:H band gap, the enhancement was attributed to photoemission of electrons from the nanoparticles, probably as a result of the plasmon excitation decay into electron-hole pairs. However, the near-field enhancement of light absorption should perhaps not be excluded either, since it is possible that it influenced excitations from defect states lying in the band gap of a-Si:H (which need a lower energy than the band gap to excite electrons into the conduction band). This latter effect was claimed in the work by Lükermann *et al.* [155], who compared the effect of Ag nanoparticles incorporated into n-i, p-i and n-i-p configurations and concluded that the enhancement of light absorption in the near-infrared (below the band gap of a-Si:H) comes from excitations from the defect states. The photocurrent generated in the visible range was either similar or lower for devices that had nanoparticles [155].

Despite the near-field plasmonic enhancement of a-Si:H solar cells has not been studied much experimentally and the few existing works do not seem to show great promise, some results of theoretical modelling and computer simulations predict a large potential in employing this mechanism. Hägglund *et al.* [112] theoretically estimated a maximum efficiency of 18% for an optically optimized a-Si:H solar cell with incorporated Ag nanoparticles, where the absorber is approximately 20 nm thick. This cell is based on prolate Ag nanoparticles surrounded by a 10 nm thick a-Si:H shell, which are positioned onto an Al reflector covered with a dielectric film. The thickness of this dielectric spacer is chosen to achieve a constructive interference at the Ag-a-Si:H film position at the wavelength of the plasmon resonance.

The near-field plasmonic enhancement of light absorption in ultrathin a-Si:H films has been studied in the present thesis, experimentally and with computer simulations (Papers 1 and 2). The results of Paper 1 demonstrate enhancement caused by the near-field plasmonic effect on very thin a-Si:H films, and quantified it as a function of the a-Si:H film thickness. The largest light absorption enhancements could be achieved for ca. 10 nm thick a-Si:H films. In Paper 2, high aspect ratio plasmonic structures – Ag nanocones – were used films in combination with a reflector and a dielectric spacer layer to improve light absorption in 20 nm thick a-Si:H. The highest absorption demonstrated could produce an ideal photocurrent of 12.5 mA/cm², which is 75% of the value for the confirmed best a-Si:H cell (although the latter value is likely the stabilized photocurrent, which is usually ca. 20% less than the initial one).

While incorporating plasmonic nanostructures into a-Si:H solar cells has in many cases improved the light absorption by the a-Si:H layer, the presence of these metallic structures may also influence the charge collection. If this is the case, it will be reflected in the values of the photocurrent, but also in the open-circuit voltage, V_{oc} , and the fill factor, FF . Since a nanostructured back reflector is usually employed together with *ca.* 100 nm of a transparent conducting oxide, there is no direct contact of the metal and the a-Si:H. The V_{oc} and FF are thus expected to remain similar to those of the reference cells, and this was indeed observed in a number of works [147, 149, 151]. This was also the case when plasmonic nanoparticles were embedded into a TCO [150, 159]. However, if the plasmonic reflector exhibits large height variations, this may lead to poor properties of the subsequently deposited layers and decreased solar cell performance [151]. The situation when metal nanoparticles are in direct contact with an a-Si:H layer is expected to be more tricky, since the defect states arising upon introducing metal into a-Si:H may act as traps for charge carriers. However, in the work by Moulin *et al.* [115], where there was a direct contact between Ag particles and the a-Si:H, V_{oc} and FF decreased only slightly, and in the work by Santbergen *et al.* [158], these parameters did not change significantly. Moreover, Kim *et al.* [152] suggested that metal nanoparticles may in some cases help improving the fill factor, by for example establishing an ohmic contact between an a-SiC:H layer (which is sometimes used to improve the V_{oc}) and the adjacent TCO layer.

Some authors suggested that as far as the scattering (far-field) mechanism of plasmonic enhancement is concerned, dielectric nanoparticles might outperform metallic ones, since there is no absorption of light in the former [145, 163]. A similar situation might apply to nanostructured plasmonic reflectors - they introduce roughness which itself may promote scattering and light trapping, even without a metal involved. Battaglia *et al.* [146] demonstrated a-Si:H solar cells (of a conventional thickness of 250 nm) with a high efficiency of *ca.* 11% fabricated on periodically and randomly structured substrates, without any metal reflector. Kuang *et al.* [153] demonstrated an ultrathin (25 nm) a-Si:H cell with a 3.6% efficiency on a very rough substrate made of ZnO nanorods and 20 nm Ag.

Finally, another recent approach to enhance light absorption in a-Si:H solar cells involving metallic nanostructures cannot be easily classified in terms of the four plasmonic enhancement mechanisms described in Section 6.1. Wang *et al.* [160] proposed an a-Si:H solar cell of only 15 nm thick, sandwiched between a checker boarder-like Ag pattern, embedded into a dielectric film, and a flat Ag film (Figure 6.3D). The light absorption of such a cell could generate an efficiency of up to 15% (and a current of *ca.* 20 mA/cm²), provided that all the charge carriers are collected. Massiot *et al.* [156] proposed a similar structure based on a 90 nm thick a-Si:H film placed in between a flat Ag reflector and a pattern of silver nanostripes. The a-Si:H layer was separated from the metal by 15 nm of a transparent conductive oxide. This solar cell is

predicted to generate 14.6 mA/cm^2 , if all light absorption generates useful charge carriers that are collected.

7. Experimental methodology

This chapter gives an overview of the experimental techniques used in this work. Section 7.1 describes the fabrication techniques, namely *photolithography* that was used for fabricating electrode patterns in Paper 1; *hole-mask colloidal lithography (HCL)* and *thin-film deposition* methods employed for producing plasmonic nanoparticles in all papers; *plasma-enhanced chemical vapour deposition (PECVD)*, by which a-Si:H films in Papers 1 and 2 were fabricated. The measurement and characterization techniques are described in Section 7.2. They include the *photoconductivity* measurements from Paper 1, the *indirect nanoplasmonic sensing* technique from Papers 3, 5 and 6, the *quartz crystal microbalance with dissipation monitoring (QCM-D)* technique from Paper 4, and also more general characterization tools that have been routinely employed: *light transmission* and *absorption* measurements, the *ellipsometry* technique and *scanning electron microscopy*.

7.1. Fabrication techniques

7.1.1. Photolithography

Photolithography is a widely used technique for transferring geometric patterns from a mask to a substrate. It employs a *photoresist*, which is an organic polymer material that changes properties when irradiated by (typically) ultraviolet light [164].

The photolithography process steps usually are: wafer cleaning, photoresist deposition, prebaking, mask alignment, exposure, and development. The main photolithography and lift-off steps are illustrated in Figure 7.1A. A cleaned substrate is coated by a photoresist, and is revolved at a high speed (typically 3000-6000 rotations per minute). At these speeds, centrifugal force causes the solution to flow to the edges, and eventually off the substrate, leaving a thin film [164]. This process is called *spin-coating* and produces a constant thickness of the photoresist across the substrate. The thickness is proportional to the polymer concentration and viscosity, and approximately inversely proportional to the spinning speed until limited by the molecule size (polymer chain length). To remove the residual solvent left in the polymer film after spin-coating, substrates are prebaked at up to 150 °C. The samples with resist are then transferred to an *exposure* system, which in the simplest case is a UV lamp illuminating the wafer through a mask. The mask is usually a glass or quartz plate with a thin metal film that reproduces the desired pattern. During exposure, the light reaches the resist only in places where the mask is transparent; since the resist

changes its properties on interaction with (UV) light, in this way the pattern on the mask is transferred to the resist.

Next comes *development*, which transforms the latent resist image formed during exposure into a pattern on the substrate, covered by resist in some places and empty in others. The development can be done either by wet chemistry (by dipping the wafer into special organic solvents) or by dry etching in plasma. The resist can be of a positive or negative type (Figure 7.1A). *Positive resists* become more soluble in the

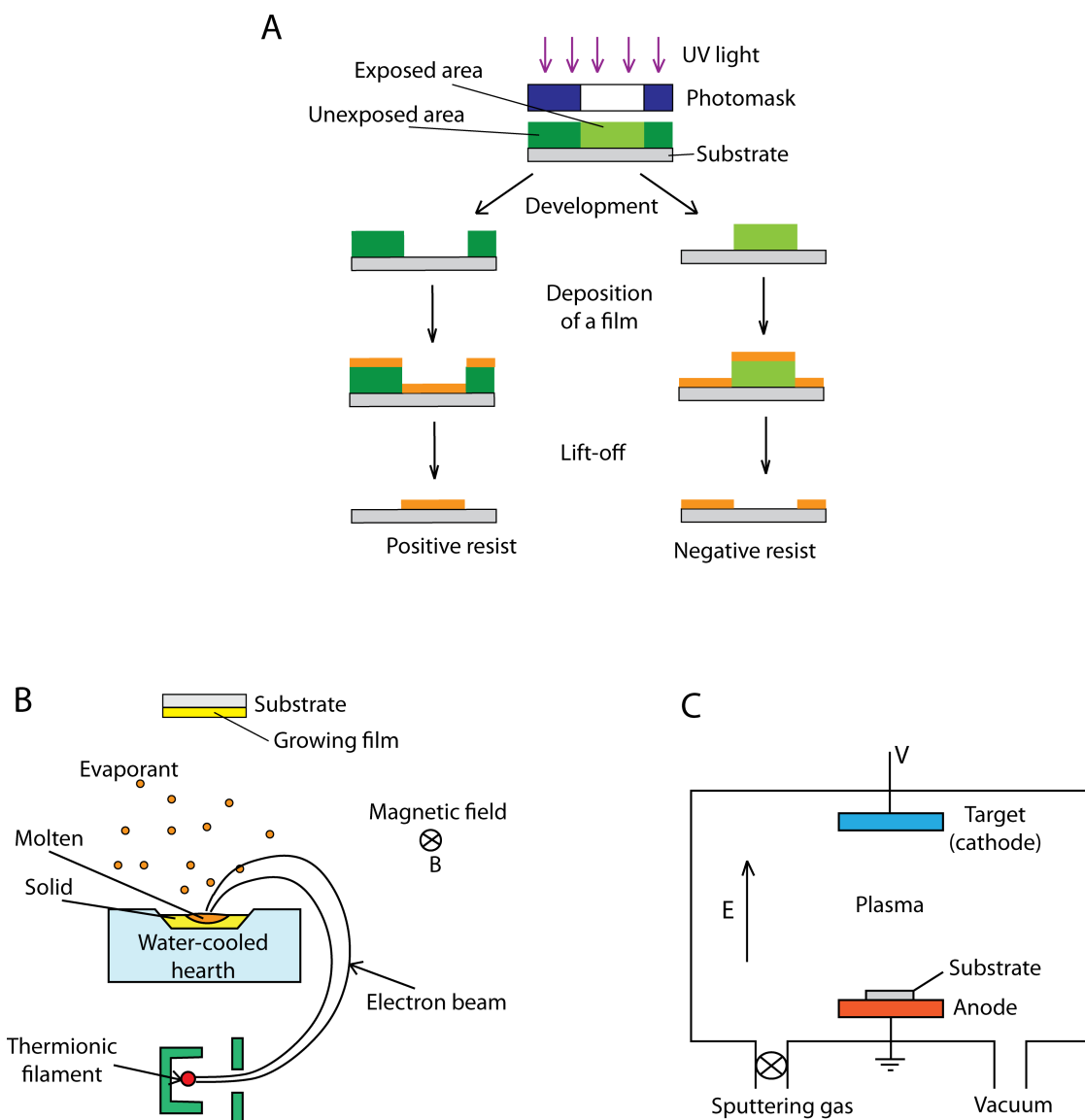


Figure 7.1. (A) Schematics of photolithography and lift-off processes for a positive and negative resist. Schematics of basic thin-film deposition techniques: (B) electron-beam evaporation, and (C) sputtering.

developer after exposure to the UV light, and are removed by the developer. Therefore, the openings in the mask produce areas of the substrate not covered by the resist. A *negative resist* behaves in the opposite manner; exposure to the UV light polymerizes it, and it becomes more difficult to dissolve. Thus, the negative resist remains on the surface wherever it was exposed, and its pattern is inverted to the one of the metal film on the mask.

Next, a mild oxygen plasma treatment is often used to remove a thin film of resist that may be left on the bare substrate areas after the development. Sometimes before etching or depositing a material, the wafer is post-baked (hard-baked). This removes residual solvents and strengthens the resist. After this, a thin film is usually deposited using techniques discussed in Section 7.1.2. The film will cover both bare substrate areas and the photoresist, but by applying a special solution, the resist can be removed (*lifted off*), together with the film on top of it. The film deposited directly on the substrate will stay and form the desired pattern (Figure 7.1A).

To achieve a good lift-off, it is important that the film deposited directly on the substrate is disconnected from the film deposited on the resist surface, since the latter is supposed to be removed, while the film on the substrate should stay. This can be achieved if there is a gap between the film on the substrate and the surrounding resist. This can be produced in a few ways, for example, by using a double layer resist system, consisting of a photoresist on top of a spacer (lift-off) layer [165]. The lift-off layer is either more sensitive to the exposure dose, or dissolves better in the developer. This leads to formation of undercuts, which create gaps between the photoresist and the material deposited afterwards.

7.1.2. Thin-film deposition by evaporation and sputtering

Deposition of thin films by evaporation is based on the evaporation that occurs to any material when it is heated to enough high temperatures. The vapour of the material is then allowed to condense onto a substrate. The whole process is executed in vacuum, otherwise the material would react with the surrounding gases and for example oxidize. (The word ‘vapour’ is thus somewhat incorrect, since in vacuum the ‘vapourised’ atoms/molecules usually move in straight paths to the substrate, without collisions.) *Resistive evaporation* represents one of the oldest thin film deposition techniques, and is done by passing a high current through heaters (e.g., tungsten boats or wires, or by heating stable oxide or ceramic compound crucibles) containing the desired material. This method is simple to implement, but it can spread contaminants that are present in the heater material. Another disadvantage of the method is that the relatively low input power does not allow evaporation of materials with high melting points/low vapour pressures at high rates [166].

Electron-beam evaporation eliminates the disadvantages mentioned above. In this process, a high-intensity e-beam (3 to 20 keV) is focused on the target material that is placed in a niche in a water-cooled hearth (Figure 7.1B) [164]. With the help of a magnetic field, the electron beam is directed onto the material to be evaporated. The material melts locally, forming its own crucible, and thus eliminating the contact with the hearth. The hearth-material interface stays cool, which results in much less source contamination problems than in the case of resistive heating. Moreover, e-beam evaporation can provide high deposition rates (up to 50-500 nm/min). The disadvantages are that the process might induce X-ray damage to the substrate (at voltages higher than 10 kV, the electron beam will cause significant X-ray emission), and that the deposition equipment is more complex.

Sputtering is a process in which an energetic particle strikes a surface with sufficient energy and momentum so that one or more of the atoms on the surface are ejected from it [167]. The incident particle could be an ion or an atom, but most often inert gas ions (e.g., Argon) are used (electrons have enough energy but lack the momentum). The sputtered atoms can land onto a substrate and form a thin film in much the same way as during evaporation, although the atoms landing on the substrate are normally more energetic compared to the case of evaporation. Having a significant kinetic energy, these atoms may cause secondary sputtering and rearrangements (annealing) at the sample surface, which can change the film microstructure. This produces films of different properties compared to evaporated films. Differences can for example be in the grain size, degree of crystallinity, defect densities, and roughness.

A sputtering system is usually a vacuum chamber with two electrodes, between which a discharge *plasma* is generated (Figure 7.1C). *Plasma* is a partially ionized gas composed of ions, electrons, and neutral species that together are electrically neutral when averaged over all the particles. Positive ions from the plasma are accelerated toward the negative electrode (cathode), which is the target, and sputter the atoms off the target. The sputtered atoms move in all directions and also reach the anode, where the substrate is placed [166]. The potential applied to the electrodes can be DC or RF (radio frequency).

In *magnetron sputtering*, a magnetic field perpendicular to the electric field is introduced. Electrons of the plasma are then subjected to crossed electric and magnetic fields, and thus experience a spiral motion. In this configuration the electrons, which otherwise move toward the anode, can instead be confined near the target, enhancing the sputtering efficiency there [166]. Magnetron sputtering allows achieving at least an order of magnitude higher deposition rates than conventional sputtering techniques.

To produce compound material films (for example, oxides and nitrides), *reactive sputtering* is often used. In reactive sputtering, the sputter gas is mixed with a reactive gas, for example, O₂ or N₂ to form oxides or nitrides, respectively. In general, formation of a compound occurs at the target surface, sometimes on the substrate surface, and not in the gas phase or in flight. Compounds generally have a much lower sputter yield than the metal they are formed from. In this work, reactive sputtering was used to fabricate TiO₂ thin films.

7.1.3. Hole-mask colloidal lithography

Colloidal lithography is a novel lithography method, which uses a self-assembled layer of colloidal nanospheres as a lithography mask [168]. This method can provide resolutions beyond those achievable in photolithography (feature size of down to 10 nm versus about 100 nm in photolithography). *Hole-mask colloidal lithography* (HCL) is a more versatile extension of the general colloidal lithography [169]. It uses a sacrificial polymer layer combined with sparsely packed colloidal nanoparticles to produce a mask for subsequent evaporation, in a process described below [168].

The main steps of an HCL process are shown in Figure 7.2A. The fabrication starts with spin-coating a thin polymer layer, which is then exposed to a mild oxygen plasma to make it more hydrophilic. Next, the sample is coated with a polyelectrolyte solution in water, which after rinsing forms a thin charged layer on the surface. A suspension of polystyrene (PS) colloidal particles in water is then pipetted onto the sample, and rinsed with water after 1 min. The PS particles have a surface charge that is of opposite sign to the charge of the polyelectrolyte. The electrostatic attraction between the particles and the surface, in combination with mutual repulsion between the particles, leads to formation of a quasi-random arrangement of particles (Figure 7.2B). It is not strictly random because the PS particles tend to stay away from each other since they are charged. Thus there will be a tendency that they arrange with a rather narrow variation in the inter-particle separation [170]. The average interparticle distance depends on the value of the particle surface charge and can be decreased by partly screening the charge (e.g., via adding a salt to the particle suspension, which affects the Debye screening length). The latter approach was used in Paper 6, where NaCl salt was added to the PS particle suspension to achieve higher coverages of the fabricated nanocones.

After the formation of a quasi-random pattern of PS particles, a thin metal film (of a material resistant to oxygen plasma, often gold or chromium) is evaporated onto the sample. The PS particles are then stripped away with a tape, which leaves the surface covered with a metal film with holes (Figure 7.2A). This film serves as an etching mask in the subsequent oxygen plasma ashing process; the polymer film is etched away

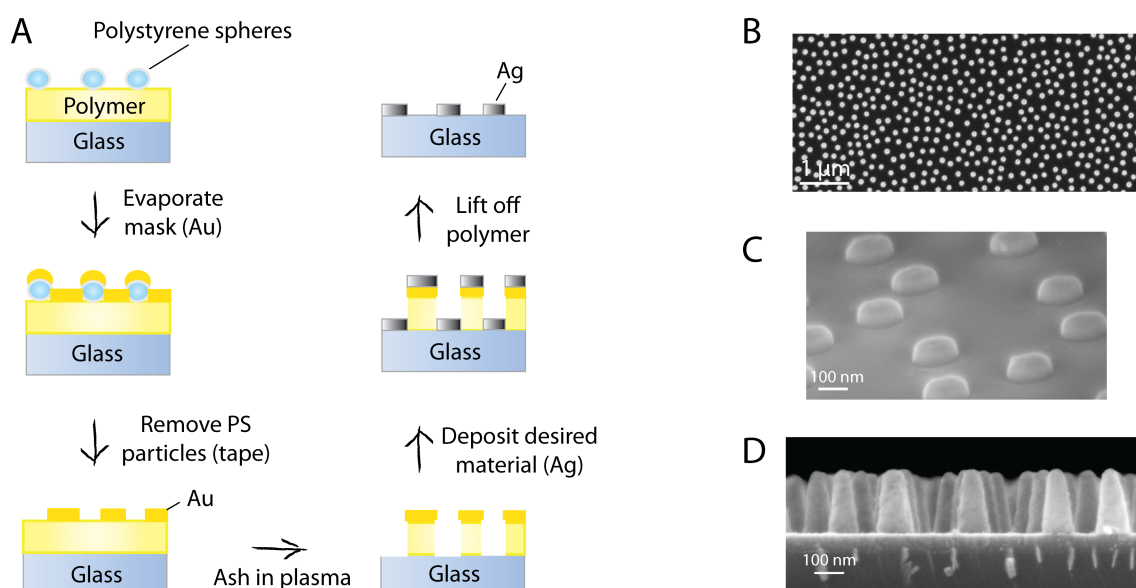


Figure 7.2. (A) The main steps of the hole-mask colloidal lithography process. Scanning electron microscope (SEM) images of Ag nanoparticles obtained by HCL: (B) cones *ca.* 110 nm in diameter, top view; (C) cylinders 60 nm in diameter, 40 nm high, coated with 9 nm of a-Si:H film; (D) the same cones as in (B), side view.

only in places that are not protected by the metal film. Then a desired material is evaporated onto the sample, and the polymer film is then dissolved in an appropriate solvent (lifted off). The lift-off process removes the metal film covering the polymer, while the film in the holes, which is in direct contact with the substrate, remains. The resulting sample has therefore a (quasi-) random pattern of metal nanodiscs of diameter determined by the PS sphere diameter, and a height corresponding to the thickness of evaporated metal. Typical nanodisc (nanocylinder) patterns obtained in HCL are shown in Figure 7.2C.

The HCL technique can be easily modified in order to fabricate particles of other shapes than cylinders, for example, ellipses, particle dimers or cones [168]. Ag nanocones made by HCL were used in Paper 2. During evaporation of the desired particle material through the hole-mask (see Figure 7.2A), the hole diameter gradually decreases due to some evaporated material landing onto the hole walls. Eventually, the holes would close and the corresponding evaporated nanostructure would have a cone shape, like those in Figure 7.2D.

7.1.4. Plasma enhanced chemical vapour deposition for producing a-Si:H films

The most common method to deposit a-Si:H films is plasma enhanced chemical vapour deposition (PECVD). In this process, a plasma is created by ionizing a gas (silane SiH_4 in the case of a-Si:H), and the produced gas species land on a substrate forming a thin film. There are several types of species generated from a given gas; for SiH_4 , these include reactive neutral species SiH , SiH_2 , SiH_3 , H and H_2 , and corresponding ionized species, such as SiH^+ , SiH_2^+ etc. [171]. Reactions between these species in the gas phase and on the substrate produce the growing film. The plasma is created by applying an RF or DC voltage to electrodes in a vacuum chamber, similarly to the mechanism used in the sputtering technique.

The PECVD process has several parameters that influence the quality of deposited films: the pressure and flow rate of the gases, the substrate temperature, and the applied power [35]. The gas pressure determines the mean free path of ionized species and thus controls whether reactions take place in the gas or at the growing film surface. The power influences the dissociation rate of the gas and therefore the film growth rate. The substrate temperature determines mobility of species on the surface, which in turn influences annealing of the film, and the temperature also affects rates of reactions on the growing film. It is generally considered that high-quality a-Si:H films are produced at temperatures of 200-300 °C, from pure or hydrogen-diluted SiH_4 , and at a relatively low power [35]. The process used for making a-Si:H films in this thesis differs somewhat from these optimal conditions, as described in Paper 1.

7.2. Characterization techniques

7.2.1. Photoconductivity measurements

In this work photoconductivity measurements of a-Si:H thin films were performed in a home-built setup shown in Figure 7.3. The a-Si:H film was deposited onto a glass substrate with a contact pattern (Figure 7.3A), which was fabricated by photolithography. The chip had 7 measurement areas 10 μm wide and 2 mm long, defined by the thin electrode lines. The lines were connected to larger pads. The chip was placed into a ceramic cell (Figure 7.3B), where Au-coated pins contacted the electrode pads on the chip. Conductivity between pairs of adjacent electrodes was measured under a bias of 1 V using a Gamry potentiostat in a two-electrode configuration. This instrument is capable of measuring very small currents, on the order of 1 fA. During the measurements, the cell was continuously purged with nitrogen, to avoid moisture and oxidation of the chip. The measurement cell and the

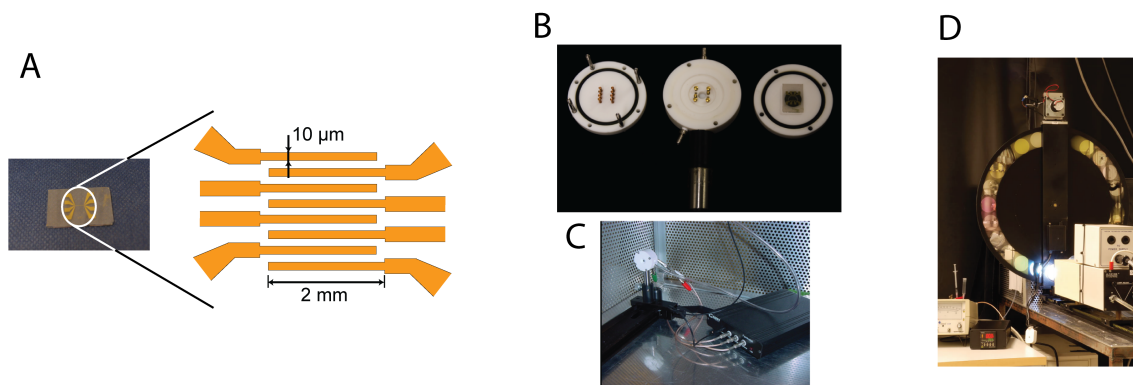


Figure 7.3. Photoconductivity setup used in this work (Paper 1). (A) A glass chip with the electrode pattern. (B) Measurement cell opened and (C) the cell at work, attached to the potentiostat. (D) The xenon arc lamp illuminating the cell (not visible) through filters on the wheel.

potentiostat were surrounded by a Faraday cage, to minimize perturbations and noise pick up from external electromagnetic fields.

To measure photoconductivity, the chip was illuminated with a 75 W xenon arc lamp through a set of band-pass filters. The filters covered a range from 420 to 820 nm in intervals of 20 nm. In this configuration, the light intensity on the sample was 0.3-1.5 mW/cm² for different filters. The filters were mounted on a wheel (Figure 7.3D), which was turned automatically after a desired time interval. The current was recorded as a function of time, and converted to current as a function of wavelength. This current spectrum was additionally normalized by coefficients corresponding to photon fluxes reaching the chip in the given setup after each filter.

7.2.2. Light transmission and absorption measurements

To deduce information about dielectric functions of a material and/or fraction of light absorbed and scattered by a given sample, transmission and absorption measurements are used.

A basic scheme of a transmission measurement is shown in Figure 7.4A. Light from a white light source passes through a monochromator to separate different wavelengths, and arrives to the sample. The sample may absorb and scatter some light, and the remaining transmitted light is collected by the detector. *Transmittance* is defined as the ratio between the intensity of the transmitted light I and the intensity of the incident light I_0 , i.e., $T = I/I_0$. Extinction, E , expresses the fraction of

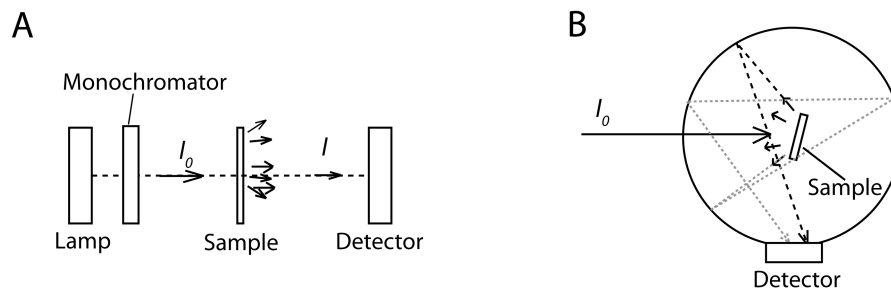


Figure 7.4. Schematics of (A) a transmission measurement setup and (B) an integrating sphere for measuring absorbance.

light that was absorbed and/or scattered by the sample, and is $E = 1 - T$. Extinction and transmittance are usually recorded as functions of wavelength; Figure 4.4A shows examples of extinction spectra of plasmonic nanodiscs.

Absorption of light can be measured in a spectrophotometer with an integrating sphere accessory [172]. The integrating sphere is a sphere with walls made of a highly reflecting material, with a detector embedded at a fixed position (Figure 7.4B). A sample is placed in the middle of the sphere, and illuminated through the entrance opening. Light that is both transmitted through the sample and scattered at different angles reflects off the walls multiple times and eventually reaches the detector. In this way all light that is not absorbed by the sample is collected (exception being a tiny portion that is reflected at the normal direction and leaves the sphere through the entrance opening; this can be minimized by tilting the sample properly). In this way, the fraction of light absorbed in the sample (the *absorbance*) can be directly deduced. If both the extinction and absorbance are measured, the scattering fraction can be calculated as $Sca = Ext - Abs$.

7.2.3. Indirect nanoplasmonic sensing measurements

The idea of the indirect nanoplasmonic sensing (INPS) was presented in Section 5.1, and the home-built setup used in the present work is shown in Figure 7.5A-C. The incoming and transmitted light is guided by optical fibres, which are mounted on a frame together with a sample holder. For measurements in gases and liquids, a flow cell is used, which allows dynamic changing of the environment for the specimen while collecting spectra from the same spot. A peristaltic pump pumps the fluids through the cell at a desired rate.

The plasmonic nanoparticles used in this work are Au discs fabricated by the HCL process, described in Section 7.1.2. The dielectric layer is a sputtered TiO₂ film of various thicknesses (ca. 10-100 nm). The data were collected and analysed using *Insplore* software [173] based on data analysis routines described in [174]. The most important sensing parameter employed was the plasmon resonance energy (peak wavelength); additionally the full width at half maximum (FWHM), the value of extinction (extinction amplitude) at the peak wavelength, and in addition other quantities were sometimes used.

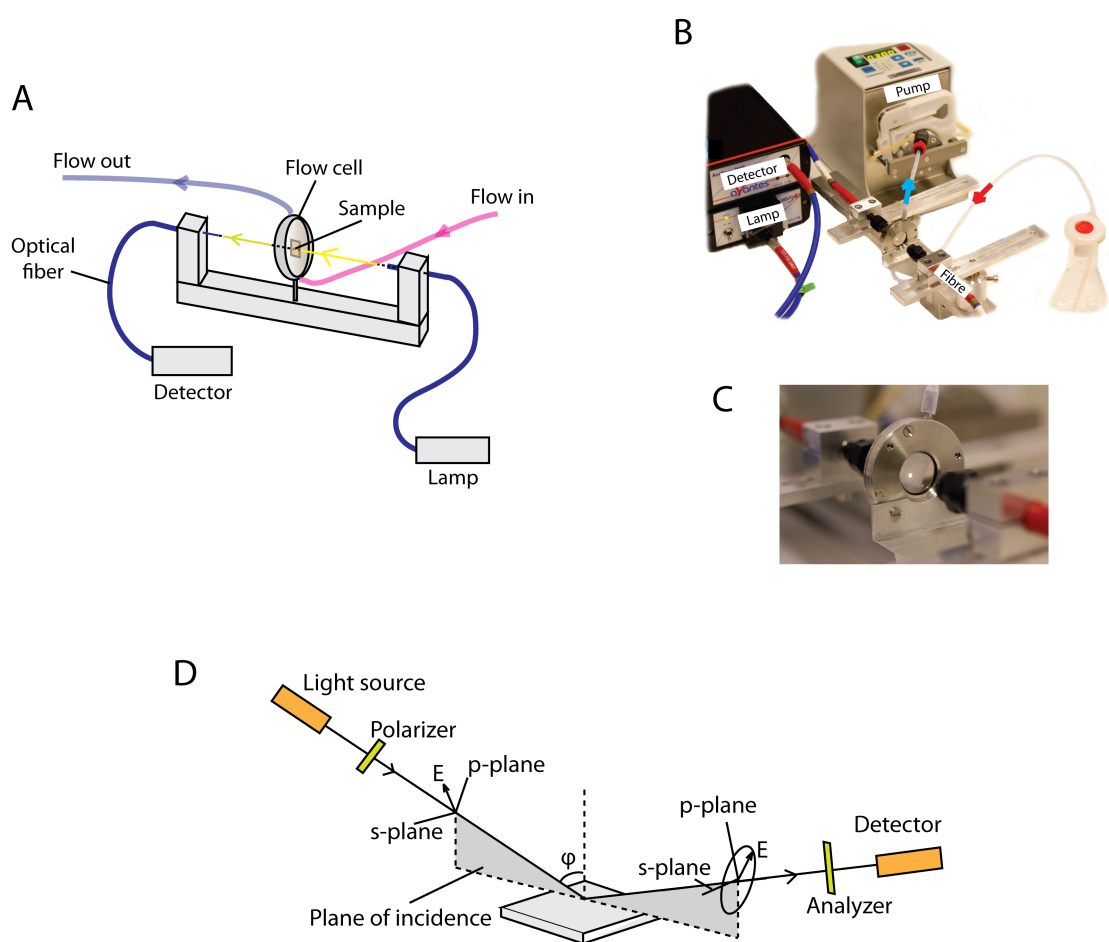


Figure 7.5. The INPS setup used in this work: (A) schematics, (B) the actual setup, and (C) a close-up on the measurement cell with a porous TiO₂ film sample inside. (D) The basic scheme of an ellipsometry setup. The incident light, which is linearly polarized, becomes elliptically polarized after reflecting off the sample (modified after [175]).

7.2.4. Spectroscopic ellipsometry

Ellipsometry is an optical characterization technique for thin films, which measures the change in polarization of light reflected off a studied film [176]. A linearly polarized light is shed at oblique angles onto a sample, and the reflected light is elliptically polarized, with characteristics depending on the film thickness and complex refractive index. If the sample consists of a number of well-defined homogeneous layers, ellipsometry can achieve a thickness determination resolution below 1 nm.

The basic scheme of an ellipsometry setup is shown in Figure 7.5D. Light emitted from the source is linearly polarized after passing through the polarizer. Light reflected from the sample passes through the second polarizer (analyser) and is collected by the detector. The reflected light can be decomposed into two perpendicular components (Fresnel reflection coefficients), one in the plane of incidence (r_p) and the other perpendicular to it (r_s), see Figure 7.5D. The ratio between these components is determined at each angle of incidence and wavelength, and can be represented as

$$\frac{r_p}{r_s} = \tan(\Psi)e^{i\Delta}, \quad (7.1)$$

where $\tan(\Psi)$ is the amplitude of the ratio, and Δ is the phase shift of the p - and s -polarized components after reflection. The values of Ψ and Δ are extracted from the ratio, and are often presented as the experimental data [175].

To extract thickness and optical constants from Ψ and Δ , a model analysis needs to be performed. The sample is modelled with a stack of layers of corresponding materials, with their approximate thicknesses, and a regression analysis is performed to find parameters that provide the best fit to the experimental data. Dielectric functions of layers are represented either with tabulated data (taken from some source) or modelled with dispersion relations appropriate for a given material type. As discussed in Section 4.1, Lorentz oscillators are suitable for regions with absorption, and Drude oscillators are employed to describe free-electron behaviour in metals. A number of dispersion relation models based on these basic oscillators have been developed; one example is Cody-Lorentz oscillator, which is used in this work for analysing a -Si:H films. This function was developed for amorphous semiconductors and in particular for a -Si:H [177]. It represents the dielectric function with a Lorentz oscillator for energies exceeding the band gap, and an Urbach exponential tail for energies lower than the band gap [177]. The Urbach tail accounts for absorption by defect states present within the band gap of a -Si:H, as discussed in Section 3.2.2. TiO_2 layers in Paper 2 were also modelled with a Cody-Lorentz oscillator, with the peak energy in the UV, where the TiO_2 absorbs light. A Tauc-Lorentz oscillator, similar to the Cody-Lorentz one, was used in combination with the Drude model to represent the optical properties of the Al reflector employed in Paper 2.

7.2.5. Scanning Electron Microscopy

Scanning electron microscopy (SEM) is a widely used technique to study surface topography and composition. In SEM, the sample is bombarded with an electron beam, and various signals are detected. The most commonly used signals include electrons emitted from the material upon bombardment (*secondary electrons*), electrons from the incident beam that are scattered back by the sample (*backscattered electrons*), and *x-rays* generated in the sample [178]. The regions from which these signals can be detected are schematically illustrated in Figure 7.6A.

The energy spectrum of electrons emitted from the sample that is bombarded with a monochromatic electron beam is schematically shown in Figure 7.6C [179]. Backscattered electrons may have about the same energy as the incident beam or lose some energy as a result of inelastic scattering within the sample. Region 1 in Figure 7.6C corresponds to backscattered electrons that have energy of $> 50\%$ of the incoming beam energy, and the broad low intensity spectrum of region 2 in Figure 7.6C represents the electrons which travelled deeper into the sample and lost most of their energy before being scattered back [179]. The number of backscattered electrons for a given primary beam intensity is linearly proportional to the atomic number of the material, and therefore the backscattered electrons provide information about the composition of the sample [179].

Secondary electrons are emitted from the sample material upon ionization of the sample atoms by the primary beam, and have lower energies than the backscattered electrons, typically $< 10\text{eV}$ (region 3 in Figure 7.6C) [179]. Because of their low energies, where the electron mean free path is very short, secondary electrons can

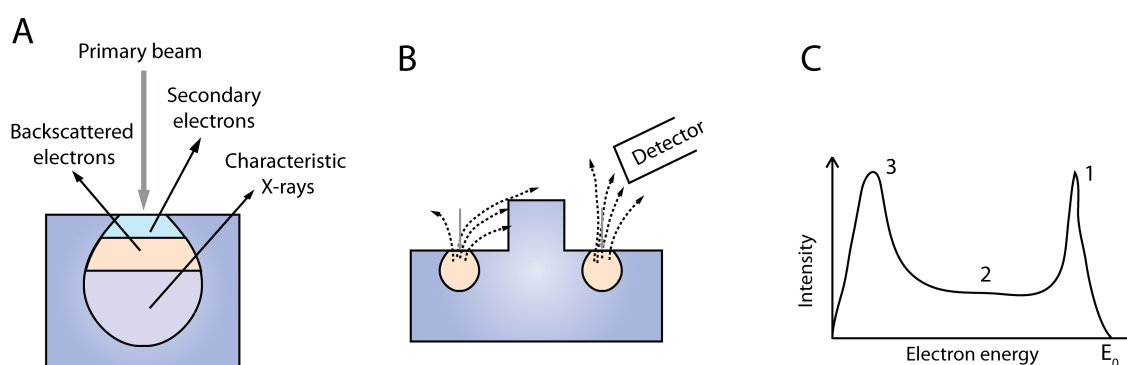


Figure 7.6. (A) Signals emitted from a sample bombarded with a (primary) electron beam (redrawn from [178]). (B) Effect of the surface topography and position of the detector in formation of images with secondary electrons (redrawn from [178]). (C) Energy spectrum of electrons emitted from a sample in SEM, for a primary beam energy E_0 (redrawn from [179]).

only travel a few nm in the material before being recaptured, and therefore those that are detected originate from a close distance from the surface (approximately 1 nm for metals and up to 20 nm for insulator) [179]. Not all emitted secondary electrons reach the detector; this depends on the angle between the surface of interest and the detector (see Figure 7.6B). Surface areas, from which the electrons do not reach the detector, will appear dark on the image, and thus SE images provide topographic information. This allows for relatively easy interpretation of SEM images, because they often look like ‘optical’ images (however, misinterpretations are also possible due to special imaging artefacts not discussed here). Examples of secondary electron SEM images of nanodiscs are shown in Figure 7.2B and C.

Characteristic X-rays are emitted when electrons of the primary beam displace an electron from the inner energy level of the specimen atom, and an electron from a higher energy level makes a transition to the vacancy, emitting the excess energy as an X-ray photon. X-rays generated in this way have material-specific energies, and therefore provide information about the composition.

7.2.6. Quartz crystal microbalance with dissipation monitoring (QCM-D)

The quartz crystal microbalance (QCM) technique is based on the fact that the frequency of an oscillator depends on its mass, which allows detecting and quantifying changes in the mass. In a common implementation, resonant oscillations are excited in a piezoelectric quartz crystal, usually in a shear mode. When a mass is added on top of the oscillating crystal, its resonant frequency shifts. Since very small changes in frequency can be routinely detected, the technique has a high sensitivity of $< 1 \text{ ng/cm}^2$ [180]. This allows using the QCM in particular to quantify the thickness of a growing film in thin-film vacuum deposition processes, like evaporation or sputtering. In this case, the mass added onto the crystal is linearly related to the resulting frequency shift, according to the Sauerbrey equation:

$$\Delta m = -C\Delta f, \quad (7.2)$$

where C is a constant that depends on the intrinsic properties of quartz and the thickness of the slab [180].

The QCM method was traditionally used in vacuum and in gaseous environments, but in the 1980s it was suggested as a measuring tool for applications in liquids [181]. The frequency shifts in this case may originate not only from an added mass, but also depend on the viscosity and density of the liquid. Rodahl *et al.* [180] further extended the applicability of the QCM technique by suggesting an instrument capable of measuring the oscillation frequency as well as the dissipation (or damping) factor of the quartz oscillator. The dissipation factor is a measure of how fast the oscillations decay after the driving force has been switched off; it is inversely proportional to the

quality factor (Q-factor). The dissipation characteristics depend on the viscosity of the liquid, and also on the viscoelastic properties of the adsorbed layer. In case the latter is not a thin and rigid film, but instead a structure, the parts of which can move relative to each other upon shear motion (for example, a large biomolecule), then the energy of the quartz oscillation will be dissipated due to this latter motion. The dissipation characteristics can thus provide information about the adsorbed film structure and elastic and/or viscoelastic properties. The technique implementing this approach is called quartz crystal microbalance with dissipation monitoring (QCM-D) and it has been used to study adsorption and desorption processes for a broad range of objects, including bacteria, viruses, eukaryotic cells, lipids, proteins, peptides, nucleotides and various small molecules of biological relevance [182], and also polymer films. It has also been applied simultaneously with the LSPR sensing technique, in a combined setup [77].

A schematic picture of a QCM-D sensor is shown in Figure 7.7A. Au electrodes, used to apply voltage to the piezoelectric quartz crystal, are present on both sides of the quartz disc (in the image, only the upper electrode is visible). The Au can be coated with a thin film that provides needed functionality for the adsorption studies. Figure 7.7B illustrates a sample of the kind used in this thesis (Paper 4), where the functional coating is a TiO_2 film, onto which dye molecules can adsorb. The results of Paper 4 suggest that the formed dye layer can be considered as a rigid film without dissipation, to which the Sauerbrey equation (7.2) applies. This allows quantification of the mass of the dye monolayer and the surface area that the studied dye molecule occupies on TiO_2 .

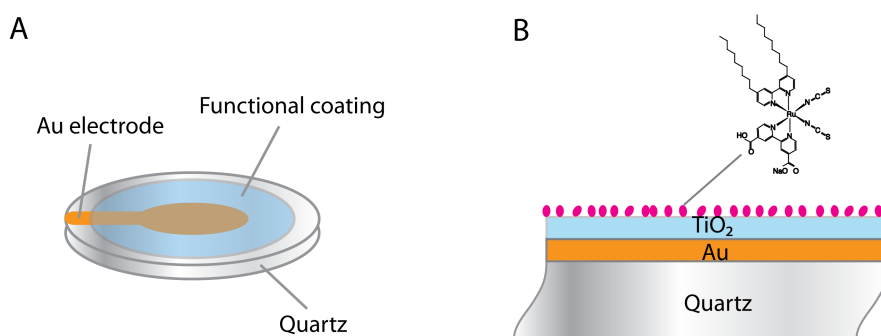


Figure 7.7. Schematics of (A) a QCM-d sensor and (B) a sample used in this thesis to study adsorption and desorption of dye molecules (pink ovals) on a TiO_2 thin film. The sensors oscillates in a shear mode.

8. Summary of results

In this thesis, use of the nanoparticle plasmon resonance was investigated for solar cell applications along two different research directions. The first one was enhancing light absorption in amorphous Si films using the near-field plasmonic effect, which could provide a possibility to reduce the absorber layer thickness and increase the efficiency of solar cells. This work resulted in Papers 1 and 2. The second line of investigation was studying adsorption and desorption of dye molecules on flat and porous TiO₂ films, and - for porous films – the diffusion process into the porous structure. These phenomena are in the present context particularly relevant for the dye-sensitized solar cell research, but also are of more generic interest for adsorption-diffusion processes, in particular, in mesoporous structures. The latter work is described in Papers 3-6. In this section, I summarize the approaches and findings in each article.

Paper 1

In paper 1, photoconductivity and optical measurements were used to quantify light absorption induced in a-Si:H films by the enhanced near-field around Ag plasmonic nanodiscs. The plasmon induced light absorption was studied as a function of the a-Si:H film thickness in the range from 9 to 67 nm. Up to a 3.2-fold enhancement of light absorption was demonstrated, which corresponds to a maximum of 15% of plasmon-induced absorptance at a single wavelength (that is, absorptance[†] from 22% to 37% at 500 nm) for a 9 nm a-Si:H film. This is a substantial enhancement in view of the fact that the maximal absorptance in such a system has a theoretical limit of 67% [183]. The experimental results were compared to computer simulations with the finite-element method, which accounted for the influence of the enhanced electric field around the plasmonic nanoparticles on light absorption in the a-Si:H films. The good agreement obtained between the experiments and the simulations suggests that the observed absorption enhancement originates from the plasmon enhanced near-field.

The simulations were also able to explain the origin of the plasmon resonance peaks (which led to the enhancement in light absorption by the a-Si:H) in the Ag nanodiscs, coated with the a-Si:H films. For the thinner films (< 50 nm), the resonance has a dipolar character. However, for the thicker films, an additional plasmon peak of

[†] Absorptance is defined as the fraction of the light that is absorbed; $A = 100 - T - S$, where A is absorptance, T is transmittance, S is scattering (all values are in %).

the Ag discs appeared, which was shown to correspond to a quadrupolar plasmonic resonance. Qualitatively, the quadrupolar resonance arises because for the thicker (> 50 nm) a-Si:H films, the wavelength of light in the high-refractive index material a-Si:H becomes comparable to the disc height (40 nm). This leads to the top and the bottom of the Ag nanodisc oscillating out of phase in this situation.

Based on these results, we proposed a novel ultrathin plasmonic a-Si:H solar cell design, which may be one of the first steps toward two-dimensional solar cells in the future. The absorbing layer thickness of as little as 20 nm can in an optically optimized solar cell provide substantial light absorption, which could lead to efficiencies of up to 18% for such a thin solar cell.

Paper 2

This study is an extension of the work done in Paper 1. Here we studied possibilities of further enhancing the absorption of light in a-Si:H thin films, by employing Ag nanostructures and a reflector-spacer structure. Since a-Si:H has a high refractive index, a coating of it on top of plasmonic nanoparticles significantly red-shifts the plasmon resonance. In order to keep the plasmon resonance in the visible range (a desirable wavelength is about 600 nm), we used nanostructures of high aspect ratios - Ag nanocones. Moreover, we used a metal reflector - dielectric spacer structure as a substrate for the Ag cones coated with an a-Si:H film, in order to additionally enhance the light intensity at the spatial position of the cones and the a-Si:H film. We measured experimentally and calculated numerically the absorptance of the Ag/a-Si:H nanocomposite on glass and on TiO₂ spacer - Al reflector structures with the spacer of varied thickness. We have also investigated reference systems, comprising flat film layers (without nanocones), and systems without the a-Si:H film. Reasonable agreement between the measurements and the calculations allowed extracting light absorptance of the individual layers, based on the calculations.

We observed that while the spacer thickness significantly influences the a-Si:H absorptance in the case of flat film systems, its effect in presence of the nanocones is substantially reduced. This can be qualitatively understood as the large cone height (> 200 nm in this work) effectively taking the role of the spacer, varying the distance between the Ag/a-Si:H nanocomposite and the reflector. This leads to phase shifts, experienced by the incident and reflected light waves, and influences the interference patterns. The highest value of the ideal photocurrent, estimated from the a-Si:H absorptance, was realized for Ag cone/a-Si:H nanocomposite on a 40 nm TiO₂ spacer/reflector structure. It was about 12.5 mA/cm², which is relatively high for a 20 nm thick a-Si:H film, considering that a confirmed record a-Si:H solar cell (about 300 nm thick) has a photocurrent of 16.7 mA/cm² [24].

While the presence of nanocones leads to plasmonic near-field effects, it also has geometrical effects that can enhance the a-Si:H absorption too. The latter include (i) increase in the amount of a-Si:H due to some of it depositing onto the side walls, and (ii) increased path of light through the film on the cone side walls. In order to distinguish between these geometrical effects and the plasmonic near-field effect, we performed calculations on the optimal system with a 40 nm TiO₂ spacer, where Ag cones were substituted with SiO₂ cones. The a-Si:H absorptance was higher in presence of the plasmonic cones compared to the dielectric ones.

While in this work we have focused on the a-Si:H absorptance for solar cell applications, using spacer-reflector structures in combination with plasmonic and semiconductor layers is a powerful means to alter absorption in the individual components. We comment briefly on the observed absorptance spectra for the specific layers in the different situations, which generally exhibit strong dependence on the parameters (spacer thickness, presence of the a-Si:H, etc.).

Paper 3

In paper 3, we demonstrated the possibility to monitor kinetics of adsorption of dye molecules on TiO₂ films by employing the indirect plasmon sensing (INPS) technique, which is of interest for dye-sensitized solar cell (DSC) research. The concept was first implemented on a model system that consisted of Au plasmonic sensor nanoparticles covered with a thin compact (non-porous) TiO₂ film. In this system, the enhanced plasmonic near-field senses any changes in the refractive index in the vicinity of the nanoparticles, *i.e.*, on the TiO₂ film surface (and a little above it), caused by adsorption of dye molecules. We monitored the plasmon resonance position in real time, during dye injection steps followed by rinsing with solvent. This revealed the kinetics of dye adsorption on the TiO₂ surface, and demonstrated that INPS/LSPR has good sensitivity for this type of measurements.

As the next step, we extended the INPS approach to a thick (10 μm) mesoporous TiO₂ film of the kind used in actual DSCs. For this experiment, we first estimated the plasmon sensing volume by mapping the dye adsorption-induced plasmon shift as a function of the flat film TiO₂ thickness (which determined the distance between the sensing LSPR particles and the adsorbed dye molecules). This resulted in an estimate that our plasmonic sensor is sensitive to the refractive index changes within *ca.* 50 nm from the Au nanoparticle surface, meaning a very local sensitivity. For the mesoporous TiO₂ film study, the plasmonic nanoparticles were placed at the interface between the TiO₂ film and the supporting substrate, mimicking the electron-collecting electrode of a DSC. In contrast to the quite fast response in the flat film measurements (about 20

s), the plasmon peak position for the porous sample exhibited a red-shift only after about 1 hour long dye adsorption. We compared this shift to the flat model system response, and attribute it to the process when the dye molecules reach the bottom of the porous TiO₂ film. We could also resolve the combined dye diffusion and adsorption kinetics at the bottom of the TiO₂ film.

This study demonstrated a means to locally sense the dye diffusion and adsorption kinetics in a mesoporous TiO₂ film, which in the context of DSCs can improve control over the dye adsorption process (immersion times, formation of an optimal monolayer, etc.). In a broader context, this technique (which we named Hidden Interface-Indirect Nanoplasmonic Spectroscopy, HI-INPS) provides possibilities to study diffusion of molecules in various porous frameworks.

Paper 5 below extended the measurements for mesoporous films in this paper, with much more detail. Paper 6 extended the measurements for the flat films. In both cases, many more dye concentrations were investigated.

Paper 4

In this work, we studied adsorption and desorption of dye molecules on flat TiO₂ films, similarly to the approach in Paper 3 (and Paper 6), but employing a different technique - Quartz Crystal Microbalance with Dissipation monitoring (QCM-D). This technique allows following the kinetics of adsorption and desorption in real time. We measured the mass uptake corresponding to an adsorbed dye (mono)layer, which translated into an area per adsorbed dye (Z907) molecule of 1.3 nm². This value was in a very good agreement with the one found by forcing the adsorbed dye molecules to desorb (after an adsorption run to saturation) and then measuring the fluorescence of the produced dye solution. Moreover, by combining the QCM-D and fluorescent measurements, we were able to quantify the ratio of dye of another type (Y123) and co-adsorbate (cheno) molecules, adsorbed simultaneously from a solution containing both molecule types.

We also measured the equilibrium uptake resulting from adsorbing dye from solutions of a number of different concentrations. The studied dye was Z907 in a 1:1 acetonitrile:tert-butanol mixture. From an adsorption isotherm, constructed based on these data and fitted with the Langmuir model, we obtained the value of the equilibrium adsorption constant of $5.1 \cdot 10^6 \text{ M}^{-1}$.

We have also performed preliminary QCM-D measurements for dye impregnation of a thick (2 μm) mesoporous TiO₂ film. There, the frequency shifts showed complex behaviour, which was likely caused not only by the mass uptake, but possibly also by a

change in fluid dynamics within the mesoporous TiO₂ as the adsorption was taking place. More investigations are needed in order to better understand this behaviour (such studies are being performed at EPFL by H. Harms in the M. Grätzel's group).

Paper 5

In this work (which is an extension of Paper 3, and focused on the mesoporous films), we studied diffusion of dye (Z907) molecules into mesoporous TiO₂ films similar to those used in dye-sensitized solar cells. This was realized by employing the HI-INPS technique, developed in Paper 3. We performed a series of experiments, where we studied the time it took for the dye molecules to reach the bottom (the percolation time) as a function of the TiO₂ film thickness and the dye solution concentration. The dependence of the percolation time on the latter parameters followed well the predictions of a diffusion-front model that we employed. Qualitatively, the essence of the diffusion-front model is that a boundary (the diffusion front) between a region in the TiO₂ film that is fully saturated with adsorbed dye, and a region that does not have any dye, is rather sharp and is moving in time, as the molecules diffuse deeper into the film. This behaviour arises since the dye molecules stick (adsorb) with a high probability to the TiO₂ surface and do not desorb fast, and because the mesoporous film has a very large surface area, *i.e.*, very many sites available for dye adsorption.

The very good agreement between the model and the measurements allowed us to extract the (effective) diffusion coefficient of the dye molecules in the porous TiO₂ network. The obtained value was 15 μm²/s. This is an order of magnitude smaller than the diffusion coefficient in the bulk solvent, which we attributed to the combined effects of an increased path length for the dye molecules in the complex porous network, and temporal weak trapping and subsequent release of diffusing molecules. Our diffusion-front model in its initial version assumed no desorption of dye molecules; this is a good approximation for our system, but it is not entirely correct. We therefore also extended the model allowing for desorption, and assumed a Langmuir kinetic behaviour. This enriched our analysis by providing an estimate of the dye coverage inside the mesoporous film, as a function of the dye solution concentration. The corresponding equilibrium adsorption constant predicted by our analysis is $8 \cdot 10^4 \text{ M}^{-1}$. This value agrees reasonably well with the value of $4 \cdot 10^4 \text{ M}^{-1}$ obtained by Fattori *et al.* [82] for the same system, and of $3 \cdot 10^4 \text{ M}^{-1}$ found by Fillinger *et al.* [83] for a similar dye.

One more interesting observation in this work was that the dye impregnation process occurs over two different timescales. The first, fast process lasts until the diffusion front reaches the bottom (approximately 20 min at a relatively high concentration of 0.1 mM). After that, a slow and long process (about 20 hours at the

same concentration) takes place until the film is fully saturated with dye. The dye loading after the first stage is 70-80% of the loading after the second process. We think that the latter long process may originate from dye molecules re-organizing on the TiO₂ surface, which leads to higher coverages. In this study, we focused on the first, short, process, and analysed it with the diffusion-front model. In literature, long (12 hours or longer) impregnation times are commonly used in fabrication of DSCs; both the fast and the slow processes occur during this time.

Paper 6

In this work, we used the INPS technique to study kinetics of dye adsorption and desorption on flat TiO₂ films, serving as model systems of mesoporous films used in DSCs. This study is an extension of our first work on this topic, which was reported in Paper 3. Here, we performed a detailed analysis of adsorption and desorption within the framework of the Langmuir kinetic model, using real time kinetic curves obtained at five different dye solution concentrations. This analysis allowed us extracting the adsorption and desorption rate constants, and calculating the equilibrium adsorption constant as their ratio. The latter value was in a good agreement with the one independently obtained from a Langmuir isotherm, where the equilibrium dye coverage (extracted from the values of the plasmon peak shift) was plotted as a function of the dye (Z907) solution concentration. The equilibrium adsorption constant, derived from the kinetic analysis, turned out to be $4.3 \cdot 10^6 \text{ M}^{-1}$, and the one derived from the isotherm analysis was $1.6 \cdot 10^6 \text{ M}^{-1}$. These values are in a reasonable agreement with the value of $5 \cdot 10^6 \text{ M}^{-1}$, found by QMC-D in Paper 4.

While the Langmuir model worked well in this study, there are also indications that its assumptions are not fully valid for our system. In Papers 3 and 4, we observed that the dye layer became more stable toward desorption after a longer adsorption time, in combination with an intermittent rinsing step. In Paper 5, saturation of the TiO₂ film with dye took a long time, despite the fact that the molecules reached the bottom of the film during much shorter times. These observations indicated possible rearrangements of dye molecules in the adsorbed layer. In this work, we took a closer look at the desorption process for cases, where the adsorption conditions (time and dye concentration) were varied. We performed a series of adsorption-desorption steps and observed less desorption after each subsequent rinsing step, which confirmed reorganization in the dye layer. Comparing desorption after adsorption that lasted for different times indicated that also the time factor (not only coverage) plays a role in the rearrangements in the dye film, longer adsorption times leading to more stable layers.

9. Outlook

9.1. Near-field plasmonic enhancement for a-Si:H solar cells

Papers 1 and 2 of this thesis have demonstrated a possibility to enhance light absorption in a-Si:H films by employing the enhanced electric near-field around Ag plasmonic nanostructures, discs and cones. In Paper 1, we also demonstrated an increased photoconductivity related to the improved light absorption, while Paper 2 only considered the optical properties of the Ag/a-Si:H nanocomposite. A natural continuation of these works is to incorporate plasmonic nanoparticles into an ultrathin a-Si:H solar cell. For this, high aspect ratio nanostructures would be needed, as discussed in Paper 2. A solar cell structure could be the following: glass – Al reflector (and contact) – TiO₂ (or another dielectric) spacer – Ag nanocones – a-Si:H film – a transparent conductive oxide (TCO).

Such a solar cell may have problems in the electrical performance, due to shunting (short-circuiting) occurring across the ultrathin a-Si:H film. The shunting may occur if the a-Si:H, deposited onto such high aspect ratio structures, has inhomogeneous thickness or pinholes, which is not improbable, especially since the film is very thin. However, Kuang *et al.* [153] recently demonstrated an a-Si:H solar cell, fabricated on 400 nm tall ZnO nanorods coated with a Ag film, where the a-Si:H absorber intrinsic layer was only 25 nm thick. This cell did not have a significantly worsened electrical performance compared to flat reference cells. In case the shunting problem does occur, a solution to it might be using the Ag nanostructures that are less sharp, and coating them with a thin dielectric film in order to keep the plasmon resonance in the visible. The dielectric coating would also reduce the probability of shunts occurring between the Ag structures and the TCO, where they are expected to be more problematic, compared to those occurring between the thin flat TiO₂ and the TCO.

Another important question is whether metal nanoparticles, embedded into a semiconductor film, will act as traps for generated electrons and/or holes. This could occur via injection of charge carriers from the semiconductor into the nanoparticle. In addition, deep trap states may appear in the semiconductor band gap in presence of metal atoms. The possible detrimental effect on the electrical performance of a solar cell in this case should be investigated. If the problem is present, a possible solution could be to introduce a thin dielectric layer in between the metal and the semiconductor.

The effect of introducing a thin dielectric spacer in between Ag nanostructures and a-Si:H layer should also be studied with respect to the optical performance. Since the

presence of a spacer decreases the near-field intensity in the adjacent a-Si:H film, one would expect less enhancement of light absorption in the latter. However, other effects may come into play, for example, the above-mentioned shift in the spectral position of the plasmon resonance due to the dielectric constant of the spacer being different (lower) than that of the a-Si:H. These effects should be looked into carefully, both by experiments and calculations. This question has been addressed by calculations for a solar cell material CuInSe₂ (CIS) [114], and it was shown that a spacer that is 4 nm thick decreases the integrated (and weighed with the solar spectrum) absorptance by only *ca.* 10%.

Another question that may be worth looking into is the effect of annealing the Ag plasmonic structures on the optical properties of the Ag/a-Si:H nanocomposite. We expect electron-electron scattering at the internal grain boundaries of Ag nanoparticles to reduce the intensity of the plasmon resonance, and annealing of Ag will reduce the number of these boundaries. In this case, the nanostructures should be coated with a dielectric spacer or, alternatively, with the a-Si:H film itself, prior to annealing, in order to avoid their reshaping.

Finally, in order to harvest a larger part of the solar spectrum, it may be beneficial to use nanoparticles with different spectral positions of the plasmon resonance. The easiest way to achieve this is by varying the particle size. Producing nanoparticles of several different diameters (but of the same height) should be straightforward with the hole-mask colloidal lithography process that we use.

9.2. Adsorption, desorption and diffusion of dye molecules on and in TiO₂ films

In Papers 3, 4 and 6, we have studied adsorption and desorption of dye molecules on compact TiO₂ surfaces, which were used as model systems of TiO₂ photoelectrodes employed in dye-sensitized solar cells (DSCs). One, perhaps not so exciting, but very important, next step could be to investigate the parameters of the adsorption and desorption processes as a function of different surface treatments and possible presence of contaminations. The motivation for this is that the reproducibility of the final solar cell performance is sometimes not very good between different research groups, but at times also even within the same laboratory. This could be related to variations in the mode of adsorption of dye molecules on the TiO₂ surface, which is the parameter essential for the photon harvesting and electron injection processes, and thus for the overall solar cell performance. Factors like surface cleaning, details of annealing of TiO₂ films, possibly presence of minute amounts of water (and/or other

impurities) in the used solvents etc. might all influence the adsorption process and chemical bond formation between the dye and the TiO₂. Following the adsorption and desorption kinetics with the INPS technique could help clarifying these issues, crucial for reproducible fabrication of DSCs. Of course, spectroscopic tools to identify the characteristics of the dye –TiO₂ bonds are also needed in parallel.

In Paper 5, we investigated diffusion of dye molecules into mesoporous TiO₂ films. As described in the summary of this paper, we have in particular observed that the dye molecules reached the bottom of the mesoporous TiO₂ films during a timescale that is much shorter than those typically used and reported for impregnating TiO₂ photoelectrodes for solar cells. Shortening the impregnation time is very important for the industrial fabrication of dye-sensitized solar cells. It would thus be interesting to understand the origin of the different timescales, to control them and to study the performance of solar cells, fabricated after impregnation during various times - in particular after the dye has percolated to the bottom, and after additional hours of impregnation.

While in this thesis we have used the indirect nanoplasmonic sensing scheme to study the dye-TiO₂ surface interactions, this approach can be applied to a broad variety of systems. Any field, where adsorption and desorption of molecules on surfaces is important, would benefit from the possibility to study the kinetics in real time and by relatively easy means. A particularly intriguing opportunity is the one of sensing locally inside a thick porous film, which was demonstrated in this work. Studying diffusion processes in porous films should be very relevant for porous materials used in for example catalysis, gas and liquid phase separation, drug release and gas sensing [184-186].

The sensor nanoparticles could in principle be placed not only at the bottom, but at any place inside a porous film. This, however, might not be straightforward if the particles are fabricated using the hole-mask colloidal lithography, as in this thesis. Testing this process on porous film could be another small, but important piece of work to do.

Finally, it would be very interesting to further investigate the complex frequency shifts observed in the initial QCM-D measurements on mesoporous TiO₂ films. Such a study could provide insights into viscoelastic properties of the TiO₂ networks, and also into the dye adsorption and diffusion processes. Furthermore, such phenomena are of more basic interest in the context of viscosity and flow in mesoporous structures.

9.3. Possible combinations of the two lines of research

The two research directions presented in this thesis have nanoplasmonics and solar cells as the common denominator, but otherwise they are quite different. Approaches and ideas from one of them could enrich the other one; here I discuss some possibilities.

One natural possibility would be to try to improve the performance of dye-sensitized solar cells using plasmonic resonance excitations. This has been already done in several works (for example, in references [126] and [139]). We could add to the existing approaches our ability to fabricate plasmonic nanostructures of a rather homogeneous size distribution, as well as the expertise we obtained after having worked with the Ag/a-Si:H system with the same aim.

Another interesting question is whether using the reflector-spacer structure (as those in Paper 2) in combination with sensing nanoparticles (as those used in Papers 3, 5 and 6) could improve the sensitivity for sensing applications. The reflector-spacer structure should have substantial effect on the sensing nanodiscs of the ‘typical’ geometry, *i.e.*, 20 nm high in our works, since their height is relatively low.

Finally, nanoplasmonic sensing might be used to answer some questions about a-Si:H films, in particular, to provide more insight into the Staebler-Wronski effect [38]. This effect is a light-induced degradation of the a-Si:H material, during which additional defects are created. This leads to a decrease in a-Si:H solar cell performances by about 20% over the first *ca.* 1000 hours of operation [37]. The Staebler-Wronski effect has been studied a lot, but is not yet fully understood; H atoms seem to play an important role in it. Possibly using a thin a-Si:H film as the sensing object in an INPS scheme, and exposing it to for example high temperatures or different gases (*e.g.*, H₂), could provide some insight into the Staebler-Wronski effect.

10. Acknowledgements

I am very grateful for having many good people around; here I would like to thank the ones that have made this thesis possible, by contributing in direct or indirect ways:

My supervisor Bengt Kasemo – thank you for taking me as a PhD student into your group, and for sharing your inspiring view on science. Thank you very much for the support, especially during the last years of my PhD, and for providing me with a nice combination of freedom and guidance.

My co-supervisor Carl Hägglund, for introducing me into the scientific life during the first years of my PhD, and for efficient work together despite the distance and the time difference over the next years! Thank you for your help and the thorough approach to our studies; I value this even more knowing how busy you have been.

My co-supervisor Christoph Langhammer, for your support, for being always available for discussions, and for sharing the very constructive, positive and enthusiastic attitude toward doing science.

Igor Zoric, for being so friendly and supportive toward all of us, for the nice and insightful discussions about the plasmon physics, and for being always available for answering questions.

Leo-Philipp Heiniger, for fabricating the films, providing the dye powders, and for the interesting discussions in e-mails and over phone.

Vladimir Zhdanov, Hauke Harms, and Michael Grätzel, for the fruitful collaboration. Emmanuel Nkurunziza, for the enthusiastic and hard work during the master project, which led to the good results.

Cleanroom experts: Mats Hagberg, for helping with a-Si:H film deposition, Örjan Arthursson, for the help with ellipsometry, Henrik Frederiksen, for advice on various deposition tools – and all three for contributing to the good atmosphere in the cleanroom!

Henrik Grönbeck, for being so friendly and very helpful with the organizational issues.

Carl W, for being such a great officemate! My dear friends Gülis, Deborah, and Masha for your love and care, and for all the nice moments! The whole Chemical physics group - such a diverse collection of good people; especially to Kristina, Carl W,

Adriana, Anna, and to former group members Markus, Elin, Raja, Nicola, Hans, and Michael Z. Natalia, Maxime, Adriana, Gülis, Debbie, and Fernando, for the sunny lunches together.

My great teachers outside of science: Eva M and Ann S, for opening a whole beautiful world of flamenco to me; Kitty S, for the great yoga classes, and for teaching us to appreciate every moment. My flamenco friends Lisbeth and Barbro, for the nice moments together. Alar, for your care and support, and for the very many very good times together!

P. I Golod, my professor in Kyiv, for sharing his unique enthusiasm about science, and for establishing the great atmosphere in the division.

My parents and my sister, and my friends in Ukraine, for their love and care.

Finally, I would like to acknowledge the Swedish Energy Agency, contract 0189-1, Nanoscience and Nanotechnology for Sustainable Energy and Environment (NANO-SEE), and Formas project 229-2009-772, for the financial support. The Myfab research infrastructure for micro- and nanofabrication is also gratefully acknowledged; the cleanroom is a great place!

11. References

1. Sveriges energisituation i ett europeiskt och globalt perspektiv. Report from The Energy Committee at the Royal Swedish Academy of Sciences. Accessed at www.kva.se/sv/Vetenskap-i-samhallet/Energi/ on Nov 1, 2013. (2013)
2. Würfel, P. *Physics of solar cells*. 2nd ed. Weinheim: Wiley-VCH, 2009.- 244 p.
3. *Europe Unconventional Gas*, www.europeunconventionalgas.org/. (Visited on December 22nd, 2013)
4. *Earth's CO₂ home page*, <http://co2now.org/>. (Visited on October 30, 2013)
5. *Energy resources and their utilization in a 40-year perspective up to 2050*. Report from The Energy Committee at the Royal Swedish Academy of Sciences. Accessed from <http://kva.se/sv/Vetenskap-i-samhallet/Energi/>. (2010)
6. Smalley, R. E. *Future global energy prosperity: the Terawatt challenge* MRS Bulletin, 30, 412-417 (2005)
7. *Global market outlook for photovoltaics 2013-2017*. Report from European Photovoltaic Industry Association (EPIA). Accessed at www.epia.org/news/publications/ on Nov 1, 2013. (2013)
8. *Connecting the Sun: Solar photovoltaics on the road to large-scale grid integration*. Report from European Photovoltaic Industry Association (EPIA). Accessed at www.epia.org/news/publications/ on Nov 1, 2013. (2012)
9. *Solar photovoltaics: Competing in the energy sector*. Report from European Photovoltaic Industry Association (EPIA). (2011)
10. Zweibel, K. *The Terawatt challenge for thin-film PV*. Report from National Renewable Energy Laboratory (NREL). (2005)
11. *PV Cycle*, www.pvcycle.org. (Visited on October 31, 2013)
12. *Statements on Solar energy: by the Energy Committee at the Royal Swedish Academy of Sciences*; accessed from <http://kva.se/sv/Vetenskap-i-samhallet/Energi/>. (2008)
13. Green, M. A. *Third generation photovoltaics: Ultra-high conversion efficiency at low cost*. *Progress in Photovoltaics: Research and Applications*, 9, 123-135 (2001)
14. Nelson, J. *The physics of solar cells*. London: Imperial College Press, 2003.- 363 p.
15. Sharp Solar module ND-250QCS. www.sharpsusa.com/SolarElectricity/SolarProducts/ResidentialSolarProducts.aspx. (visited on October 10, 2013)
16. Reference Solar Spectral Irradiance: Air Mass 1.5, <http://rredc.nrel.gov/solar/spectra/am1.5/>. (visited on October 10, 2013)
17. Persson, T. *Solar radiation climate in Sweden*. *Physics and Chemistry of the Earth, Part B*, 24(3), 275-279 (1999)
18. Neamen, D. A. *Semiconductor physics and devices: basic principles*. Boston: McGraw-Hill, 2003.- 746 p.
19. Fonash, S. J. *Solar cell device physics*. 2nd ed.: Elsevier, 2010.
20. Shockley, W. and Queisser, H. J. *Detailed balance limit of efficiency of p-n junction solar cells*. *Journal of Applied Physics*, 32(3), 510-519 (1961)
21. Janssen, R. A. J. and Nelson, J. *Factors limiting device efficiency in organic photovoltaics*. *Advanced Materials*, 25, 1847-1858 (2013)

22. Hirst, L. C. and Ekins-Daukes, N. J. *Fundamental losses in solar cells*. Progress in Photovoltaics: Research and Applications, 19, 286-293 (2010)
23. Polman, A. and Atwater, H. A. *Photonic design principles for ultrahigh-efficiency photovoltaics*. Nature Materials, 11, 174-177 (2012)
24. Green, M. A., Emery, K., Hishikawa, Y., Warta, W. and Dunlop, E. D. *Solar cell efficiency tables (Version 42)*. Progress in Photovoltaics: Research and Applications, 21, 827-837 (2013)
25. Kirk, A. P. and Fischetti, M. V. *Fundamental limitations of hot-carrier solar cells*. Physical Review B, 86, 165206 (2012)
26. Kosten, E. D., Atwater, J. H., Parsons, J., Polman, A. and Atwater, H. A. *Highly efficient GaAs solar cells by limiting light emission angle*. Light: Science and Applications, 2, e45 (2013)
27. Green, M. A. *Crystalline and thin-film silicon solar cells: state of the art and future potential*. Solar Energy, 74, 181-192 (2003)
28. Campbell, P. and Green, M. A. *Light trapping properties of pyramidally textured surfaces*. Journal of Applied Physics, 62(1), 243-249 (1987)
29. Tiedje, T., Yablonovitch, E., Cody, G. D. and Brooks, B. *Limiting efficiency of silicon solar cells*. IEEE Transactions on Electron Devices, ED-31(5), 711-716 (1984)
30. Zhao, J., Wang, A. and Green, M. A. *19.8% efficient 'honeycomb' textured multicrystalline and 24.4% monocrystalline silicon solar cells*. Applied Physics Letters, 73(14), 1991-1993 (1998)
31. Zweibel, K. *Thin film PV manufacturing: Materials costs and their optimization*. Solar Energy Materials & Solar Cells, 63, 375-386 (2000)
32. Aberle, A. G. *Thin-film solar cells*. Thin Solid Films, 517, 4706-4710 (2009)
33. Chirila, A., Bloesch, P., Seyrling, S., Uhl, A., Buecheler, S., Pianezzi, F., Fella, C., Perrenoud, J., Kranz, L., Verma, R., Guettler, D., Nishiwaki, S., Romanyuk, Y. E., Bilger, G., Bremaud, D. and Tiwari, A. N. *Cu(In,Ga)Se₂ solar cell grown on flexible polymer substrate with efficiency exceeding 17%*. Progress in Photovoltaics: Research and Applications, 19, 560-564 (2011)
34. Takahashi, K. and Konagai, M. *Amorphous silicon solar cells*. London: North Oxford Academic Publishers, 1986.- 225 p.
35. Carlson, D. E. and Wronski, C. R. *Amorphous silicon solar cells* / In *Solar cells: materials, manufacture and operation*, ed. by T. Markvart and L. Castaner. Oxford: Elsevier Advanced Technology, 2005.- pp. 217-251.
36. Cuevas, A. and Sinton, R. A. *Characterisation and diagnosis of silicon wafers and devices* / In *Solar cells: materials, manufacture and operation*, ed. by T. Markvart and L. Castaner. Oxford: Elsevier Advanced Technology, 2005.- pp. 163-188.
37. Shah, A. V., Schade, H., Vanecek, M., Meier, J., Vallat-Sauvain, E., Wyrsh, N., Kroll, U., Droz, C. and Bailat, J. *Thin-film Silicon solar cell technology*. Progress in Photovoltaics: Research and Applications, 12, 113-142 (2004)
38. Shimizu, T. *Staebler-Wronski effect in hydrogenated amorphous silicon and related alloy films*. Japanese Journal of Applied Physics, 43(6A), 3257-3268 (2004)
39. Hänni, S., Bugnon, G., Parascandolo, G., Boccard, M., Escarre, J., Despeisse, M., Meillaud, F. and Ballif, C. *High-efficiency microcrystalline silicon single-junction solar cells*. Progress in Photovoltaics: Research and Applications, 21, 821-826 (2013)
40. Spanggaard, H. and Krebs, F. C. *A brief history of the development of organic and polymeric photovoltaics*. Solar Energy Materials & Solar Cells, 83, 125-146 (2004)

41. Weickert, J., Dunbar, R. B., Hesse, H. C., Wiedemann, W. and Schmidt-Mende, L. *Nanostructured organic and hybrid solar cells*. *Advanced Materials*, 23(1810-1828) (2011)
42. Jorgensen, M., Norrman, K. and Krebs, F. C. *Stability / degradation of polymer solar cells*. *Solar Energy Materials & Solar Cells*, 92, 686-714 (2008)
43. Tanenbaum, D. M., Hermenau, M., Voroshazi, E., Lloyd, M. T., Galagan, Y., Zimmermann, B., Hösel, M., Dam, H. F., Jorgensen, M., Gevorgyan, S. A., Kudret, S., Maes, W., Lutsen, L., Vanderzande, D., Würfel, U., Andriessen, R., Rösch, R., Hoppe, H., Teran-Escobar, G., Lira-Cantu, M., Rivaton, A., Uzunoglu, G. Y., Germack, D., Andreasen, B., Madsen, M. V., Norrman, K. and Krebs, F. C. *The ISOS-3 inter-laboratory collaboration focused on the stability of a variety of organic photovoltaic devices*. *RSC Advances*, 2, 882-893 (2012)
44. Grätzel, M. *Dye-sensitized solar cells*. *Journal of Photochemistry and Photobiology C: Photochemistry Reviews*, 4, 145-153 (2003)
45. Zhang, Q. and Cao, G. *Nanostructured photoelectrodes for dye-sensitized solar cells*. *Nano Today*, 6, 91-109 (2011)
46. Nazeeruddin, M. K., Baranoff, E. and Grätzel, M. *Dye-sensitized solar cells: a brief overview*. *Solar Energy*, 85, 1172-1178 (2011)
47. Harikisun, R. and Desilvestro, H. *Long-term stability of dye solar cells*. *Solar Energy*, 85, 1179-1188 (2010)
48. Toivola, M., Halme, J., Miettunen, K., Aitola, K. and Lund, P. D. *Nanostructured dye solar cells on flexible substrates - review*. *International Journal of Energy Research*, 33, 1145-1160 (2009)
49. Wang, B. and Kerr, L. L. *Dye sensitized solar cells on paper substrates*. *Solar Energy Materials & Solar Cells*, 95, 2531-2535 (2011)
50. Wild-Scholten, M. J. d. and Veltkamp, A. C. *Environmental life cycle analysis of dye sensitized solar devices; status and outlook*. In 22nd European Photovoltaic Solar Energy Conference and Exhibition, Milan, Italy, 3-7 september 2007. (2007)
51. Grätzel, M. *Recent advances in sensitized mesoscopic solar cells*. *Accounts of Chemical Research*, 42, 1788-1798 (2009)
52. Hardin, B. E., Snaith, H. J. and McGehee, M. D. *The renaissance of dye-sensitized solar cells*. *Nature Photonics*, 6, 162-169 (2012)
53. Jun, H. K., Careem, M. A. and Arof, A. K. *Quantum dot-sensitized solar cells - perspective and recent developments: A review of Cd chalcogenide quantum dots as sensitizers*. *Renewable and Sustainable Energy Reviews*, 22, 148-167 (2013)
54. Burschka, J., Pellet, N., Moon, S.-J., Humphry-Baker, R., Gao, P., Nazeeruddin, M. K. and Grätzel, M. *Sequential deposition as a route to high-performance perovskite-sensitized solar cells*. *Nature*, 499, 316-320 (2013)
55. Kojima, A., Teshima, K., Shirai, Y. and Miyasaka, T. *Organometal halide perovskites as visible-light sensitizers for photovoltaic cells*. *Journal of American Chemical Society*, 131, 6050-6051 (2009)
56. Lee, M. M., Teuscher, J., Miyasaka, T., Murakami, T. N. and Snaith, H. J. *Efficient hybrid solar cells based on meso-superstructured organometal halide perovskites*. *Science*, 338, 643-647 (2012)
57. Liu, M., Johnston, M. B. and Snaith, H. J. *Efficient planar heterojunction perovskite solar cells by vapour deposition*. *Nature*, 501, 395-398 (2013)

58. Park, N.-G. *Organometal perovskite light absorbers toward a 20% efficiency low-cost solid-state mesoscopic solar cell*. *The Journal of Physical Chemistry Letters*, 4, 2423-2429 (2013)
59. Bohren, C. F. and Huffman, D. R. *Absorption and scattering of light by small particles*. New York: Wiley, 1998.- 530 p.
60. Maier, S. A. *Plasmonics: fundamentals and applications*. New York: Springer, 2007.- 223 p.
61. Ordal, M. A., Long, L. L., Bell, R. J., Bell, S. E., Bell, R. R., Alexander, R. W., Jr. and Ward, C. A. *Optical properties of the metals Al, Co, Cu, Au, Fe, Pb, Ni, Pd, Pt, Ag, Ti, and W in the infrared and far infrared*. *Applied Optics*, 22, 1099-1120 (1983)
62. Johnson, P. B. and Christy, R. W. *Optical constants of the noble metals*. *Physical Review B*, 6, 4370-4379 (1972)
63. Townsend, E. and Bryant, G. W. *Plasmonic properties of metallic nanoparticles: the effects of size quantization*. *Nano Letters*, 12, 429-434 (2011)
64. Zoric, I., Zäch, M., Kasemo, B. and Langhammer, C. *Gold, Platinum, and Aluminum nanodisk plasmons: material independence, subradiance, and damping mechanisms*. *ACS Nano*, 5(4), 2535-2546 (2011)
65. Dahmen, C. and von Plessen, G. *Optical effects of metallic nanoparticles*. *Australian Journal of Chemistry*, 60, 447-456 (2007)
66. Mayer, K. M. and Hafner, J. H. *Localized surface plasmon resonance sensors*. *Chemical Reviews*, 111, 3828-3857 (2011)
67. Sepulveda, B., Angelome, P. C., Lechuga, L. M. and Liz-Marzan, L. M. *LSPR-based nanobiosensors*. *Nano Today*, 4, 244-251 (2009)
68. Larsson, E. M., Syrenova, S. and Langhammer, C. *Nanoplasmonic sensing for nanomaterials science*. *Nanophotonics*, 1, 249-266 (2012)
69. Hayashi, S. and Okamoto, T. *Plasmonics: visit the past to know the future*. *Journal of Physics D: Applied Physics*, 45, 433001 (2012)
70. Jensen, T., Kelly, L., Lazarides, A. and Schatz, G. C. *Electrodynamics of noble metal nanoparticles and nanoparticle clusters*. *Journal of Cluster Science*, 10(2), 295-317 (1999)
71. Giannini, V., Fernandez-Dominguez, A. I., Heck, S. C. and Maier, S. A. *Plasmonic nanoantennas: fundamentals and their use in controlling the radiative properties of nanoemitters*. *Chemical Reviews*, 111, 3888-3912 (2011)
72. Halas, N. J., Lal, S., Chang, W.-S., Link, S. and Nordlander, P. *Plasmons in strongly coupled metallic nanostructures*. *Chemical Reviews*, 111, 3913-3961 (2011)
73. Stewart, M. E., Anderton, C. R., Thompson, L. B., Maria, J., Gray, S. K., Rogers, J. A. and Nuzzo, R. G. *Nanostructured plasmonic sensors*. *Chemical Reviews*, 108, 494-521 (2008)
74. Müller, M., Jung, U., Gusak, V., Ulrich, S., Holz, M., Herges, R., Langhammer, C. and Magnussen, O. *Localized surface plasmon resonance investigations of photoswitching in azobenzene-functionalized self-assembled monolayers on Au*. *Langmuir*, 29, 10693-10699 (2013)
75. Langhammer, C., Larsson, E. M., Kasemo, B. and Zoric, I. *Indirect nanoplasmonic sensing: ultrasensitive experimental platform for nanomaterials science and optical nanocalorimetry*. *Nano Letters*, 10, 3529-3538 (2010)
76. Langhammer, C., Zhdanov, V. P., Zoric, I. and Kasemo, B. *Size-dependent kinetics of hydriding and dehydriding of Pd nanoparticles*. *Physical Review Letters*, 104, 135502 (2010)

77. Larsson, E. M., Edvardsson, M. E. M., Langhammer, C., Zoric, I. and Kasemo, B. A combined nanoplasmonic and electrodeless quartz crystal microbalance setup. *Review of Scientific Instruments*, 80, 125105 (2009)
78. Masel, R. I. *Principles of adsorption and reaction on solid surfaces*. New York; Chichester; Brisbane; Toronto; Singapore: John Wiley & Sons, Inc., 1996.- 804 p.
79. O'Regan, B., Xiaoe, L. and Ghaddar, T. Dye adsorption, desorption and distribution in mesoporous TiO₂ films, and its effects on recombination losses in dye sensitized solar cells. *Energy & Environmental Science*, 5, 7203-7215 (2012)
80. Martsinovich, N., Ambrosio, F. and Troisi, A. Adsorption and electron injection of the N₃ metal-organic dye on the TiO₂ rutile (110) surface. *Physical Chemistry Chemical Physics*, 14, 16668-16676 (2012)
81. Bazzan, G., Deneault, J. R., Kang, T.-S., Taylor, B. E. and Durstock, M. F. Nanoparticle/dye interface optimization in dye-sensitized solar cells. *Advanced Functional Materials*, 21(17), 3268-3274 (2011)
82. Fattori, A., Peter, L. M., McCall, K. L., Robertson, N. and Marken, F. Adsorption and redox chemistry of cis-RuLL'(SCN)₂ with L=4,4'-dicarboxylic acid-2,2'-bipyridine and L'=4,4'-dinonyl-2,2'-bipyridine (Z907) at FTO and TiO₂ electrode surfaces. *Journal of Solid State Electrochemistry*, 14(10), 1929-1936 (2010)
83. Fillinger, A. and Parkinson, B. A. The adsorption behavior of a Ruthenium-based sensitizing dye to nanocrystalline TiO₂: Coverage effects on the external and internal sensitization quantum yields. *Journal of the Electrochemical Society*, 146, 4559-4564 (1999)
84. Griffith, M. J., James, M., Triani, G., Wagner, P., Wallace, G. G. and Officer, D. L. Determining the orientation and molecular packing of organic dyes on a TiO₂ surface using X-ray reflectometry. *Langmuir*, 27(12944-12950) (2011)
85. Lee, C.-R., Kim, H.-S., Jang, I.-H., Im, J.-H. and Park, N.-G. Pseudo first-order adsorption kinetics of N719 dye on TiO₂ surface. *ACS Applied Materials & Interfaces*, 3(6), 1953-1957 (2011)
86. Lu, Y., Choi, D.-j., Nelson, J., Yang, O.-B. and Parkinson, B. A. Adsorption, desorption and sensitization of low-index anatase and rutile surfaces by the Ruthenium complex dye N₃. *Journal of the Electrochemical Society*, 153, E131-E137 (2006)
87. Neale, N. R., Kopidakis, N., van de Lagemaat, J., Gratzel, M. and Frank, A. J. Effect of a coadsorbent on the performance of dye-sensitized TiO₂ solar cells: Shielding versus band-edge movement. *Journal of Physical Chemistry B*, 109(49), 23183-23189 (2005)
88. Park, H., Bae, E., Lee, J.-J., Park, J. and Choi, W. Effect of the anchoring group in Ru-Bipyridyl sensitizers on the photoelectrochemical behavior of dye-sensitized TiO₂ electrodes: carboxylate versus phosphonate linkages. *Journal of Physical Chemistry B*, 110, 8740-8749 (2006)
89. Shklover, V., Nazeeruddin, K., Gratzel, M. and Ovchinnikov, Y. E. Packing of ruthenium sensitizer molecules on mostly exposed faces of nanocrystalline TiO₂: crystal structure of (NBu₄)₂[Ru(H₂tctterpy)(NCS)₃](2-)_{0.5} DMSO. *Applied Organometallic Chemistry*, 2002(11), 635-642 (2002)
90. Ushiroda, S., Ruzycki, N., Lu, Y., Spitler, M. T. and Parkinson, B. A. Dye sensitization of the anatase (101) crystal surface by a series of dicarboxylated thiocyanine dyes. *Journal of American Chemical Society*, 127, 5158-5168 (2004)

91. Zuleta, M., Edvinsson, T., Yu, S., Ahmadi, S., Boschloo, G., Göthelid, M. and Hagfeldt, A. *Light-induced rearrangements of chemisorbed dyes on anatase (101)*. *Physical Chemistry Chemical Physics*, 14, 10780-10788 (2012)
92. Katoh, R., Yaguchi, K., Murai, M., Watanabe, S. and Furube, A. *Differences in adsorption behavior of N3 dye on flat and nanoporous TiO₂ surfaces*. *Chemical Physics Letters*, 497, 48-51 (2010)
93. Peic, A., Staff, D., Risbridger, T., Menges, B., Peter, L. M., Walker, A. B. and Cameron, P. J. *Real-time optical waveguide measurements of dye adsorption into nanocrystalline TiO₂ films with relevance to dye-sensitized solar cells*. *Journal of Physical Chemistry C*, 115(3), 613-619 (2011)
94. Spitler, M. T. and Parkinson, B. A. *Dye sensitization of single crystal semiconductor electrodes*. *Accounts of Chemical Research*, 42, 2017-2029 (2009)
95. Jo, Y., Jung, C.-I., Lim, J., Kim, B. H., Han, C.-H., Kim, J., Kim, S., Kim, D. and Jun, Y. *A novel dye coating method for N719 dye-sensitized solar cells*. *Electrochimica Acta*, 66, 121-125 (2012)
96. Concina, I., Frison, E., Braga, A., Silvestrini, S., Maggini, M., Sberveglieri, G., Vomiero, A. and Carofiglio, T. *On-line monitoring and active control of dye uptake in dye-sensitized solar cells*. *Chemical Communications*, 47(42), 11656-11658 (2011)
97. Kantonis, G., Stergiopoulos, T., Katsoulidis, A. P., Pomonis, P. J. and Falaras, P. *Electron dynamics dependence on optimum dye loading for an efficient dye-sensitized solar cell*. *Journal of Photochemistry and Photobiology A - Chemistry*, 217(1), 236-241 (2011)
98. Wang, Z. S., Yanagida, M., Sayama, K. and Sugihara, H. *Electronic-insulating coating of CaCO₃ on TiO₂ electrode in dye-sensitized solar cells: Improvement of electron lifetime and efficiency*. *Chemistry of Materials*, 18(12), 2912-2916 (2006)
99. Wen, P., Xue, M., Ishikawa, Y., Itoh, H. and Feng, Q. *Relationships between cell parameters of dye-sensitized solar cells and dye-adsorption parameters* *ACS Applied Materials & Interfaces*, 4(4), 1928-1934 (2012)
100. Kim, J.-K., Seo, H., Son, M.-K., Shin, I., Hong, J. and Kim, H.-J. *The analysis of the change in the performance and impedance of dye-sensitized solar cell according to the dye-adsorption time*. *Current Applied Physics*, 10(3), S418-S421 (2010)
101. Katoh, R., Fuke, N., Furube, A. and Koide, N. *Effect of dye coverage on photo-induced electron injection efficiency in N719-sensitized nanocrystalline TiO₂ films*. *Chemical Physics Letters*, 489(4-6), 202-206 (2010)
102. Watson, T., Holliman, P. and Worsley, D. *Rapid, continuous in situ monitoring of dye sensitisation in dye-sensitized solar cells*. *Journal of Materials Chemistry*, 21(12), 4321-4325 (2011)
103. Holliman, P. J., Davies, M. L., Connell, A., Velasco, B. V. and Watson, T. M. *Ultra-fast dye sensitisation and co-sensitisation for dye sensitized solar cells*. *Chemical Communications*, 46(38), 7256-7258 (2010)
104. Lesne, A. and Lagues, M. *Scale invariance: from phase transitions to turbulence*. Berlin; Heidelberg: Springer-Verlag, 2012.- 397 p.
105. Deen, W. M. *Hindered transport of large molecules in liquid-filled pores*. *AIChE Journal*, 33, 1409-1425 (1987)
106. Sahimi, M. and Jue, V. L. *Diffusion of large molecules in porous media*. *Physical Review Letters*, 62, 629-632 (1989)

107. Dürr, M., Schmid, A., Obermaier, M., Yasuda, A. and Nelles, G. *Diffusion properties of dye molecules in nanoporous TiO₂ networks*. Journal of Physical Chemistry A, 109, 3967-3970 (2005)
108. Dürr, M., Obermaier, M., Yasuda, A. and Nelles, G. *Adsorption-/desorption-limited diffusion of porphyrin molecules in nano-porous TiO₂ networks*. Chemical Physics Letters, 467, 358-360 (2009)
109. Bartlett, P. N. and Gardner, J. W. *Diffusion and binding of molecules to sites within homogeneous thin films*. Philosophical Transactions of the Royal Society of London Series A - Mathematical, Physical and Engineering Sciences, 354(1704), 35-57 (1996)
110. Atwater, H. A. and Polman, A. *Plasmonics for improved photovoltaic devices*. Nature Materials, 9, 205-213 (2010)
111. Pala, R. A., White, J., Barnard, E., Liu, J. and Brongersma, M. L. *Design of plasmonic thin-film solar cells with broadband absorption enhancements*. Advanced Materials, 21, 3504-3509 (2009)
112. Hägglund, C. and Apell, P. S. *Resource efficient plasmon-based 2D-photovoltaics with reflective support*. Optics Express, 18(103), A343-A356 (2010)
113. Hägglund, C. and Kasemo, B. *Nanoparticle plasmonics for 2D-photovoltaics: mechanisms, optimization and limits*. Optics Express, 17(14), 11944-11957 (2009)
114. Hägglund, C. and Apell, P. S. *Plasmonic near-field absorbers for ultrathin solar cells*. The Journal of Physical Chemistry Letters, 3, 1275-1285 (2012)
115. Moulin, E., Luo, P., Pieters, B., Sukmanowski, J., Kirchhoff, J., Reetz, W., Müller, T., Carius, R., Royer, F.-X. and Stiebig, H. *Photoresponse enhancement in the near infrared wavelength range of ultrathin amorphous silicon photosensitive devices by integration of silver nanoparticles*. Applied Physics Letters, 95, 033505 (2009)
116. Westphalen, M., Kreibig, U., Rostalski, J., Lüth, H. and Meissner, D. *Metal cluster enhanced organic solar cells*. Solar Energy Materials & Solar Cells, 61, 97-105 (2000)
117. White, T. P. and Catchpole, K. R. *Plasmon-enhanced internal photoemission for photovoltaics: Theoretical efficiency limits*. Applied Physics Letters, 101, 073905 (2012)
118. Green, M. A. and Pillai, S. *Harnessing plasmonics for solar cells*. Nature Photonics, 6, 130-132 (2012)
119. Zhdanov, V. P., Zoric, I. and Kasemo, B. *Plasmonics: Heat transfer between metal nanoparticles and supporting nanolayers*. Physica E, 46, 113-118 (2012)
120. Schaadt, D. M., Feng, B. and Yu, E. T. *Enhanced semiconductor optical absorption via surface plasmon excitation in metal nanoparticles*. Applied Physics Letters, 86, 063106 (2005)
121. Pillai, S., Catchpole, K. R., Trupke, T. and Green, M. A. *Surface plasmon enhanced silicon solar cells*. Journal of Applied Physics, 101, 093105 (2007)
122. Losurdo, M., Giangregorio, M. M., Bianco, G. V., Sacchetti, A., Capezzuto, P. and Bruno, G. *Enhanced absorption in Au nanoparticles / a-Si:H / c-Si heterojunction solar cells exploiting Au surface plasmon resonance*. Solar Energy Materials & Solar Cells, 93, 1749-1754 (2009)
123. Hägglund, C., Zäch, M., Petersson, G. and Kasemo, B. *Electromagnetic coupling of light into a silicon solar cell by nanodisk plasmons*. Applied Physics Letters, 92, 053110 (2008)
124. Matheu, P., Lim, S. H., Derkacs, D., McPheeters, C. and Yu, E. T. *Metal and dielectric nanoparticle scattering for improved optical absorption in photovoltaic devices*. Applied Physics Letters, 93, 113108 (2008)

125. Wan, D., Chen, H.-L., Tseng, T.-C., Fang, C.-Y., Lai, Y.-S. and Yeh, F.-Y. *Antireflective nanoparticle arrays enhance the efficiency of silicon solar cells*. *Advanced Functional Materials*, 20, 3064-3075 (2010)
126. Standridge, S. D., Schatz, G. C. and Hupp, J. T. *Distance dependence of plasmon-enhanced photocurrent in dye-sensitized solar cells*. *Journal of American Chemical Society*, 131, 8407-8409 (2009)
127. Akimov, Y. A., Ostrikov, K. and Li, E. P. *Surface plasmon enhancement of optical absorption in thin-film silicon solar cells*. *Plasmonics*, 4, 107-113 (2009)
128. Catchpole, K. R. and Polman, A. *Design principles for particle plasmon enhanced solar cells*. *Applied Physics Letters*, 93, 191113 (2008)
129. Pors, A., Uskov, A. V., Willatzen, M. and Protsenko, I. E. *Control of the input efficiency of photons into solar cells with plasmonic nanoparticles*. *Optics Communications*, 284, 2226-2229 (2011)
130. Beck, F. J., Mokkalapati, S. and Catchpole, K. R. *Plasmonic light-trapping for Si solar cells using self-assembled Ag nanoparticles*. *Progress in Photovoltaics: Research and Applications*, 18, 500-504 (2010)
131. Munday, J. N. and Atwater, H. A. *Large integrated absorption enhancement in plasmonic solar cells by combining metallic gratings and antireflection coatings*. *Nano Letters*, 11, 2195-2201 (2011)
132. Nakayama, K., Tanabe, K. and Atwater, H. A. *Plasmonic nanoparticle enhanced light absorption in GaAs solar cells*. *Applied Physics Letters*, 93, 121904 (2008)
133. Hayashi, S., Kozaru, K. and Yamamoto, K. *Enhancement of photoelectric conversion efficiency by surface plasmon excitation: a test with an organic solar cell*. *Solid State Communications*, 79(9), 763-767 (1991)
134. Stenzel, O., Stendal, A., Voigtsberger, K. and von Borczyskowski, C. *Enhancement of the photovoltaic conversion efficiency of copper phthalocyanine thin film devices by incorporation of metal clusters*. *Solar Energy Materials & Solar Cells*, 37(337-348) (1995)
135. Duche, D., Torchio, P., Escoubas, L., Monestier, F., Simon, J.-J., Flory, F. and Mathian, G. *Improving light absorption in organic solar cells by plasmonic contribution*. *Solar Energy Materials & Solar Cells*, 93, 1377-1382 (2009)
136. Kulkarni, A., Noone, K. M., Munchika, K., Guyer, S. R. and Ginger, D. S. *Plasmon-enhanced charge carrier generation in organic photovoltaic films using silver nanoprisms*. *Nano Letters*, 10, 1501-1505 (2010)
137. Lal, N. N., Soares, B. F., Sinha, J. K., Huang, F., Mahajan, S., Bartlett, P. N., Greenham, N. C. and Baumberg, J. J. *Enhancing solar cells with localized plasmons in nanovoids*. *Optics Express*, 19(2), 11256-11263 (2011)
138. Wen, C., Ishikawa, K., Kishima, M. and Yamada, K. *Effects of silver particles on the photovoltaic properties of dye-sensitized TiO₂ thin films*. *Solar Energy Materials & Solar Cells*, 61, 339-351 (2000)
139. Sheehan, S. W., Noh, H., Brudvig, G. W., Cao, H. and Schmuttenmaer, C. A. *Plasmonic enhancement of dye-sensitized solar cells using core-shell-shell nanostructures*. *Journal of Physical Chemistry C*, 117, 927-934 (2013)
140. Derkacs, D., Lim, S. H., Matheu, P., Mar, W. and Yu, E. T. *Improved performance of amorphous silicon solar cells via scattering from surface plasmon polaritons in nearby metallic nanoparticles*. *Applied Physics Letters*, 89, 093103 (2006)

141. Ferry, V. E., Verschuuren, M. A., Li, H. B. T., Schropp, R. E. I., Atwater, H. A. and Polman, A. *Improved red-response in thin film a-Si:H solar cells with soft-imprinted plasmonic back reflectors*. Applied Physics Letters, 95, 183503 (2009)
142. Ferry, V. E., Verschuuren, M. A., Li, H. B. T., Verhagen, E., Walters, R. J., Schropp, R. E. I., Atwater, H. A. and Polman, A. *Light trapping in ultrathin plasmonic solar cells*. Optics Express, 18(102), A237-A245 (2010)
143. Tsai, F.-J., Wang, J.-Y., Huang, J.-J., Kiang, Y.-W. and Yang, C. C. *Absorption enhancement of an amorphous Si solar cell through surface plasmon-induced scattering with metal nanoparticles*. Optics Express, 18(102), A207-A220 (2010)
144. Zhu, J., Hsu, C.-M., Yu, Z., Fan, S. and Cui, Y. *Nanodome solar cells with efficient light management and self-cleaning*. Nano Letters, 10, 1979-1984 (2010)
145. Akimov, Y. A., Koh, W. S., Sian, S. Y. and Ren, S. *Nanoparticle-enhanced thin film solar cells: Metallic or dielectric nanoparticles?* Applied Physics Letters, 96, 073111 (2010)
146. Battaglia, C., Hsu, C.-M., Söderström, K., Escarre, J., Haug, F.-J., Charriere, M., Boccard, M., Despeisse, M., Alexander, D. T. L., Cantoni, M., Cui, Y. and Ballif, C. *Light trapping in solar cells: Can periodic beat random?* ACS Nano, 6, 2790-2797 (2012)
147. Bhattacharya, J., Chakravarty, N., Pattnaik, S., Slafer, W. D., Biswas, R. and Dalal, V. L. *A photonic-plasmonic structure for enhancing light absorption in thin film solar cells*. Applied Physics Letters, 99, 131114 (2011)
148. Biswas, R. and Xu, C. *Nano-crystalline silicon solar cell architecture with absorption at the classical $4n_2$ limit*. Optics Express, 19, A664 (2011)
149. Ferry, V. E., Verschuuren, M. A., Lare, M. C. v., Schropp, R. E. I., Atwater, H. A. and Polman, A. *Optimized spatial correlations for broadband light trapping nanopatterns in high efficiency ultrathin film a-Si:H solar cells*. Nano Letters, 11, 4239-4245 (2011)
150. Ho, C.-I., Yeh, D.-J., Su, V.-C., Yang, C.-H., Yang, P.-C., Pu, M.-Y., Kuan, C.-H., Cheng, I.-C. and Lee, S.-C. *Plasmonic multilayer nanoparticles enhanced photocurrent in thin film hydrogenated amorphous silicon solar cells*. Journal of Applied Physics, 112, 023113 (2012)
151. Hsu, C.-M., Battaglia, C., Pahud, C., Ruan, Z., Haug, F.-J., Fan, S., Ballif, C. and Cui, Y. *High-efficiency amorphous silicon solar cell on a periodic nanocone back reflector*. Advanced Energy Materials, 2, 628-633 (2012)
152. Kim, J., Abou-Kandil, A., Fogel, K., Hovel, H. and Sadana, D. K. *The role of high work-function metallic nanodots on the performance of a-Si:H solar cells: Offering ohmic contact to light trapping*. ACS Nano, 4, 7331-7336 (2010)
153. Kuang, Y., Werf, K. H. M. v. d., Houweling, S. Z. and Schropp, R. E. I. *Nanorod solar cell with an ultrathin a-Si:H absorber layer*. Applied Physics Letters, 98, 113111 (2011)
154. Lal, N. N., Zhou, H., Hawkeye, M., Sinha, J. K., Bartlett, P. N., Amaratunga, G. A. J. and Baumberg, J. J. *Using spacer layers to control metal and semiconductor absorption in ultrathin solar cells with plasmonic substrates*. Physical Review B, 85, 245318 (2012)
155. Lükermann, F., Heinzmann, U. and Stiebig, H. *Plasmon enhanced resonant defect absorption in thin a-Si:H n-i-p devices*. Applied Physics Letters, 100, 253907 (2012)
156. Massiot, I., Colin, C., Pere-Laperne, N., Cabarrocas, P. R., Sauvan, C., Lalanne, P., Pelouard, J.-L. and Collin, S. *Nanopatterned front contact for broadband absorption in ultra-thin amorphous silicon solar cells*. Applied Physics Letters, 101, 163901 (2012)
157. Moulin, E., Sukmanowski, J., Luo, P., Carius, R., Royer, F.-X. and Stiebig, H. *Improved light absorption in thin-film silicon solar cells by integration of silver nanoparticles*. Journal of Non-Crystalline Solids, 354, 2488-2491 (2008)

158. Santbergen, R., Liang, R. and Zeman, M. *A-Si:H solar cells with embedded silver nanoparticles*. In 35th IEEE Photovoltaic Specialists Conference. 748-753(2010)
159. Tan, H., Santbergen, R., Smets, A. H. M. and Zeman, M. *Plasmonic light trapping in thin-film silicon solar cells with improved self-assembled silver nanoparticles*. *Nano Letters*, 12, 4070-4075 (2012)
160. Wang, Y., Sun, T., Paudel, T., Zhang, Y., Ren, Z. and Kempa, K. *Metamaterial-plasmonic absorber structure for high efficiency amorphous silicon solar cells*. *Nano Letters*, 12, 440-445 (2011)
161. Losurdo, M., Bergmair, I., Giangregorio, M. M., Dastmalchi, B., Bianco, G. V., Helgert, C., Pshenay-Severin, E., Falkner, M., Pertsch, T., Kley, E.-B., Huebner, U., Verschuuren, M. A., Muehlberger, M., Hingerl, K. and Bruno, G. *Enhancing chemical and optical stability of silver nanostructures by low-temperature hydrogen atoms processing*. *The Journal of Physical Chemistry C*, 116, 23004-23012 (2012)
162. AGC Solar, www.agc-solar.com/agc-solar-products/coated-glass.html. (Visited on November 13, 2013)
163. Grandidier, J., Callahan, D. M., Munday, J. N. and Atwater, H. A. *Light absorption enhancement in thin-film solar cells using whispering gallery modes in dielectric nanospheres*. *Advanced Materials*, 23, 1272-1276 (2011)
164. Madou, M. J. *Fundamentals of microfabrication: the science of miniaturization*. 2nd ed. Boca Raton; London; New York; Washington, D.C.: CRC Press, 2002.- 723 p.
165. Photolithography liftoff. MC2 Processlab help pages, <http://processlab.mc2.chalmers.se>. ((Visited on 6 September 2011))
166. Ohring, M. *Materials science of thin films: deposition and structure*. 2nd ed. San Diego, CA: Academic Press, 2002.- 794 p.
167. *Handbook of vacuum science and technology* / ed. by Hoffman, D. M. San Diego, CA: Academic Press, 1998.- 835 p.
168. Fredriksson, H., Alaverdyan, Y., Dmitriev, A., Langhammer, C., S., S. D., Zäch, M. and Kasemo, B. *Hole-mask colloidal lithography*. *Advanced Materials*, 19(23), 4297 (2007)
169. Hulteen, J. C., Treichel, D. A., Smith, M. T., Duval, M. L., Jensen, T. R. and Van Duyne, R. P. *Nanosphere lithography: size-tunable silver nanoparticle and surface cluster arrays*. *Journal of Physical Chemistry B*, 103, 3854-3863 (1999)
170. Hanarp, P., Käll, M. and Sutherland, D. S. *Optical properties of short range ordered arrays of nanometer gold disks prepared by colloidal lithography*. *Journal of Physical Chemistry B*, 107, 5768-5772 (2003)
171. Luft, W. and Tsuo, Y. S. *Hydrogenated amorphous Silicon alloy deposition processes*. New York: Dekker, 1993.- 327 p.
172. Langhammer, C., Kasemo, B. and Zoric, I. *Absorption and scattering of light by Pt, Pd, Ag, and Au nanodisks: absolute cross sections and branching ratios*. *Journal of Chemical Physics*, 126, 194702 (2007)
173. *Insplorion software*, www.insplorion.com. (Visited on October 15, 2011)
174. Dahlin, A. B., Tegenfeldt, J. O. and Höök, F. *Improving the instrumental resolution of sensors based on Localized Surface Plasmon Resonance*. *Analytical Chemistry*, 78, 4416-4423 (2006)
175. J. A. Woollam Co., *I. Guide to Using WVASE 32*. 2001.- Version 3.335.

176. Azzam, R. M. A. *Ellipsometry: a sophisticated tool for optical metrology*. In SPIE Proceedings; Optical Metrology Roadmap for the Semiconductor, Optical, and Data Storage Industries. Vol. 4099 184-196(2000)
177. Ferlauto, A. S., Ferreira, G. M., Pearce, J. M., Wronski, C. R., Collins, R. W., Deng, X. and Ganguly, G. *Analytical model for the optical functions of amorphous semiconductors from the near-infrared to ultraviolet: Applications in thin film photovoltaics*. Journal of Applied Physics, 92(5), 2424-2436 (2002)
178. *Scanning microscopy for nanotechnology: techniques and applications* / ed. by Zhou, W. and Wang, Z. L. New York; London: Springer, 2007.- 522 p.
179. Stokes, D. *Principles and practice of Variable Pressure:Environmental Scanning Electron Microscopy (VP-ESEM)*. Chichester: Wiley, 2009.- 235 p.
180. Rodahl, M., Höök, F., Krozer, A., Brzezinski, P. and Kasemo, B. *Quartz crystal microbalance setup for frequency and Q-factor measurements in gaseous and liquid environments*. Review of Scientific Instruments, 66, 3924-3930 (1995)
181. Nomura, T. and Okuhara, M. *Frequency shifts of piezoelectric quartz crystals immersed in organic liquids*. Analytica Chimica Acta, 142, 218-284 (1982)
182. Speight, R. E. and Cooper, M. A. *A survey of the 2010 Quartz Crystal Microbalance literature*. Journal of Molecular Recognition, 25, 451-473 (2012)
183. Hägglund, C., Apell, P. S. and Kasemo, B. *Maximized optical absorption in ultrathin films and its application to plasmon-based two-dimensional photovoltaics*. Nano Letters, 10, 3135-3141 (2010)
184. Li, J.-R., Kuppler, R. J. and Zhou, H.-C. *Selective gas adsorption and separation in metal-organic frameworks*. Chemical Society Reviews, 38, 1477-1504 (2009)
185. Melde, B. J. and Johnson, B. J. *Mesoporous materials in sensing: morphology and functionality at the meso-interface*. Analytical and Bioanalytical Chemistry, 398, 1565-1573 (2010)
186. Shekhah, O., Liu, J., Fischer, R. A. and Wöll, C. *MOF thin films: existing and future applications*. Chemical Society Reviews, 40, 1081-1106 (2011)

